ACTIVE OXIDE NANOPHOTONICS

Thesis by

Matthew J. Dicken

In Partial Fulfillment of the Requirements

for the Degree of

Doctor of Philosophy

CALIFORNIA INSTITUTE OF TECHNOLOGY

Pasadena, California

2009

(Defended March 25, 2009)

ACKNOWLEDGEMENTS

I would like to gratefully acknowledge funding from the Center for Science and Engineering of Materials and the Army Research Lab. I would like to thank Harry Atwater for the seemingly endless resources and my committee for their attention. It has been my pleasure to work with the handful of fabulous people at Caltech. Finally, thank you Megan for your support and patience.

ABSTRACT

Materials that can be manipulated electrically or mechanically to induce a change in their intrinsic properties are highly relevant when suitably integrated with current technologies. These “active” materials, such as oxide-based ferroelectrics or materials with easily accessible changes of phase, find extensive use as mechanical resonators, solid-state memories, and optical modulators. Barium titanate, a tetragonal ferroelectric at room temperature, is a prime example of a material both mechanically and optically active. This thesis deals primarily with the deposition of active, oxide-based materials and their integration into device structures where either the mechanical or optical properties are exploited.

The technologically interesting paradigms within which these active oxide materials have been investigated are microelectromechanical systems, plasmonics, and metamaterials. Microelectromechanical systems are devices that have been micromachined and rely on an applied voltage to induce a mechanical response. Mechanically active materials, such as piezoelectrics or ferroelectrics, can increase the response of these devices. Plasmonics deals with electromagnetic waves resonantly coupled into free electron oscillations at a metal-dielectric interface or metal nanoparticle. Coupling to these resonant modes allows surface plasmon polaritons to propagate along the metal with a nonlinear dispersion. Metamaterials are ordered, subwavelength, metal inclusions in a dielectric, which respond collectively to electromagnetic radiation. This response can yield a material permittivity or permeability not found in nature. The optical properties of metamaterials lead to effects such as negative index response and super lensing, and can be used to design optical cloaking structures. Here, devices utilizing these effects are investigated with an eye toward tuning or switching their resonant response using optically active oxide thin films.

This manuscript follows the evolution of active oxide thin films from deposition, through design of plasmonic devices and active metamaterials, finite difference modeling of these structures, and finally experimental validation. First, deposition and material integration techniques for oxide-based thin films will be discussed. The role of molecular beam epitaxy, pulsed laser deposition, and ion beam assisted deposition as material growth techniques are investigated. Development of a multitude of oxide materials using these techniques including barium titanate, strontium ruthenate, vanadium oxide, and magnesium oxide will be covered. The following two sections deal with the mechanical and optical

properties of barium titanate thin films as they are studied and utilized to design and fabricate active devices. Films were characterized mechanically, using nanoindentation and piezoresponse force microscopy, and optically with variable angle spectroscopic ellipsometry. The subsequent section deals with the design, fabrication, and experimental validation of an active optical device based on surface plasmon polariton wavevector modulation via electrooptic modulation of a barium titanate thin film. Interferometers based on pairs of parallel slits fabricated in silver films on barium titanate are used to investigate optical modulation due to both domain switching and the electrooptic effect. Finally, active metamaterials are discussed through the investigation of a new material, vanadium oxide, as it is deposited and characterized, and the results used to design and fabricate active, split-ring resonator metamaterial structures.

TABLE OF CONTENTS

LIST OF FIGURES

Chapter 1
Introduction

Extrinsic material properties have been studied since the dawn of humankind. Understanding the composition and properties of the materials that make up our universe is of utmost importance for our technological progression. Throughout time, the classification of solid materials has evolved from purely utilitarian (hard, soft), to a knowledge of the elements (gold, lead), and finally to an understanding of materials on an atomistic scale. The study of materials and their interactions with nature has led to the discovery of such important properties as conductivity, magnetism, piezoelectricity, ferroelectricity, refraction, optical waveguiding, and a host of other effects. It is not an overstatement that all technologically relevant achievements have, at their roots, no small amount of materials research.

Of particular interest in the age of logic devices are materials and effects that can be controlled externally. Materials that demonstrate electrical or optical properties that can be modified by an external force are largely investigated or engineered to act as switching elements. Here, we investigate such active material properties as piezoelectricity, ferroelectricity, the electrooptic effect, and insulator-metal phase transitions.

1.1 Piezoelectricity and Ferroelectricity

Many interesting properties in solid materials can be derived from their crystal symmetry. Solid systems of atoms can be classified into 32 symmetric point groups, 20 of which are noncentrosymmetric. It is from this select class of materials that the piezoelectric and ferroelectric effects arise. The electromechanical properties of materials were first studied in the later 1800s by Pierre and Jacques Curie. Their initial work characterized the piezoelectric effect from studies of Rochelle salt and quartz. Further work on Rochelle salt led to the discovery of ferroelectric effect by Valasek in 1920 (*Nye 1957*). Ferroelectric materials exhibit spontaneous electrical polarization due to a structural displacement of atoms in the crystal unit cell. Interactions between adjacent unit cells lead to polarization domain formation similar to ferromagnetic domains. The quintessential ferroelectric

material, barium titanate, $BaTiO_3$, (BTO) and its domain patterns are shown in figure 1.1 (*Bhattacharya et al. 2003*).

The ferroelectric effect in materials, including BTO, exists as a result of a polar axis found in 10 of the 20 noncentrosymmetric crystal point groups. Ferroelectric materials are characterized by the existence of a switchable dipole moment within the crystal unit cell. All ferroelectric materials also exhibit the piezoelectric effect, defined as a mechanically induced polarization of the lattice (*Fatuzzo et al. 1967*). The piezoelectric effect (equation (1.1)) linearly relates the induced charge density, $\mathbf{D_i}$, due to an applied stress, $\boldsymbol{\sigma_{jk}}$, in a material.

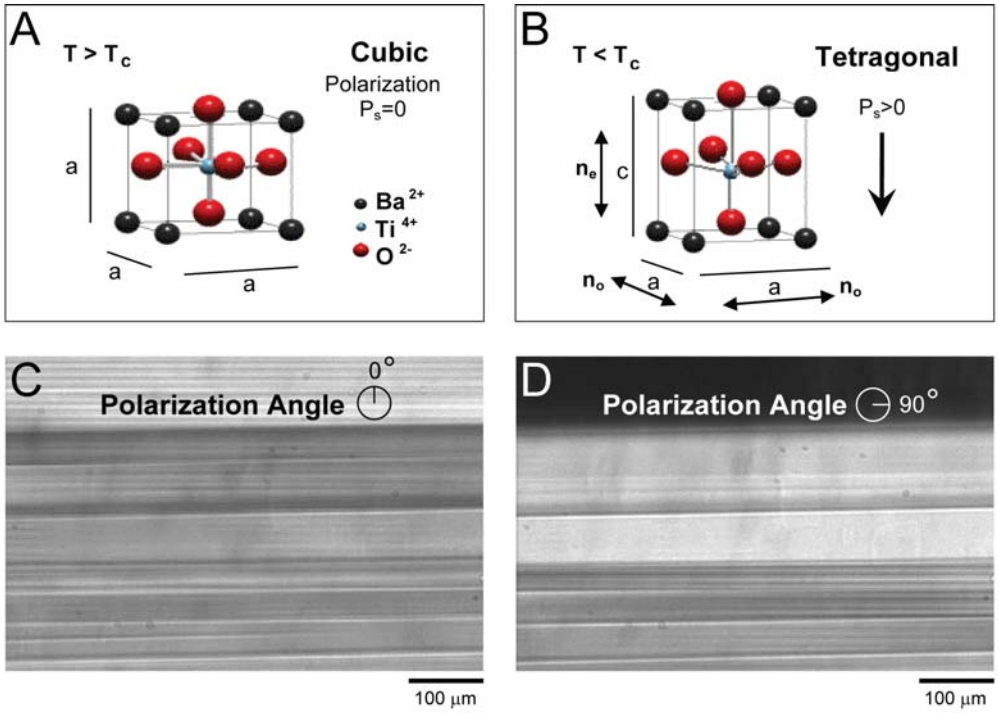

Figure 1.1. Barium titanate domain structure. Tetragonal $BaTiO_3$ above (A) and below (B) its Curie temperature, T_c, demonstrating the displacement of the oxygen tetrahedron from the central Ti atom and subsequent spontaneous polarization. Ferroelectric domains form below the Curie temperature imaged using a polarized optical microscope at 0° (C) and 90° (D).

$$D_i = d_{ijk}\sigma_{jk} \tag{1.1}$$

Here, $\mathbf{d_{ijk}}$ is a third-rank tensor of piezocoefficients that relate the charge and stress in 3-D. It is more common to encounter the converse piezoelectric effect (equation (1.2)), defined as the strain, $\boldsymbol{\varepsilon_{ij}}$, induced due to an applied electric field, $\mathbf{E_k}$.

$$\varepsilon_{ij} = d_{kij}E_k \tag{1.2}$$

The piezoelectric coefficients form a symmetric third-rank tensor, and the symmetry of the material can be used to reduce many of the elements to zero. Those elements which are non-zero are determined by the symmetry point group of the crystal. The perovskite oxide ferroelectrics, BTO, strontium titanate (STO) and lead titanate (PTO), have a point group of P4MM and the resulting tensor has the form

$$\begin{bmatrix} 0 & 0 & 0 & 0 & d_{15} & 0 \\ 0 & 0 & 0 & d_{15} & 0 & 0 \\ d_{31} & d_{31} & d_{33} & 0 & 0 & 0 \end{bmatrix}. \tag{1.3}$$

This tensor shows two shear components, $\mathbf{d_{31}}$ and $\mathbf{d_{15}}$, and one direct response, $\mathbf{d_{33}}$, for a given directional effect (electric field, stress, etc.). The form of the response tensor will be identical for other linear effects on the P4MM crystal structure, and therefore the same coefficients will be non-zero in the tensor describing the electrooptic coefficients. The dependence of orientation on these properties must be understood and controlled during ferroelectric device design and fabrication.

1.1.1 Orientation Effects

Crystal orientation plays a large role in the response of a material to external effects. The tensorial nature of bulk material properties is well known and equations can be written to describe the combined response including all coefficients (equation (1.4)) and they can be represented in 3-D as polar plots (figure 1.2) (*Harnagea 2001*).

$$d_{zz} = d_{33}\cos^3\theta + (d_{15} + d_{13})\cos\theta\sin^2\theta \tag{1.4}$$

The maximum value of equation (1.4) for BTO is at $d_{zz} = 52°$ off of the z-axis. This has been investigated by Li and Ruglovsky *et al*. who found that some degree of misorientation or mosaity in the crystal orientation can lead to increased piezoresponse from the material. The same analysis shows that the largest electrooptic response in BTO is at an angle off of the z-axis. Orientation effects can be taken advantage of by engineering deposition parameters to yield specific crystal orientations in thin films.

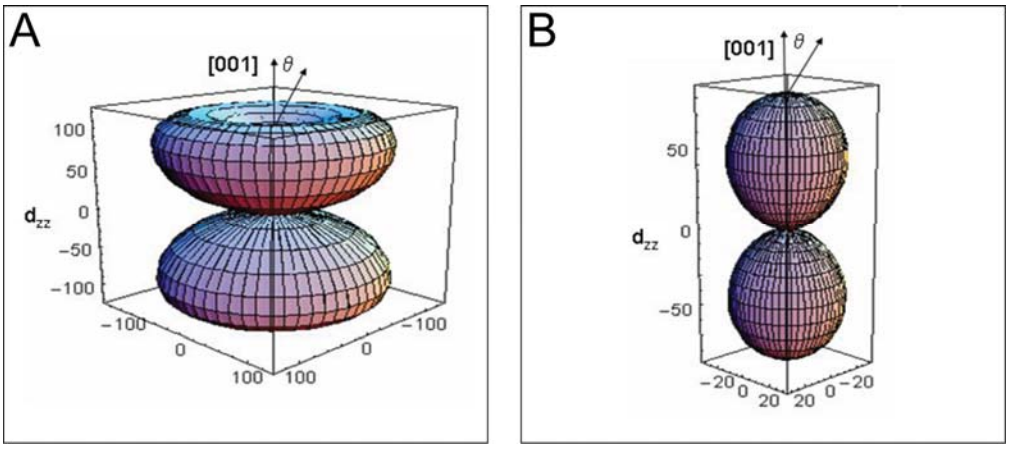

Figure 1.2. Orientation effects on piezoresponse in ferroelectrics. Polar plots using equation (1.4) and piezocoefficients from (A) BTO and (B) PTO to show the orientation effects on piezoresponse.

Ferroelectric domains can be manipulated externally through application of an electric field or applied stress leading to many sensing and actuating applications. One of the most successful applications of ferroelectric materials thus far is as the active material in solid state memory devices. Information can be stored and read through domain manipulation via locally applied voltage (*Scott 2000*). Manipulating ferroelectric domains, through applied fields or stresses, changes the material properties according to the following constitutive equations,

$$\sigma_i = C_{i,j}\varepsilon_j - e_{i,k}E_k \quad , \tag{1.5}$$

$$D_l = e_{l,m}\varepsilon_m + \kappa_{l,n}E_n \quad , \tag{1.6}$$

which show the coupled nature of elastic stress (**σ**), displacement (**D**), elastic strain (**ε**) and applied field (**E**) with their proportionality constants (**C, ε, κ**) (*Damjanovic 1998, Nye 1957*). Understanding and engineering the mechanical and optical activity of ferroelectric materials opens new avenues for device design.

1.2 Active Materials

A central theme of this thesis work is coaxing tunable mechanical, optical, or electrical responses from thin film materials through an external force. Barium titanate, the material of focus for the first half of this thesis, exhibits ferroelectric and electrooptic properties, which can induce both mechanical and optical changes. Vanadium (II) oxide (VO_2) has a low insulator-metal transition temperature which causes the material to become conductive and highly absorbing in the infrared portion of the spectrum. Mechanical and optical activity in BTO will be discussed in the following sections. Effects of the VO_2 phase transition and its application to active metamaterial designs will be examined in chapter 7.

1.2.1 Mechanically Active Materials

Ferroelectric thin films exhibit mechanical responses to applied stress or electric fields. The realization that ferroelectric materials can achieve a large work per unit volume has led to their increased use in microelectromechanical systems (MEMS) recently (figure 1.3) (*Bhattacharya et al. 2005*). Utilizing the tetragonal structure of titanate-based ferroelectrics, MEMS designs can achieve up to 6% dilatation in optimized devices (*Burcsu et al. 2000*). Recent work by Bhattacharya and Ruglovsky investigated domain switching in ferroelectric films as a route toward large deflections in micromachined cantilevers (*Ruglovsky 2007*). BTO and PTO films used in this work were developed using molecular beam epitaxy and pulsed laser deposition. A top-down approach was used to fabricate the cantilevers using reactive ion etching or focused ion beam milling. This work brought to light the issue of polarization fatigue due to metal contacts.

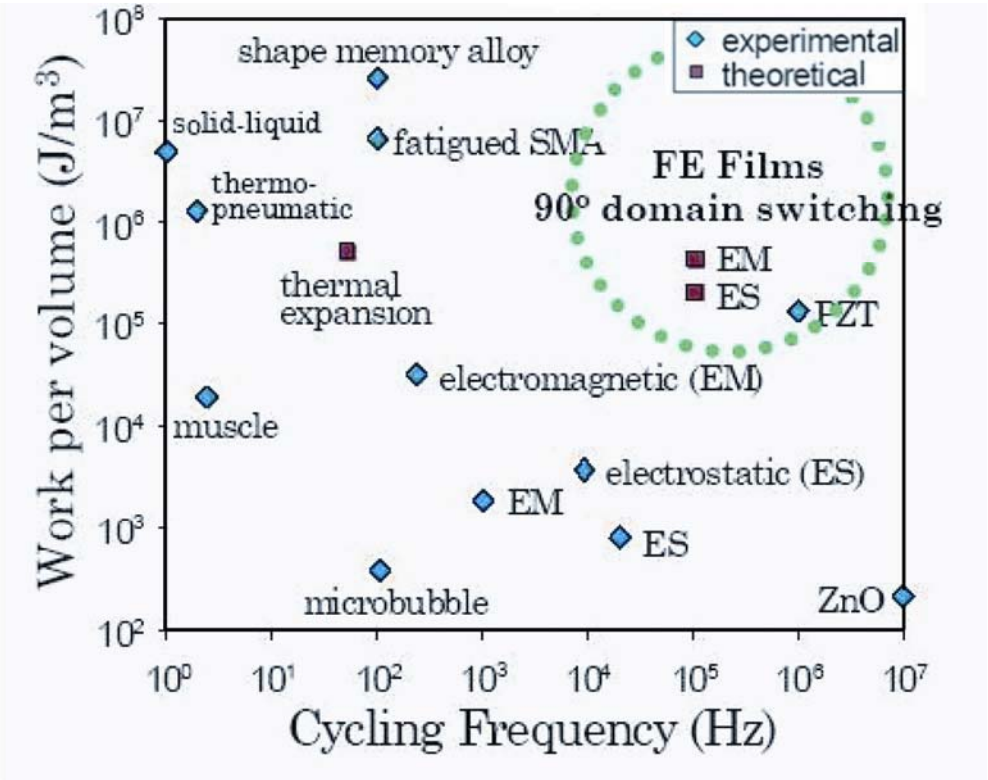

Figure 1.3. Mechanical work vs cycling frequency. Plot of mechanically active materials used in microelectromechanical systems showing their relative work output at a given cycling frequency (*Krulevitch et al. 1996*).

1.2.2 Fatigue

Manipulating the properties of ferroelectric oxides requires application of an electric field across the thin film. To achieve this, conductive electrodes must be integrated into the film stack. It has been shown over the years that metal electrodes are detrimental to ferroelectric oxide devices as they speed up device fatigue (figure 1.4) (*Duiker et al. 1990, Scott et al. 1991*).

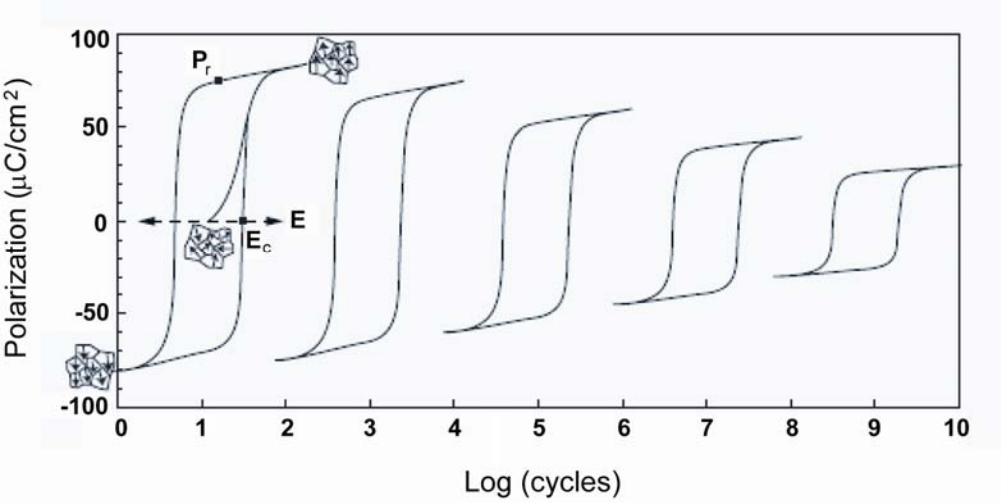

Figure 1.4. Polarization fatigue. Schematic of P-E curves as a function of number of polarization switching cycles. The effects of fatigue can be seen as the number of cycles increases and the remnant polarization decreases.

One of the biggest problems facing ferroelectric materials integration has been the existence of polarization fatigue. Switching domains in these materials at high frequencies wears the material down and causes the remnant polarization to slowly disappear. This is often due to the incompatibility of metal electrodes used to apply the switching field. Metal electrodes getter oxygen from the lattice, forming an oxide at the interface and eventually causing a breakdown in the device (*Duiker et al. 1990*). One solution to this problem is the use of oxide-based electrodes. Such materials (strontium ruthenate (SRO), lanthanum nickelate (LNO), and lanthanum strontium cobalt oxide (LSCO)) are conductive enough to provide high-frequency switching voltages but do not act as a sink for oxygen from the ferroelectric (*Ramesh et al. 1992*). Conductive oxides can be engineered to have very low optical absorption in the visible range (*Dicken et al. 2007*). This can negatively impact electrical conductivity in the oxide, but is a great advantage for many optical device designs. Integration of low optical absorption oxide electrodes with active oxide materials is necessary for high-frequency switching applications over many cycles.

1.2.3 Optically Active Oxides

In addition to their uses as mechanically active materials, oxide-based ferroelectrics find applications in optically active devices. The most common electrooptic materials used are $LiNbO_3$, $BaTiO_3$, KH_2PO_4, and CdTe. These materials are all non-centrosymmetric and therefore exhibit the Pockels effect, which is also known as the linear electrooptic effect (*Saleh et al. 1991*). Lithium niobate is a popular choice as an electrooptic material due to the ease with which an optical modulator can be fabricated. Diffusing hydrogen into the $LiNbO_3$ lattice causes the index to increase in the affected region, thus forming a waveguide. BTO, however, has advantages over lithium niobate in that it can be deposited as a thin film and it has higher electrooptic coefficients in specific crystal directions.

The perovskite oxide BTO exhibits both the linear electrooptic effect as well as a large birefringence due to its tetragonal crystal structure. The electrooptic effect describes the electric field dependence of the index of refraction for a material (equation (1.7)). This effect is tensorial and follows the same analysis discussed previously for the piezoelectric effect.

$$n_{ij}(E) = n_{ij} + \sum_{k} r_{ijk} E_k + \sum_{kl} s_{ijkl} E_k E_l \tag{1.7}$$

Here, the linear coefficient, $\mathbf{r_{ijk}}$, is called the Pockels coefficient, and the second-order coefficient, $\mathbf{s_{ijkl}}$, is known as the Kerr coefficient. While all materials exhibit the second-order electrooptic effect, the Pockels effect only follows from non-centrosymmetric crystal structures. There is much interest in using BTO as an electrooptic material because of its large Pockels coefficient.

BTO thin films have been studied extensively as a route toward chip-based optics. Waveguides and modulators have been fabricated in BTO thin films deposited by chemical vapor deposition, molecular beam expitaxy, and pulsed laser deposition techniques (figure 1.5) (*Petraru et al. 2002, Schlom et al. 2001, Tang et al. 2004b*). It has been shown that BTO can operate at switching speeds up to 40GHz with effective electrooptic coefficients as high as 300 pm/V (*Petraru et al. 2002, Tang et al. 2004a*).

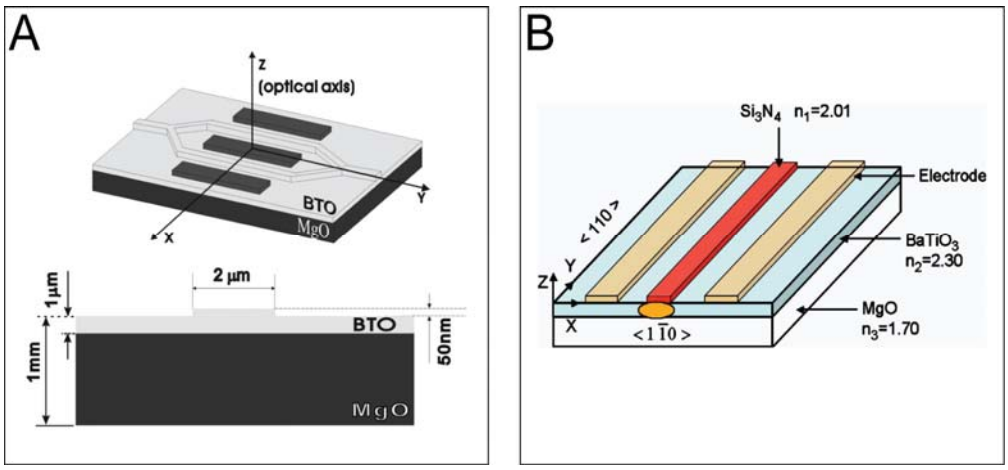

Figure 1.5. Barium titanate based electrooptic devices. (A) Schematic of a typical ridge-type Mach-Zehnder interferometer constructed from BTO. The index contrast at the air/BTO interface confines the optical mode beneath the 50 nm ridge. (B) Silicon nitride strip-loaded linear waveguide. Both devices achieve modulation through the electrooptic effect by applying a voltage across the BTO via in-plane electrodes.

1.3 Nanophotonics

As the age of miniaturization progresses, millimeter-long optical devices must become *passé* (*ITRS 2007*). To this effect, we look toward integrating these materials with new physics as a means of shrinking device size. Potential for the application of BTO thin films within the realm of nanophotonics is rich, but requires some method of increasing the strength of light-matter interactions in order to utilize the electrooptic effects in a much smaller device volume. Enter plasmonics and metamaterials.

1.3.1 Plasmonics

Perhaps the most common introductory sentence in photonic and electronic device literature is some variation on "Increasing speed/storage and shrinking device sizes, driven by Moore's law, has lead to the development of [engineering feat] for [device] with [figure of merit]." While this may be true for the fields of plasmonics and metamaterials, the physics behind these subjects is extraordinarily rich and deserves study in its own right.

Plasmonics is the *nom de guerre* for the field of nanophotonics dealing with collective oscillations of charge in nanoparticles or at a metal-dielectric interface. Plasmons occur both in the bulk (equation (1.8)) and at the surface (equation (1.9)) of a material with suitably free electrons to support these oscillations.

$$\omega_p = \sqrt{\frac{4\pi N e^2}{m\varepsilon_0}} \tag{1.8}$$

$$\omega_{sp} = \frac{\omega_p}{\sqrt{1+2\varepsilon_d}} \tag{1.9}$$

Here, ω_p and ω_{sp} are the bulk and surface plasmon frequencies, N is the density of electrons, m is the electron mass, e the electron charge and ε_0 and ε_d the permittivity of free space and relative permittivity of the medium. Optical power can be coupled into plasmon modes externally via electromagnetic waves. The fundamentally interesting property of surface plasmons is the broad spectrum of frequencies possible depending on the wave vector. The dispersion relation for surface plasmons lies to the right of the "light line" ($\omega = ck$), meaning they have a longer wavevector than light with the same energy. Since surface plasmons have a higher momentum than light, they remain bound to the surface during propagation. This leads to a propagating mode with evanescent fields into both the metal and the dielectric as described by (*Raether 1988*),

$$k_{sp} = k_0 \sqrt{\frac{\varepsilon_m \varepsilon_d}{\varepsilon_m + \varepsilon_d}} \quad , \tag{1.10}$$

where ε_m and ε_d are the dielectric functions of the metal and the dielectric, and k_0 and k_{sp} are the free-space and surface plasmon wavevectors.

Plasmon oscillations can also be induced in localized geometries such as nanoparticles, or nanoscale grooves and holes in metals. Electromagnetic waves can be used to pump the free electrons in a metal nanoparticle. This leads to enhanced absorption at the plasmon frequency of the metal because the energy is being coupled efficiently into this mode. Plasmons can be coupled into surface modes using grating-like structures, or launched from grooves or slits. There is a wealth of literature exploring this coupling via gratings as well as enhanced transmission due to plasmon propagation through sub-wavelength slits and holes (*Ebbesen et al. 1998, Garcia-Vidal et al. 2003, Lalanne et al.*

2005, Lezec et al. 2002, Lezec et al. 2004, Thio et al. 2001). This work uses plasmon-mediated enhanced transmission from subwavelength slits to design plasmon interferometer structures, as described in chapter 6.

Recently there has been increased interest in using optically active materials for plasmonics and metamaterial applications (*Pacifici et al. 2007*). It has been found that electromagnetic radiation can be coupled into these oscillations and propagate as a surface plasmon polaritons (SPPs) at a metal-insulator interface (figure 1.6) (*Barnes et al. 2003, Dionne et al. 2005, Kretschmann et al. 1968*). Metallic nanoparticles show analogous behavior when resonantly pumped at their plasmon frequency, resulting in enhanced absorption (figure 1.7) (*Maier et al. 2003, Sweatlock et al. 2005, Wei et al. 2004*).

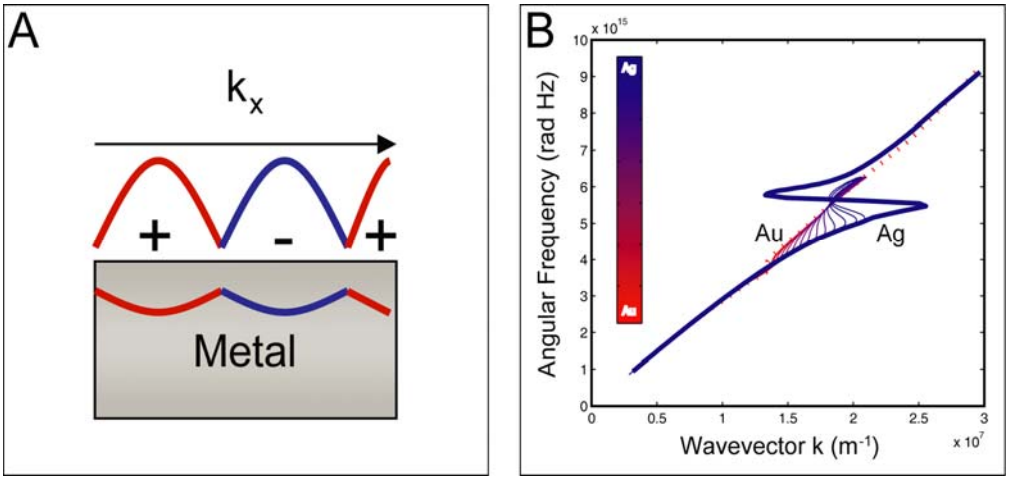

Figure 1.6. Plasmon dispersion and resonance. (A) Schematic of the surface charge profile resulting in SPPs in thin metal films. Bound SPP modes propagate with a wavevector based on the optical properties of both materials. (B) Corresponding dispersion relation for SPP propagation at metal-air interface. Dispersion curves shown are calculated from a Au/Ag alloy optical data.

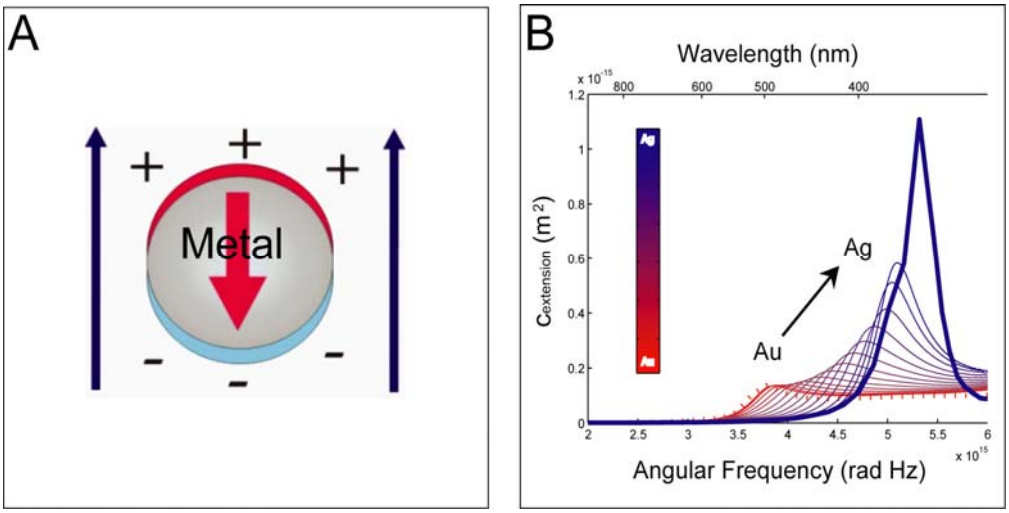

Figure 1.7. Nanoparticle plasmon resonance. (A) Schematic of the dipole charge distribution in a "nanoparticle." Energy can be coupled into the particle by resonantly pumping at the natural frequency of the electron gas. (B) Calculated extinction cross section for 10 nm metal alloy nanoparticles using the optical properties of a Au/Ag alloy (*Bohren et al. 1983*).

Coupling EM radiation into SPP modes at a metal-dielectric interface using sub-wavelength slits and grooves has been studied extensively (*Ebbesen et al. 1998, Lezec et al. 2002, Lezec & Thio 2004*). We are interested in coupling light into these modes at a metal-oxide interface in order to shrink the SPP wavelength and increase the light-matter interaction. Figure 1.8 shows schematically how the wavelength of a SPP changes in a metal-insulator-metal structure. Incorporating optically active materials into these plasmonic structures has led to tunable devices and has implications for future work on metal-insulator-metal waveguides, transistor-like devices, and more vibrant optical display technologies.

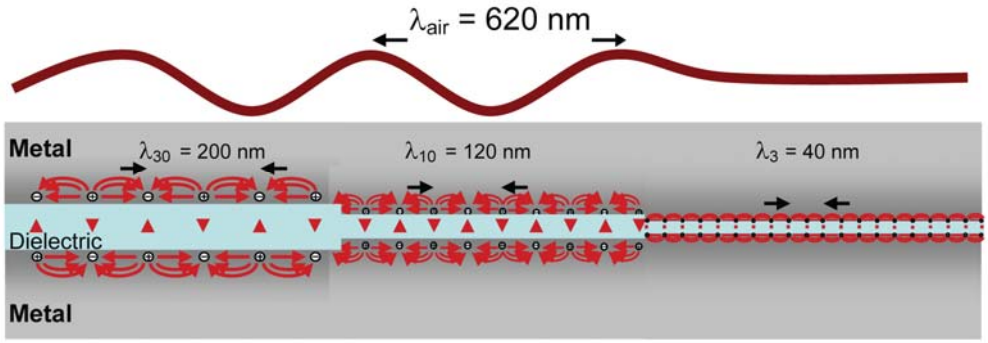

Figure 1.8. Metal-insulator-metal plasmon waveguide. Schematic showing the SPP wavelength change in a metal-insulator-metal structure as the dimensions shrink. Light is very strongly confined in the thinnest section of the waveguide, propagating with a wavelength 15 times smaller than it would in free space.

1.3.2 Metamaterials

Metamaterials are distinguished from their cousins, "regular materials," by the fact that they are designed and fabricated from an array of subwavelength metal structures in a dielectric medium. These novel structures, or composite materials, have electromagnetic response functions not physically realizable in nature. The metal structures are typically notched rings, so-called split-ring resonators (SRRs), with physical dimensions much smaller than the wavelength of interest. Each SRR acts as nanoscale R-L-C circuit, and the collective response of arrays of these rings is equivalent to that of a material with a new magnetic permeability, μ, or electric permittivity, ε, and thus new transmission and reflection properties (figure 1.9) (*Smith et al. 2000, Veselago 1968*). Through intelligent design, these materials can be made to exhibit negative values of either μ, ε, or both simultaneously.

Resonant transmission spectra can be tuned by integrating an optically active material as the dielectric medium in a metamaterial.

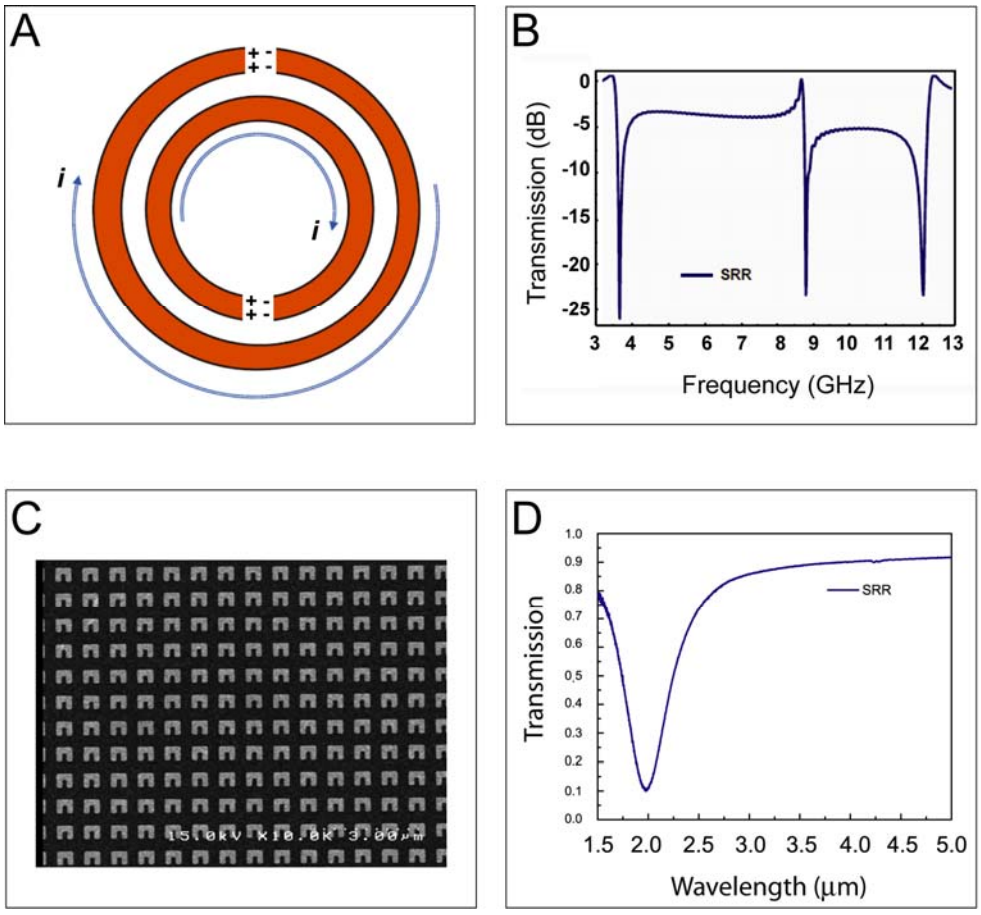

Figure 1.9. Split-ring resonators. Electromagnetic waves incident on an SRR structure induces a current and capacitive response in the gap. The transmission of EM radiation through these structures shows resonant suppression when the energy is coupled into the SRR. (A) Schematic of SRR structures with transmission (B) in the GHz frequency range (*Aydin 2008*). (C) Scanning electron microscope image of a SRR metamaterial array with resonant transmission (D) in the THz, or near-IR spectrum.

The theory of metamaterials was presented first in 1968 by Veselago. It was 30 years later that the first structures were realized and negative values of ε and μ were achieved in the microwave frequency range (*Pendry et al. 1999*). Metamaterial structures for operation in the microwave regime are large enough to pattern conventionally. Nanofabrication has allowed these structures to be miniaturized, and their operating frequency scales accordingly. Current nanostructures are based on either rods, to affect permittivity (*Shalaev et al. 2005*),

or split-ring resonators, to affect permeability (*Linden et al. 2004*). Nanostructured metamaterials have their resonant properties in the mid- and near-infrared spectrum. The first example of an active metamaterial in the THz frequency band was shown by Chen *et al.* and utilized the depletion region in a metal-semiconductor junction to change the gap length in an array of SRRs (*Chen et al. 2006*) and the same group showed this effect in SRRs on silicon by photoexcitation of charge carriers (*Chen et al. 2008*). We will discuss simulations and experiments for active metamaterials, based on the metal-insulator transition in VO_2.

1.4 Thesis Scope

The work presented in this thesis can be divided into three parts: developing active oxide materials as thin films, designing optical devices based on these thin films, and experimentally validating these devices. Initially, this research focused primarily on mechanically active thin films based on BTO, and films were developed and characterized with this in mind. Following the success of those endeavors, we saw an opportunity to utilize oxide thin films to design active devices in the emerging fields of plasmonics and metamaterials. Devices based on these effects were designed, modeled, fabricated, and tested in this work. For the purposes of this thesis, we will discuss film growth, characterization, and device applications in three separate sections.

1.4.1 Part I: Thin Film Deposition and Characterization Techniques

The section on film growth will cover the techniques used to deposit thin films of the various oxide materials used in this thesis work. These materials include BTO, SRO, STO, PTO and VO_2. Deposition of these materials was carried out using either molecular beam epitaxy (MBE) or pulsed laser deposition (PLD). Also included in this section is a description of ion beam assisted deposition (IBAD) of MgO. IBAD is used to integrate biaxially oriented thin films of complex oxides on arbitrary, smooth substrates.

Chapter 2 covers the background for the work presented here through an in-depth look at ferroelectric thin film deposition and characterization techniques. A description of the material deposition techniques will be given, with emphasis on those used to develop oxide thin films. The three most prevalent characterization techniques used will be covered: reflection high energy electron diffraction (RHEED), variable angle spectroscopic ellipsometry (VASE), and piezoforce microscopy (PFM).

Chapter 3 provides a thorough description of the thin film materials grown, and the quality of these films with respect to crystal structure, degree of epitaxy, orientation, and phase. IBAD MgO deposited on amorphous silicon nitride, or any substrate with less than 5 nm RMS roughness, yields a biaxially oriented template on which any material lattice matched to MgO can be grown. We will compare growth of BTO, PTO, SRO, STO, and VO_2 on IBAD MgO and bulk MgO, as well as other substrates. BTO is the flagship material for this thesis and its growth via MBE and PLD will be discussed in depth. Similarly, PLD was found to be the most versatile growth process and its role in deposition of BTO, SRO, PTO, SRO, and VO_2 will be highlighted.

1.4.2 Part II: Mechanical and Optical Characterization of Active Oxides

The results of extensive mechanical and optical characterization of thin films used in this work are discussed in Part II of the thesis. Chapter 4 deals specifically with mechanical characterization. The piezo- and ferroelectric properties of BTO were investigated for films on bulk and IBAD MgO substrates. Piezoforce microscopy and nanoindentation was performed on BTO thin films to study ferroelectric domain properties. Comparative PFM studies were done on BTO grown on conductive layers of Pt, SRO, and lanthanum strontium cobalt oxide (LSCO). Additionally, films were micromachined into cantilevers to investigate domain switching as a means of mechanical beam bending.

Optical characterization of the films was carried out using variable angle spectroscopic ellipsometry. Chapter 5 presents optical models used to fit VASE data and extract the index of refraction and absorption as a function of wavelength over the range 300-2200 nm for many of the materials discussed in this thesis. A parametric study of MBE BTO growth is presented showing the effects of oxygen on the absorption characteristics of the films. Two models are presented for PLD VO_2 thin films, describing its index and absorption in both the semiconducting and metallic phases.

1.4.3 Part III: Active Metal-Oxide Nanophotonics

Having developed and characterized thin films of active oxide materials, we turn our attention to device applications in the final portion of the thesis. Mechanical applications, specifically MEMS cantilevers and bridges, are the topic of previous thesis work. Here, we

present optical device applications for these active oxide thin films in the form of double-slit plasmonic interferometers and optically active metamaterials.

Active oxide applications to SPP-mediated devices are covered in chapter 6. Transmission from arrays of double-slit interferometers milled in Ag films on BTO is used to investigate SPP propagation. Specifically, modulation of the SPP wavevector through electrooptic changes in the BTO index of refraction will be discussed. Modulation was achieved by applying a voltage across the BTO film via the silver top contact and a layer of transparent, conductive, SRO under the film. Change in the transmission as a function of voltage is attributed to a combination of domain switching and the electrooptic effects in BTO.

This work continues in chapter 7 where we investigate, fabricate, and test active metamaterials based on VO_2. Metamaterial designs were engineered to take advantage of the insulator-metal phase transition in VO_2. Arrays of metal/VO2 hybrid-SRRs can have their transmission spectra modified by electrically shorting the ring at the phase transition temperature. We designed, simulated, fabricated, and experimentally verified active metamaterials with resonant transmission peaks in the near-infrared range. The effects of heating, applied voltage and optical switching of the VO_2 thin films and SRR structures will be discussed.

Chapter 8 investigates a combinatorial technique for bimetal alloy deposition with regard to the optical properties of the metal alloy. Magnetron sputtering was used to codeposit bimetal alloys of various metals including; Ag, Au, and Cu. The optical properties as a function of alloy composition were measured using VASE. We found that the optical properties changed smoothly from one pure element to the other. The optical data were used to validate a new method for fitting the dielectric function using a genetic algorithm based on Lorentz-Drude-Debye formalism.

Part I

Thin Film Deposition and Characterization Techniques

Chapter 2
Background

This chapter illuminates the relevant mechanical and optical material properties, various deposition and characterization techniques used, and the applications toward the fields of plasmonics and metamaterials to which this thesis, as a whole, aspires.

2.1 Deposition Techniques

There are numerous deposition techniques for thin film materials in the literature. The choice of a deposition technique is often a trade-off between ease of processing and material quality. Common processing techniques for oxides include: sol-gel, metal-organic vapor deposition, MBE, and PLD. For the purposes of this thesis we will discuss the latter two techniques, MBE and PLD. Prior to the discussion of growth techniques, we will introduce IBAD MgO as a method for integration of biaxially oriented thin films.

2.1.1 Ion Beam Assisted Deposition of MgO

IBAD was first used by Yu *et al*. to grow biaxially oriented niobium films on amorphous substrates. The technique uses an ion beam, impinging on the substrate, to develop the texture of a material being deposited by physical vapor deposition. There are two purported mechanisms to explain how IBAD develops the biaxial texture. The first considers selective milling of the material being deposited contingent upon its orientation to the ion beam (*Bradley et al. 1986, Yu et al. 1985*). The second relies on molecular dynamics simulations to show that anisotropic, ion-induced, damage leads to grains of one dominant orientation (*Dong et al. 1998, Ressler et al. 1997*).

Using the IBAD technique, biaxially oriented MgO has been deposited on silicon nitride with less than 7° FWHM in-plane distribution and less than 4° FWHM out-of-plane distribution (*Brewer et al. 2002*). Biaxially textured films have grains oriented with a narrow distribution in-plane and out-of-plane and exhibit properties converging on those of a single crystal. We used IBAD MgO templates to deposit biaxially oriented ferroelectric films on silicon nitride and silicon dioxide to investigate crystal orientation effects on piezoresponse. Deposition of both IBAD MgO and heteroepitaxial BTO takes place sequentially in the same

UHV chamber (figure 2.1). The IBAD MgO films fabricated using this system have been used extensively in this work in addition to work previously published by El-Naggar and Ruglovsky (*El-Naggar 2006, Ruglovsky 2007*). Specific characterization results for these films will be discussed in chapter 3.

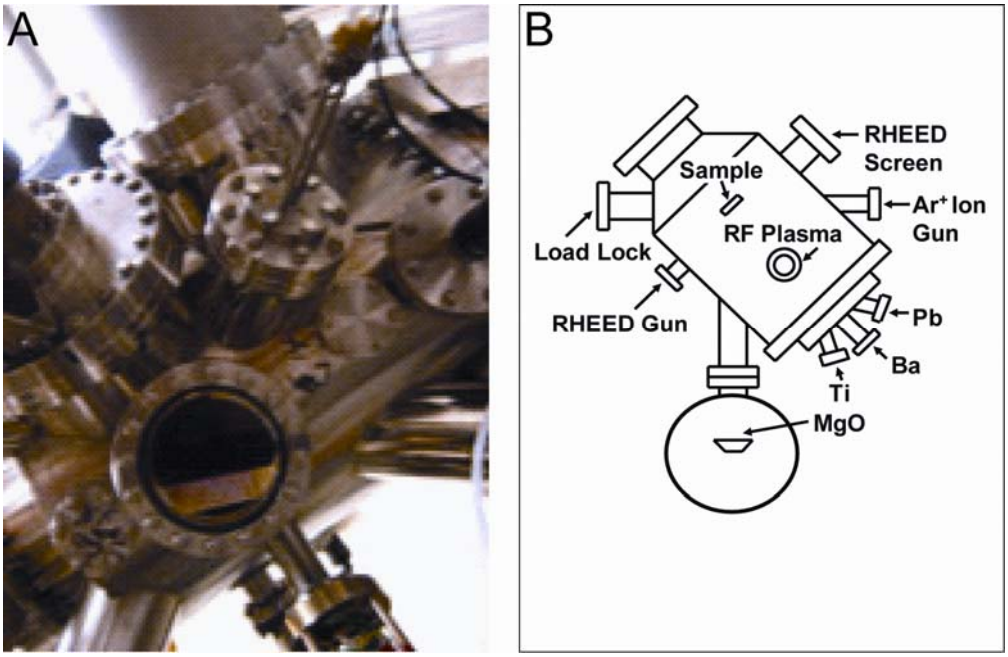

Figure 2.1. Ultra-high vacuum molecular beam epitaxy system. (A) UHV chamber equipped for IBAD MgO and MBE of complex oxides. (B) Chamber schematic showing the placement of the titanium sublimation pump, barium and lead effusion cells, e-beam MgO source, argon ion gun used for IBAD, RF oxygen plasma source and *in situ* RHEED.

2.1.2 Molecular Beam Epitaxy-MBE

Initial work on BTO deposition was carried out using an UHV chamber equipped for MBE deposition of oxide materials. MBE uses high temperature effusion cells to individually heat Ba, Pb, or Sr, creating a uniform flux of material toward the substrate. The custom built MBE chamber is also equipped with a Ti sublimation pump (Varian Ti-Ball) which is used as a Ti source (*Theis et al. 1996*). Each material source is operated by a computer controlled pneumatic shutter using Labview software. Layer-by-layer deposition takes place by shuttered growth in an oxygen ambient provided by a leak valve through a RF plasma source. The RF plasma source generates reactive oxygen radicals which lead to better film stoichiometry and lower optical absorption. A quartz crystal monitor is used to

measure flux rates and confirm stability prior to deposition. Once the source deposition rates and substrate temperature are stable, the substrate shutter is retracted and the source-shuttered growth begins. Previously, MBE has been used to grow thin films of BTO, STO, and PTO (*Schlom et al. 2001*). They have demonstrated such effects as strain induced lowering of the Curie temperature through substrate engineering (*Choi et al. 2004*).

2.1.3 Pulsed Laser Deposition-PLD

PLD is a high vacuum technique utilizing a high energy laser pulse to atomize a target material which redeposits on a heated substrate (figure 2.2). The KrF excimer laser (λ = 247 nm) used is pulsed at 10 Hz with a pulse power of 300 mJ/pulse. Optical components are used to shape the laser beam and focus the pulses on the target. The substrate and targets rotate in plane, and targets raster back and forth, enabling a uniform deposition of material. As each pulse is absorbed by the target material, it is converted to thermal, chemical, and mechanical energy, resulting in evaporation, ablation, and plasma formation. The highly energetic material forms a bright plume consisting of atoms, electrons, and larger material particles. Typically, the target-substrate distance and the chamber background pressure are engineered to reduce number of larger material particles, which lead to poor quality films.

PLD has proven to be a particularly powerful deposition tool and has been used to deposit materials that previously were not available as thin films. This results from the fact that almost any material that can be formed into a sintered pellet can be used as a PLD target. Doped materials, like 1% W in VO_2, can be deposited simply by employing a target with the desired composition (*Jin et al. 1995*). Metal oxide materials (like VO_2) have been deposited using both pure metal targets and targets composed of the oxide of interest (*Donev et al. 2006, Lappalainen et al. 2008, Suh et al. 2004*). Materials with components too volatile to deposit easily with MBE, like PTO, have been deposited and used in work by Ruglovsky (*Ruglovsky 2007*). The Neocera PLD used in this work is equipped to deposit from up to six different targets. This can be used for combinatorial synthesis, a powerful technique used to create a continuum of sample compositions on a single substrate.

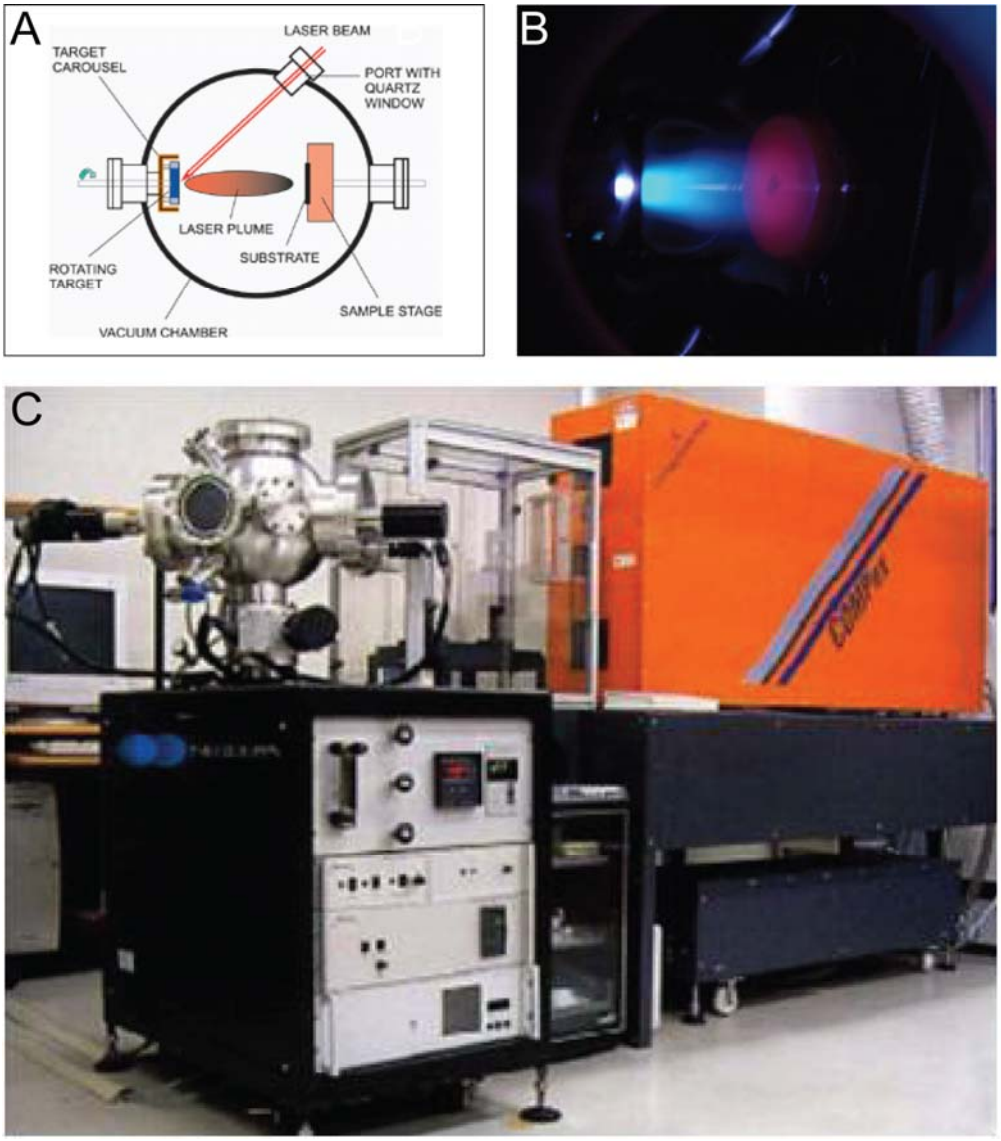

Figure 2.2. Pulsed laser deposition system. (A) PLD schematic showing the relative placement of targets, substrate, and quartz laser port. (B) Example of energetic plume of material created with each laser pulse. (C) Neocera PLD system.

2.2 Characterization Techniques

In the beginning stages of thin film development, material properties are optimized by changing process parameters with each sample growth. During this phase, each sample requires extensive characterization to dictate the parameters of the next sample. It is important to have a method for *in situ* characterization during growth. In this work we rely heavily on *in situ* RHEED to characterize films. After growth, we use numerous *ex-situ* characterization techniques such as x-ray diffraction (XRD), variable angle spectroscopic ellipsometry (VASE), and piezoforce response microscopy (PFM) to examine thin film quality and dictate the next step in optimization.

2.2.1 Reflection High-Energy Electron Diffraction-RHEED

RHEED uses a 15–25 keV electron beam scattered from the sample at a grazing angle of 1°-3° onto a fluorescent screen to produce a 2-D diffraction pattern. This pattern is indicative of the near surface crystal structure and is often used to show surface reconstructions. The incoming electrons scatter from the crystal potential and diffract according to the Laue condition, where the change in the electron wave vector is equal to an inverse lattice vector, $\mathbf{\Delta k}$ (figure 2.3). This condition is demonstrated using the Ewald sphere construction, a sphere of radius equal to the electron wave vector, $\mathbf{k}$, centered on the origin. The intersection of the Ewald sphere with inverse lattice points indicates an allowed diffraction condition

$$\Delta k = k' - k \quad . \tag{2.1}$$

The high energy electrons used in RHEED cause the Ewald sphere to be flat enough that it intersects many lattice conditions giving a 2-D image of the inverse lattice on the fluorescent screen.

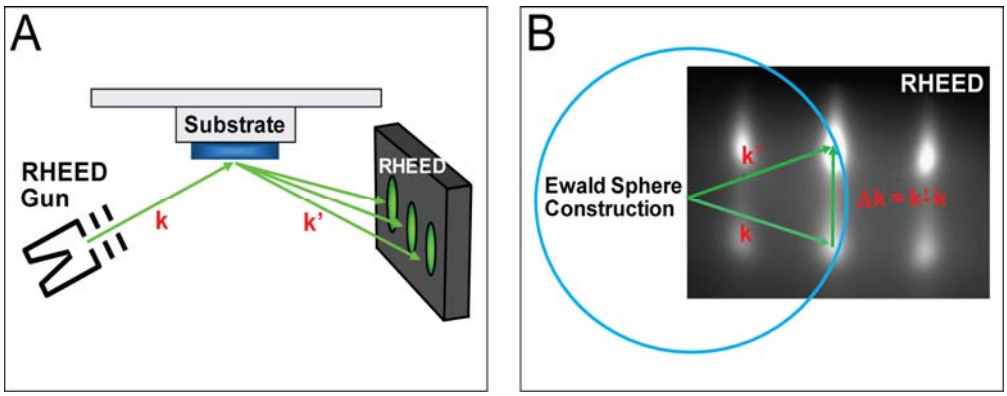

Figure 2.3. Reflection high-energy electron diffraction. (A) Schematic of *in situ* RHEED showing how the Laue condition results in diffraction spots on the luminescent screen. (B) Ewald construction showing the diffraction conditions that result in bright spots in the RHEED pattern.

RHEED patterns are generated by electron scattering from the crystal lattice potential. It is possible, therefore, to calculate the RHEED pattern by solving the Schrödinger equation for the interaction of electrons with the crystal potential V(r)

$$\nabla^2\Psi(r)+\left(V(r)+k^2\right)\Psi(r)=0 \quad . \tag{2.6}$$

Using a semi-infinite crystal scattering potential leads to simple Bloch function solutions of the form

$$\Psi(r)=\sum_k \Psi_k(r)\exp[ik\bullet r] \quad . \tag{2.7}$$

The solutions to the Bloch expansion are taken over all inverse lattice vectors **k** to satisfy the Laue condition for an electron to scatter into a different mode. Solving the dynamical scattering problem can be done computationally and leads to information about the RHEED spot intensities and shapes. A wealth of information regarding film crystallinity, grain size, surface reconstructions, and surface morphology is contained in RHEED spot shapes and intensities.

Kinematical simulations can be used to reconstruct RHEED spots for a given material, angle of incidence, grain size, and grain orientation distribution. From these simulations, a qualitative understanding of RHEED spot shape can be developed.

Simulations show that RHEED spot widths are inversely proportional to grain size and height is inversely proportional to electron penetration depth. The out-of-plane grain distribution is proportional to the width of the central diffraction spots. In-plane-orientation requires analysis, at various in-plane angles, of the spot intensities, a rocking curve. This analysis, developed by *Brewer et al.*, has been used to characterize IBAD MgO growth and as a heuristic to qualitatively characterize other thin films throughout this work.

2.2.2 Piezoresponse Force Microscopy-PFM

There are a variety of powerful scanning probe techniques based on deflection of a cantilever tip from the sample surface. Using this geometry with some modification, the surface roughness, electrical and mechanical characteristics can be investigated. One such specialized use is PFM (figure 2.4). PFM uses an atomic force microscopy (AFM) setup equipped with conducting tips to apply an AC voltage in the 1–5 V range to the sample surface. A lock-in amplifier is used to detect the deflection due to the local piezoelectric response. Grain-by-grain response is monitored using the conductive AFM tip to scan the surface. This is contingent upon the film having a suitable backside electrode, meaning all samples must be grown on conductive substrates. Local piezoelectric hysteresis loops may be obtained by sweeping a DC bias across the sample and recording the piezoresponse (figure 2.5).

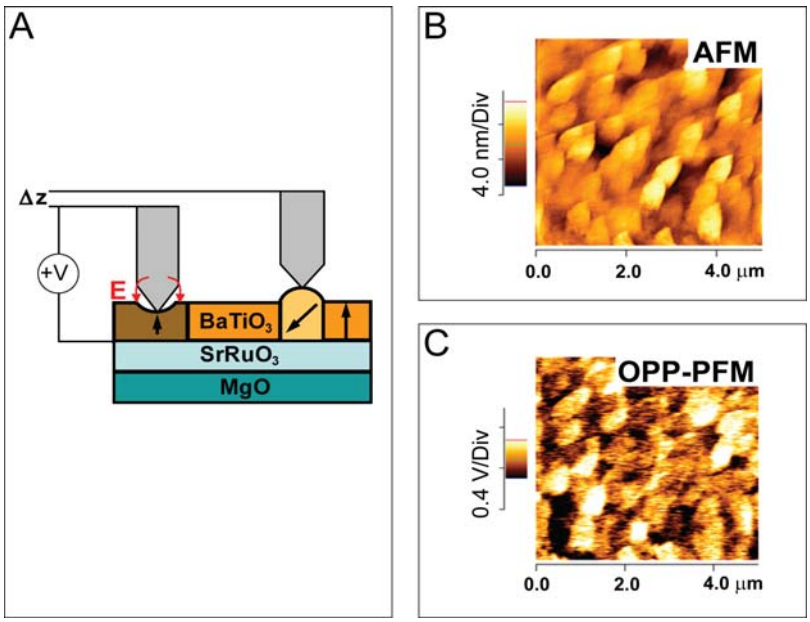

Figure 2.4. Piezoresponse force microscopy. (A) Schematic of PFM showing the cantilever tip deflection. Cantilever deflections due to both surface morphology and polarization domains are detected simultaneously. (B) AFM and (C) out-of-plane polarization maps of a BTO thin film grown on conductive SRO.

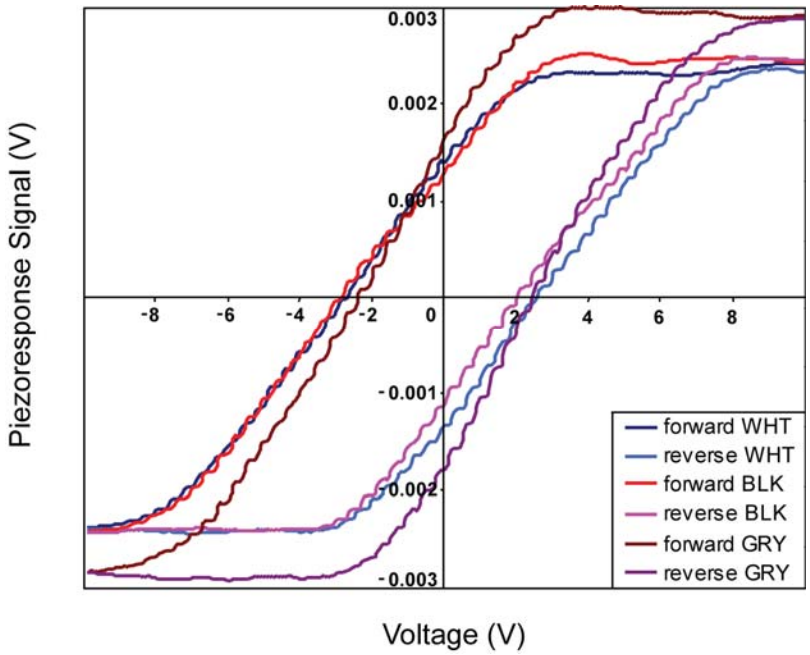

Figure 2.5. Hysterisis loops. Local piezoresponse hysterisis loops for three distinct domains in a BTO thin film. Labeled WHT, BLK, and GRY, these domains have polarizations leading to PFM displacements with Δz negative, positive, and zero. PFM loops show that all three domain types exhibit piezoelectric activity.

In PFM, the signal is recorded as **Acos(θ)**, where **A** is the amplitude of the first harmonic signal, which provides information about the magnitude of the piezo-coefficient, $\mathbf{d_{33}}$, in the measured z-direction, and **θ** is the phase shift between the AC voltage applied through the tip and the piezoresponse which determines the direction of polarization. Equation (2.8) relates this signal to the field induced strain.

$$A\cos\theta = -\left(\frac{dC}{dz}\frac{1}{k_{lever}}\right)(V_{dc} - V_c)V_{ac} \pm d_{33}V_{ac} \tag{2.8}$$

Throughout this work, when appropriate, we use AFM and PFM to confirm the domain activity in thin ferroelectric films. AFM is used extensively to compare surface morphology from sample to sample, especially for optical applications where surface scattering can be an issue. PFM also determines the domain size, polarization orientation, and switching fields.

2.2.3 Variable Angle Spectroscopic Ellipsometry–VASE

Ellipsometry is an optical characterization technique for thin film materials that uses linearly polarized light scattered from the sample and collected through a rotating polarizer. The incident light interacts with the film which imparts both phase and rotation to the scattered signal. The nature of this interaction depends on the complex index of refraction of the material, $\tilde{\mathbf{N}} = \mathbf{n} + \mathbf{i\kappa}$. The complex index, $\tilde{\mathbf{N}}$, is comprised of the real index of refraction, **n**, and the extinction coefficient, **κ**. The real part of the index is related to the phase velocity of light in the material while the extinction coefficient determines how quickly the light will be absorbed by the material.

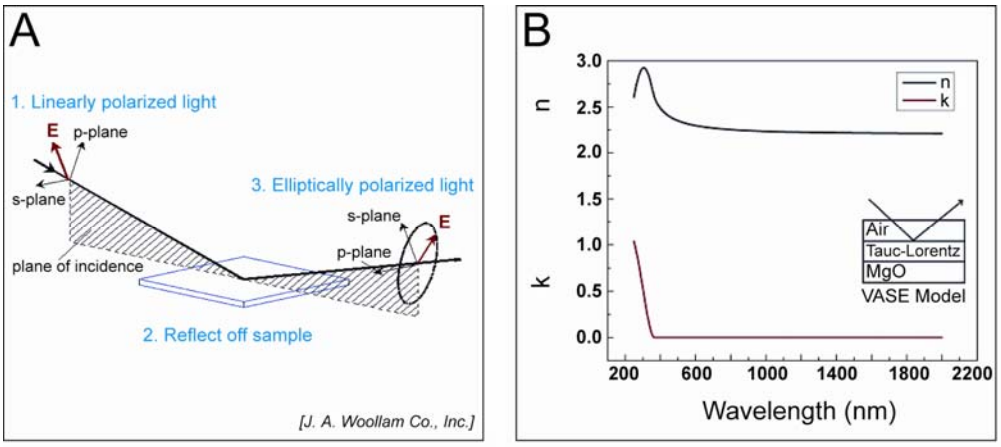

Figure 2.6. Ellipsometry. (A) Linearly polarized light is scattered from the sample and detected through a polarizer, Ψ and Δ are the measured quantities. (B) Ψ and Δ are used to extract **n** and **κ** from each layer with the application of a suitable optical model.

Ellipsometry examines both the reflection and transmission properties of the sample of interest. Reflections from each interface in a material stack are governed by the Fresnel equations and the total reflection coefficient can be derived for s- and p-polarizations as

$$R^p = \frac{r_{12}^p + r_{23}^p \exp(-i2\beta)}{1 + r_{12}^p r_{23}^p \exp(-i2\beta)} \quad , \quad R^s = \frac{r_{12}^s + r_{23}^s \exp(-i2\beta)}{1 + r_{12}^s r_{23}^s \exp(-i2\beta)} \quad , \tag{2.9}$$

where $\mathbf{r_{ab}}$ are the Fresnel reflection coefficients from the interface between a and b, and

$$\beta = 2\pi\left(\frac{d}{\lambda}\right)\tilde{N}_2 \cos\phi_2 \quad . \tag{2.10}$$

Here, **d** is the layer thickness, **λ** the wavelength of light, $\tilde{\mathbf{N}}_2$ is the complex index of the layer, and $\boldsymbol{\phi_2}$ is the phase shift due to the layer. Equation (2.9) is explicit for a three-layer stack but can be generalized to an arbitrary number of material layers.

These represent the total reflection coefficients for a single film, two interfaces and three materials; denoted 1, 2, and 3. Using the ratio of these reflectance coefficients, $\boldsymbol{R^p}$ and $\boldsymbol{R^s}$, and including the possibility of a phase shift from each interface leads to the general equations for ellipsometry, **Ψ** and **Δ** as

$$\Delta = \delta_1 - \delta_2 \quad , \quad \tan\Psi = \frac{\left|R^p\right|}{\left|R^s\right|} \qquad , \tag{2.11}$$

where δ_1 and δ_2 are the phase difference between the s- and p-waves before and after reflection. For a single layer, knowledge of Ψ and Δ is sufficient to find **n** and κ. Multiple layers can be modeled using equations for the dielectric function of the materials involved. Assuming the instrument is working properly, the measured Ψ and Δ are always correct. The optical properties and thickness of a thin film on a substrate material can be extracted using an appropriate model.

The complex index of refraction is dependant on the wavelength of light being considered. Spectroscopic ellipsometry is often used to describe $\tilde{N}(\omega)$ in the UV-visible-near-infrared regions. Spectroscopic ellipsometry data is necessary to model the wavelength dependence of $\tilde{N}$. The most common model used to fit Ψ and Δ was developed by Cauchy in 1830.

$$n(\lambda) = n_0 + \frac{n_1}{\lambda^2} + \frac{n_2}{\lambda^4} \tag{2.12}$$

The Cauchy model works well for dielectrics in the visible region, far from the band gap of the material, where **n** varies only slightly and κ is approximately zero. A more rigorous treatment of the complex dielectric shows that the real and complex parts are not independent. The Kramers-Kronig relation relates these two parts as follows,

$$n(E) - 1 = \frac{2}{\pi} P \int_0^\infty \frac{E' k(E')}{E'^2 - E^2} dE' \qquad , \tag{2.13}$$

where **E** is the energy, and **P** is the Cauchy principal value. Simple models, like that of Cauchy, do not satisfy this physical relationship, but by taking into account more of the physics of light-matter interactions, Kramers-Kronig consistent models may be developed. One such model by Lorentz considers the relationship between atomic polarizability and the

nature of electromagnetic radiation to define the dielectric function in terms of multiple oscillator functions. In terms of ε_1 and ε_2, the Lorentz formulation reduces to

$$\tilde{\varepsilon} = 1 + \frac{4\pi e^2}{m} \sum_k \frac{N_k}{\left(\omega_k^2 - \omega^2\right) - i\Gamma_k \omega} \quad , \tag{2.14}$$

with $\tilde{\varepsilon} = \tilde{N}^2$, ***e*** is the magnitude of the electronic charge, **Γ** the damping, $\mathbf{N_k}$ is the density of oscillators in the model, **m** the electronic mass, $\boldsymbol{\omega_k}$ is the resonant frequency in the absence of damping and **ω** the pumping frequency. Variations on the Lorentz oscillator function are used throughout this thesis to model dielectric functions and extract **n** and **κ**. Knowledge of **$\tilde{N}(\omega)$** for the thin film materials used here is necessary to design the optical devices.

2.3 Conclusions

MBE and PLD were used extensively in this thesis work to develop oxide thin films for mechanical and optical applications. MBE offers a precise, high quality technique for thin film deposition. MBE, however, requires UHV conditions, and deposition is very slow, making initial investigations prohibitively long. PLD is a faster deposition technique which only requires that a sintered or pure elemental target can be made of the material. Rapid, accurate characterization of thin films is necessary during the initial stages of deposition. RHEED and XRD are the two best techniques and should be applied liberally.

Chapter 3
Oxide Thin Film Growth Techniques

The intent of this chapter is to present work done to develop deposition techniques for thin films of various oxide materials. These films were initially intended as a means for investigating domain switching in ferroelectrics for high work per volume ferroelectric MEMS. As such, they were designed to be integrated with Si CMOS processing. Integration with Si relies heavily on IBAD MgO as a template for growth of biaxially textured oxides. We will begin, therefore, by discussing IBAD MgO films, followed by MBE of BTO. Following work on MBE growth, we use PLD to optimize growth of SRO thin films, to be used as a lattice matched conductive oxide electrode in device designs. Film stacks of BTO on SRO on IBAD MgO on amorphous Si_3N_4 on Si represent the successful integration of active oxide ferroelectric materials for mechanical and optical applications. Finally, the deposition and optimization of films of VO_2, via PLD, for optical metamaterial applications is discussed.

3.1 Ion Beam Assisted Deposition—MgO

IBAD films were deposited in an UHV chamber using an e-beam evaporator to deposit MgO onto amorphous Si_3N_4 substrates oriented 45° to an Ar ion source. We use a linear, 4-pocket, Temescal e-beam evaporator. The e-beam evaporator is housed separately from the main UHV chamber, approximately 36 inches from the substrate. The copper crucibles hold 5 cm^3 of MgO. The e-beam is created via a hot filament adjacent to the crucible and focused onto the material by two magnets. The filament current is controlled through a high voltage power supply and the housing is water cooled. A quartz crystal monitor is used to measure the deposition rate of the MgO. The minimum deposition rate to achieve biaxially textured MgO films is 1.5 Å/sec, and the optimal rate, with regard to orientation and grain size, is 2.0 Å/sec.

The IBAD process takes place at room temperature with 1.0 X 10^{-4} Torr background Ar pressure to facilitate the ion beam. Ar ions are supplied using a Kauffman ion source. Ar is supplied via a leak valve through the Kauffman source and ionized between two plates held at high voltage. The Ar ions are accelerated toward the substrate due to a negatively

biased mesh at the base of the gun. A Faraday cup is used to calibrate the flux of the incoming ions. The optimum ion current is 13.0 X 10^{-6} amps for the deposition parameters reported here.

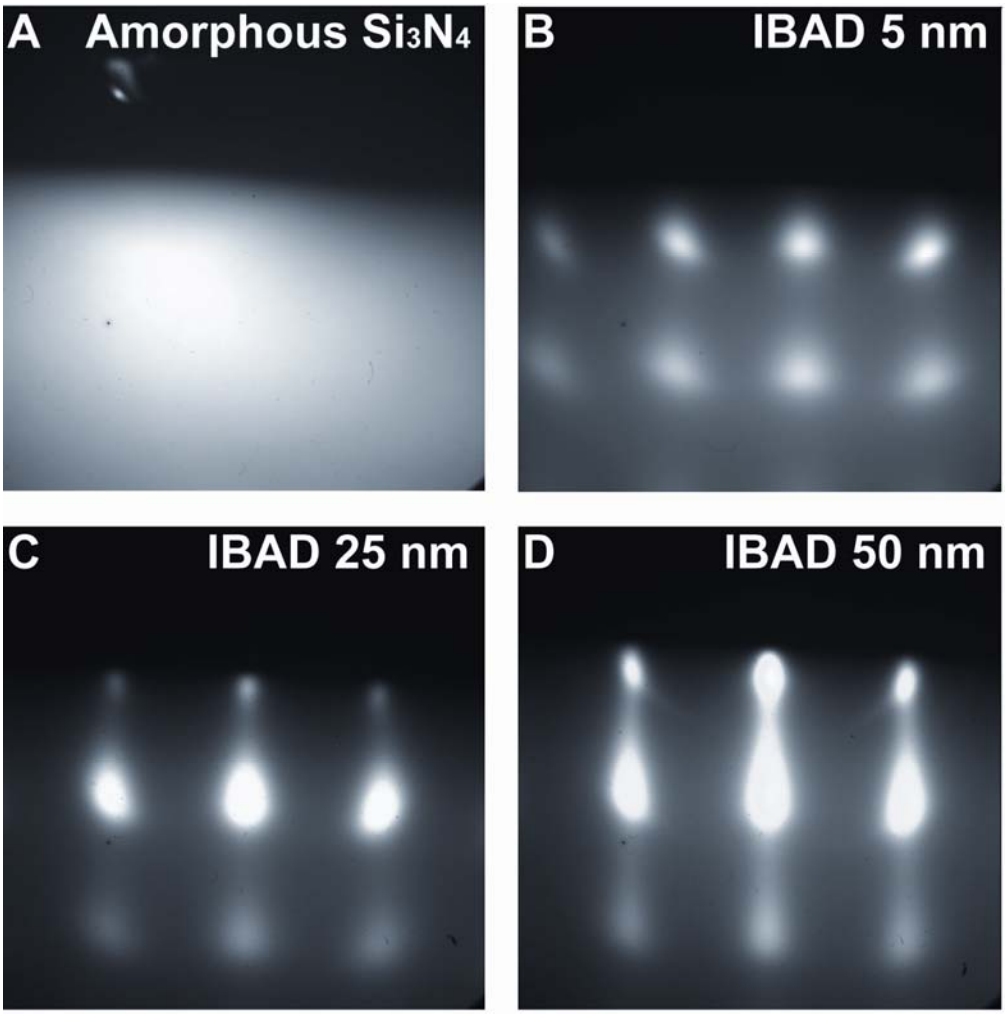

Figure 3.1. Ion Beam Assisted Deposition MgO—RHEED development. RHEED patterns showing texture development. (A) Amorphous Si_3N_4 substrate. (B) Room temperature IBAD MgO, approximately 5 nm. (C) IBAD MgO approximately 25 nm. (D) 650 °C Homoepitaxial MgO deposition, approximately 50 nm total thickness.

In situ RHEED is used to monitor the texture development during IBAD. Figure 3.1 shows typical biaxial MgO texture during the process. The initial RHEED pattern is diffuse due to the amorphous nature of Si_3N_4. After approximately 25-30 Å of MgO deposition, diffraction spots appear in RHEED indicating texture development. Following the deposition of 75-100 Å of MgO, the RHEED pattern no longer changes with further deposition at room temperature. Following heterogeneous growth of MgO on Si_3N_4, we deposit MgO homoepitaxially via further e-beam deposition at 650 °C. The IBAD sample is annealed at 650 °C for one hour before MgO is evaporated at a rate of 1.0 Å/sec. The further brightening and narrowing of the RHEED pattern indicates that the grain orientation is improving. X-ray diffraction confirms the (200) orientation of the IBAD MgO films and inherited texture from heteroepitaxial films (figure 3.2).

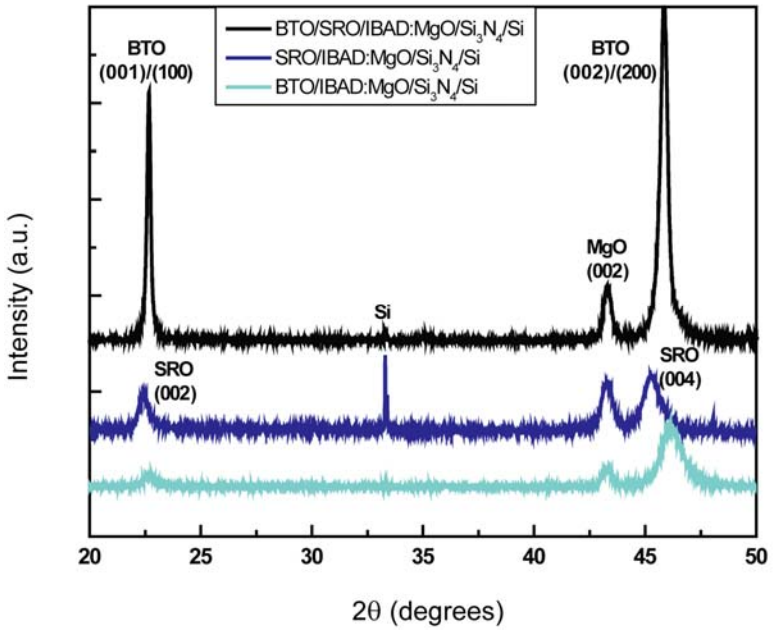

Figure 3.2. Ion Beam Assisted Deposition MgO—x-ray diffraction comparison. θ-2θ XRD scans of films deposited on IBAD MgO/Si_3N_4/Si substrates show the biaxial texture inherited from the underlying IBAD MgO. Texture is inherited in MBE BTO (light blue), PLD SRO (dark blue), and BTO on SRO (black) samples grown on IBAD MgO.

Samples grown at these conditions validate IBAD MgO films as an epitaxial template for integrating complex oxides with amorphous substrates. IBAD MgO films grown with these parameters have been used as templates for MBE BTO, PLD BTO, and PLD SRO. In

addition to growth on Si_3N_4 films deposited on Si wafers, we have grown IBAD MgO on 50-100 nm Si_3N_4 freestanding films (figure 3.3). Arrays of these Si_3N_4 films, commonly used as transmission electron microscopy (TEM) grids, were used as relaxed substrates for mechanical and optical studies on BTO thin films.

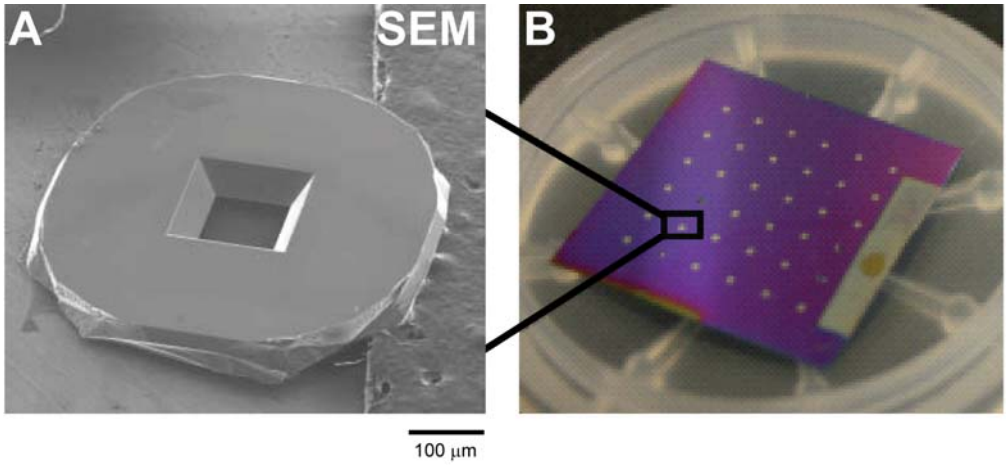

Figure 3.3. Si_3N_4 transmission electron microscopy arrays. (A) Scanning electron microscopy image of a free standing Si_3N_4 film. The photo shows the TEM window from behind, through the back-etched silicon wafer. (B) An array of these films coated with IBAD MgO and CVD PTO.

Growth and characterization of IBAD MgO films has shown that they are suitable as biaxially oriented templates for complex oxides. These films have been optimized for growth on Si_3N_4 on bulk substrates, Si_3N_4 freestanding films, silicon dioxide, and bulk silicon. The most important condition for successful growth of IBAD MgO has been the roughness of the substrate, less than 5 nm RMS roughness, as determined by AFM, is required. These films were used extensively as templates for work done by El-Naggar and Ruglovsky (*El-Naggar 2006, Ruglovsky 2007*) to study orientation effects on mechanical properties in ferroelectric thin films grown by MBE and PLD.

3.2 MBE BTO

MBE of BTO is carried out in the UHV chamber previously discussed for IBAD MgO. This allows for monolithic deposition without breaking vacuum. The base chamber pressure is 1 X 10^{-8} Torr with a background comprised entirely of oxygen supplied from a leak valve attached to a RF plasma source. The chamber is equipped with two Knudsen effusion cell sources, elemental Ba and Pb. These k-cells are small crucibles filled with a pure element that is resistively heated until it sublimes at a reasonable rate. Ti is supplied from a Varian Ti-Ball sublimation pump.

Traditionally, the elemental flux is calibrated using a quartz crystal monitor, atomic emission spectroscopy, or other analysis. The information is then fed back to a program to control deposition. This is not the case for titanate-based ferroelectrics due to the extreme temperature of the Ti source. The quartz crystal monitor cannot be used to calibrate the titanium flux because the radiative heating raises the temperature higher than the monitor can operate at. It was determined that RHEED oscillations could be used to calibrate growth (figure 3.4).

In situ RHEED oscillations were used to calibrate the flux ratios for Ba and Ti. As atoms are deposited on a flat surface the electron beam begins to scatter and the RHEED spot loses intensity. This continues until the coverage is 50%, at which point the intensity recovers. The intensity of the specular reflection spot is monitored with a CCD camera and software provided by K-Space Associates. Source temperatures were calibrated using this technique to yield equivalent flux rates. Subsequently, a source shuttering program was written in Labview, and calibrated with RHEED, to optimize the flux and improve film stoichiometry. Using these calibrated flux ratios, BTO thin films were deposited on bulk MgO and IBAD MgO substrates. Deposition takes place at 650 °C with 1.5 X 10^{-5} Torr background oxygen pressure. Oxygen was supplied through an RF plasma source operating at 300 Watts. Plasma generated oxygen radicals lead to better oxygen stoichiometry and hence, much higher optical quality BTO films, to be discussed in chapter 5.

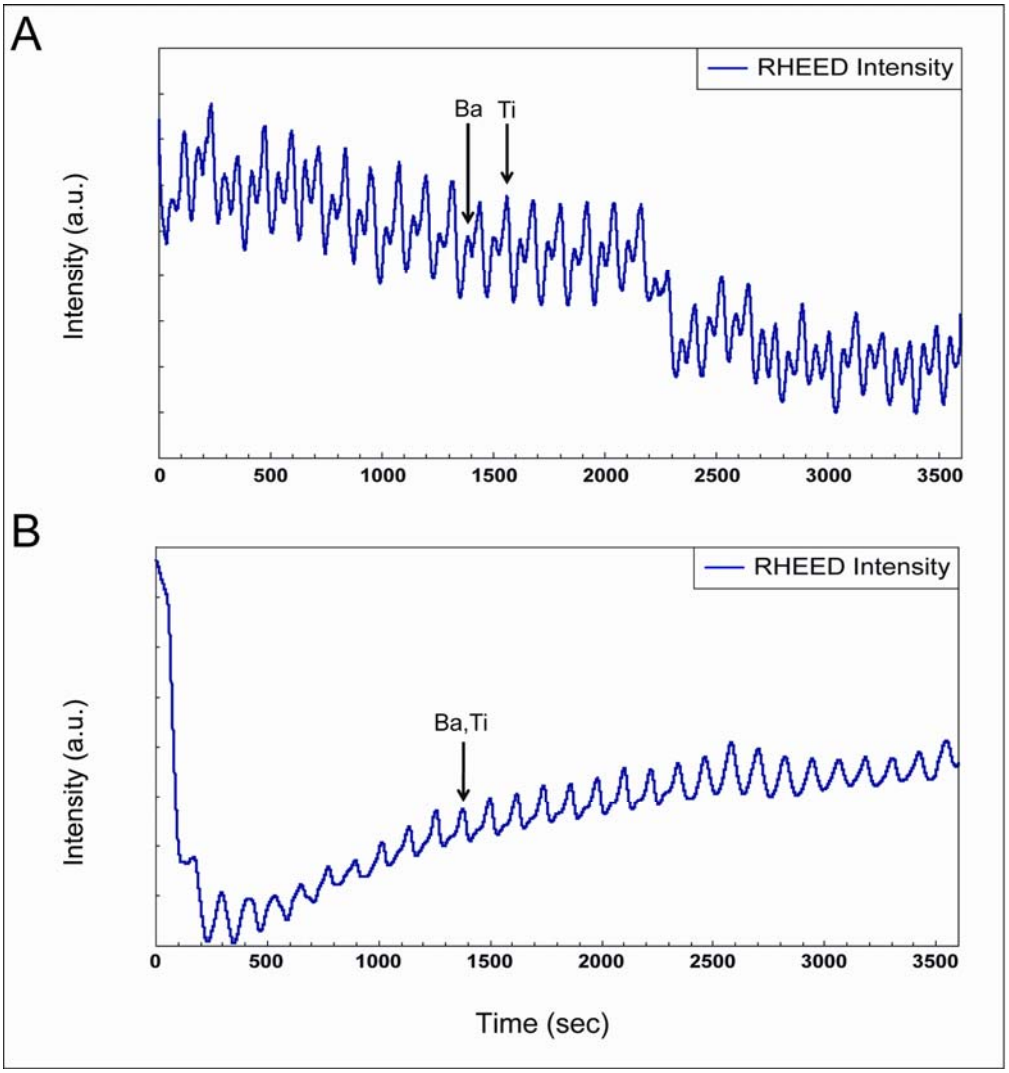

Figure 3.4. RHEED intensity oscillations. Intensity oscillations of the specularly reflected beam are monitored during BTO growth. (A) The intensity peaks of during barium oxide and titanium dioxide deposition are separated when the fluxes are not equal. (B) Calibrated fluxes used for stoichiometric growth of BTO.

In addition to calibrating material fluxes, RHEED is also an indicator of surface crystal quality. Monitoring the RHEED pattern of the substrate during the first few minutes of growth is sufficient to know what each growth conditions will yield. MBE BTO films on bulk MgO and IBAD MgO were characterized by *in situ* RHEED, typical examples of film quality are shown in figure 3.5. Typical θ-2θ XRD patterns for BTO on bulk MgO and IBAD MgO are shown in figure 3.6.

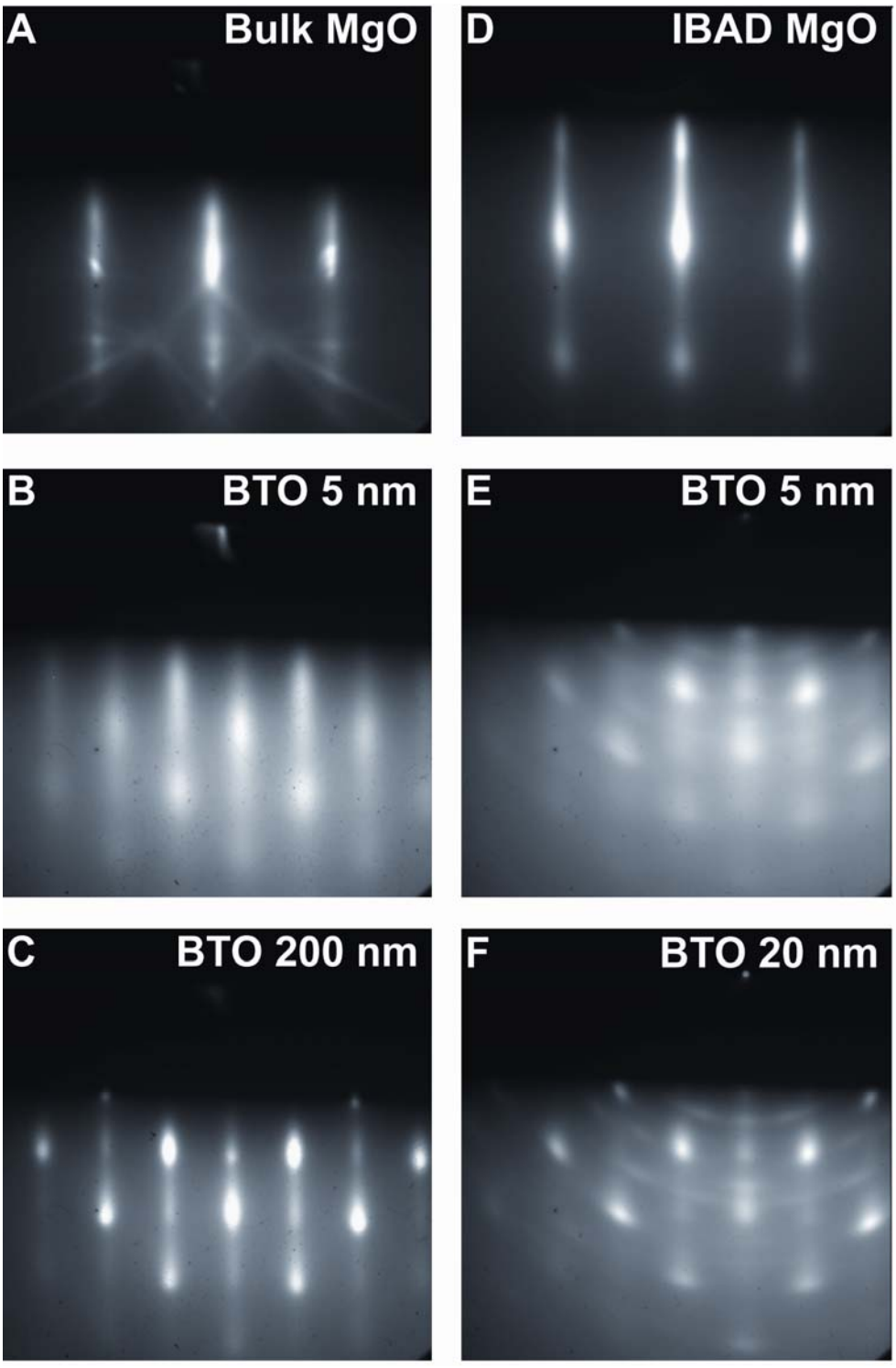

Figure 3.5. Barium titanate RHEED comparison. BTO grown on bulk MgO begins to show a RHEED pattern after approximately 5 nm of growth. BTO films are highly oriented on both bulk MgO and IBAD MgO. We see a small degree of polycrystalline BTO begin to develop on the IBAD MgO substrate after 20 nm.

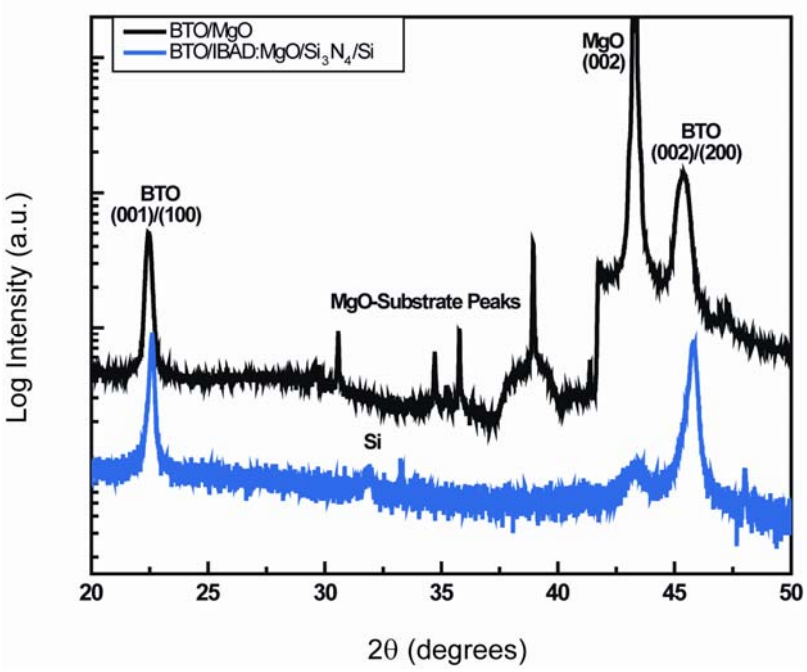

Figure 3.6. Barium titanate x-ray diffraction comparison. θ-2θ XRD scans of MBE BTO on bulk MgO (black) and IBAD MgO (light blue). Both samples show only the (001)/(100) phase.

After growth, XRD can be used to confirm the crystal orientation and look for other phases and orientations. Having confirmed the crystal orientation and phase of BTO on IBAD MgO templates, as well as bulk MgO and BTO on SRO films deposited on similar samples, we turn to AFM and PFM to investigate the surface morphology, piezoelectric and ferroelectric activity. Typical AFM and PFM images are shown here in figure 3.7. In general, RMS roughness of MBE BTO thin films was less than 5 nm. Grain size was in the range of 200–500 nm for samples on bulk MgO and 100–300 nm for samples grown IBAD MgO. Local piezoresponse hysteresis loops can be used to show grain-by-grain polarization response (figure 3.8). AFM/PFM characterization of mechanically active oxide thin films will be discussed further in chapter 4.

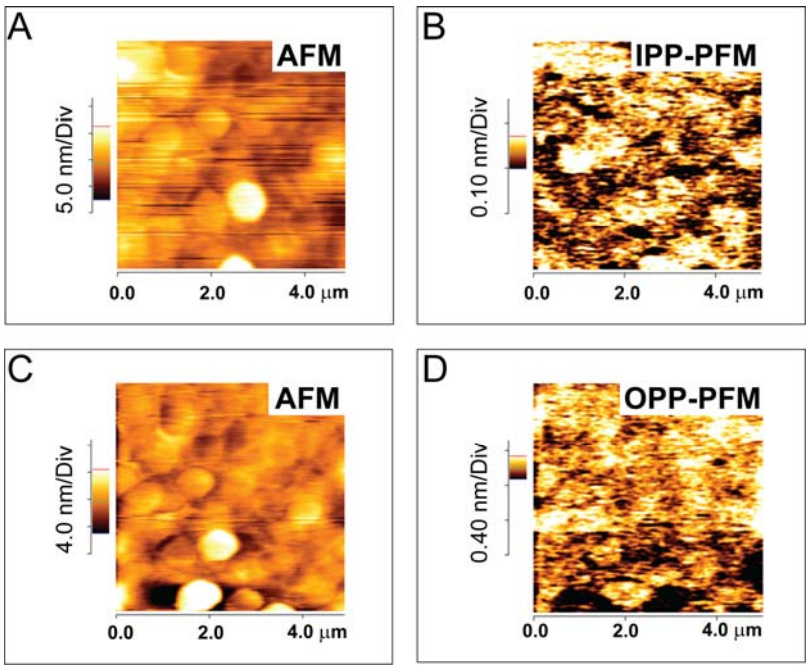

Figure 3.7. Barium titanate AFM/PFM. AFM and PFM images for MBE BTO on PLD SRO on bulk MgO. AFM shows grains approximately 300-500 nm in size. In-plane and out-of-plane polarization maps show the orientation of the ferroelectric domains in the BTO thin film.

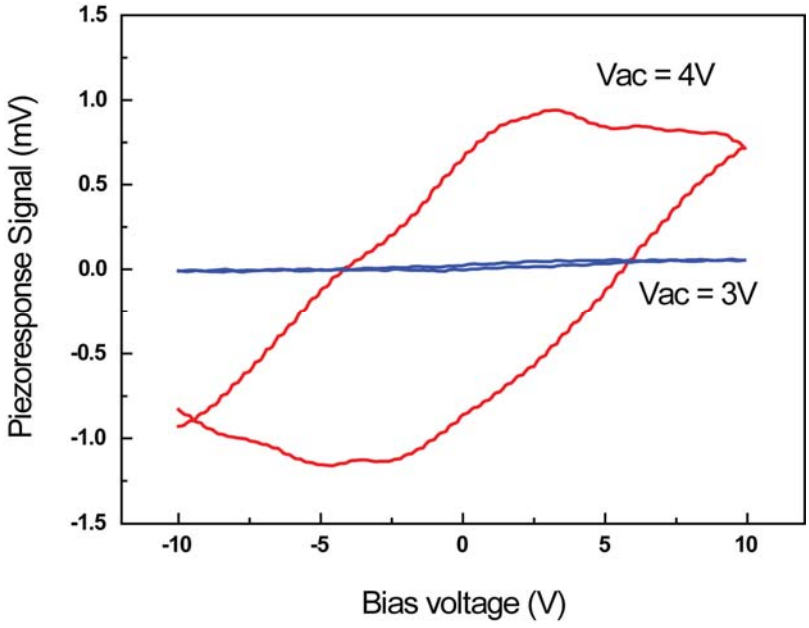

Figure 3.8. Piezoresponse hysterisis loops. A local hysterisis loop shows that the switching voltage for a MBE BTO / PLD SRO / MgO sample is approximately 4 V.

3.3 PLD BTO, STO, SRO, and VO_2

PLD is a physical deposition technique that utilizes a high power laser pulse, incident on a sintered target, to create an atomized plume of material that deposits on a heated substrate. As discussed earlier, we use PLD for its versatility in terms of materials and superior deposition rate. In this section we will report typical results for optimized growth of BTO, STO, SRO, and VO_2 by PLD.

PLD BTO and STO thin films are grown at 650 °C at 5 mTorr oxygen from a sintered target, 99.9% pure $BaTiO_3$, and 99.9% pure $SrTiO_3$. Growth of BTO on bulk MgO and STO substrates was investigated. θ-2θ XRD data show that the thin film quality is similar to MBE samples for BTO (figure 3.9) and highly oriented STO (figure 3.10).

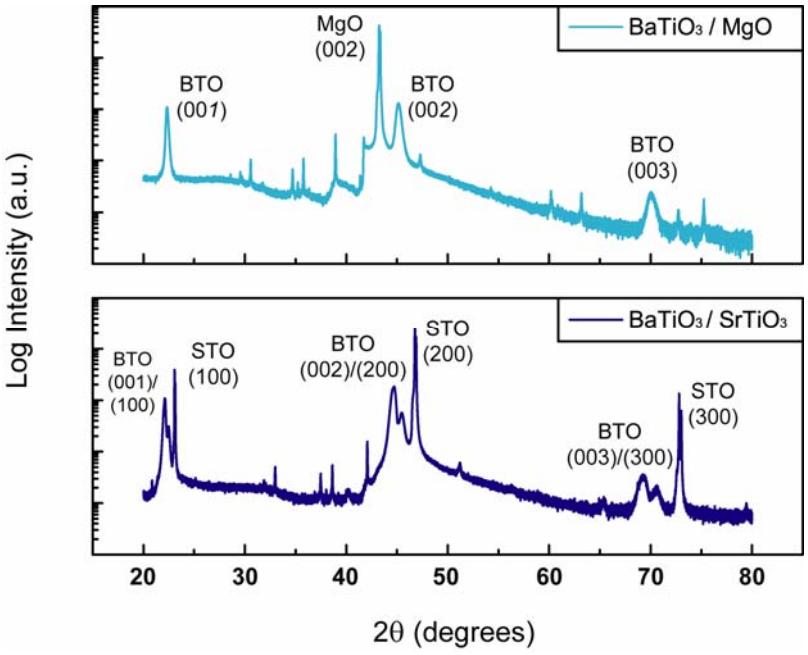

Figure 3.9. Pulsed laser deposition barium titanate. θ-2θ XRD scans of PLD BTO films on MgO (light blue) and STO (dark blue). BTO/MgO films are compressively stressed and show (00*l*) predominantly shifted toward the c-axis orientation. PLD BTO growth on STO shows both a- and c-axis orientation.

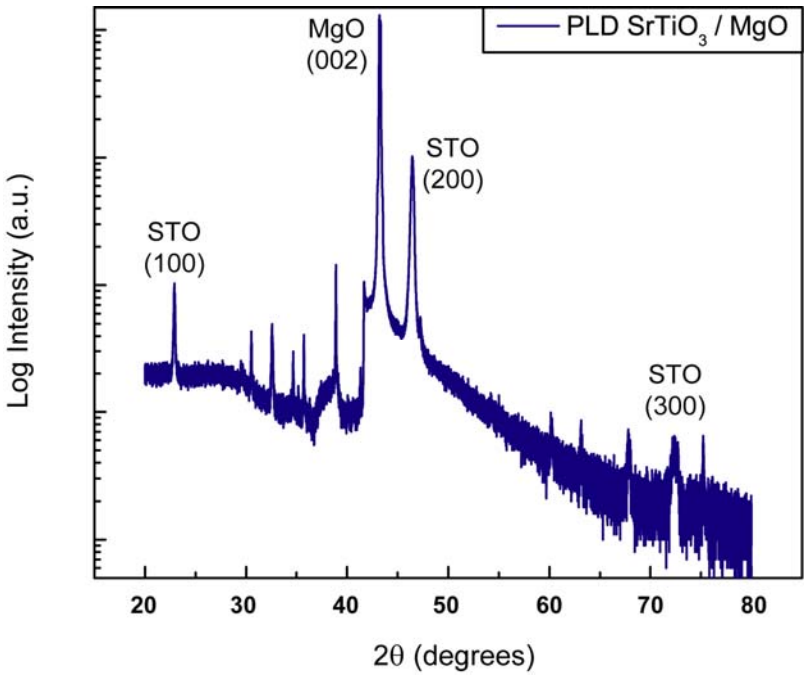

Figure 3.10. Pulsed laser deposition strontium titanate. θ-2θ XRD scan of PLD STO film on MgO grown at 650 °C in 5 mTorr oxygen partial pressure. 18,000 laser pulses with 300 mJ at 10 Hz yields approximately 200 nm thick films.

An advantage of PLD growth is the convenience of a faster deposition rate allowing for faster sample growth and characterization. The Neocera PLD system has the ability to deposit from up to six different targets. After optimizing growth of BTO and STO, we deposited a compositionally graded film based on both materials. This was done using a script to rotate each target after a set number of pulses. The desired ratios were 60:40, 70:30, and 90:10 BTO:STO, grown in three stages. θ-2θ XRD data show a highly oriented film with peaks shifted toward the (*l*00) 2θ values (figure 3.11). Applications of the compositionally graded BTO/STO films grown here include use as temperature insensitive dielectrics (*El-Naggar 2006*).

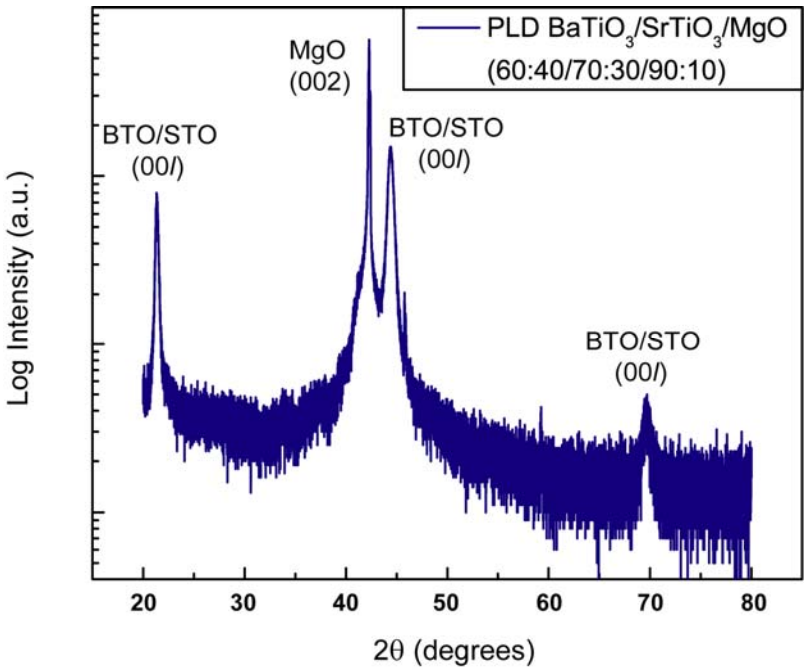

Figure 3.11. Compositionally graded barium strontium titanate. θ-2θ XRD scan of PLD BTO and STO deposited in three phases, each with a different number of laser pulses on each target. Used this way, PLD enables multilayer deposition of complementary materials leading to graded film composition.

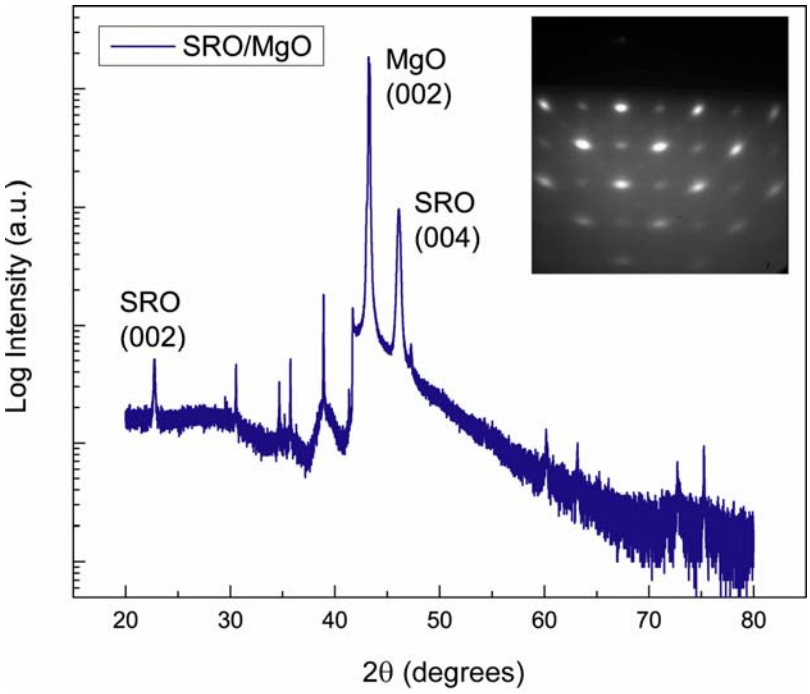

Figure 3.12. Pulsed laser deposition strontium ruthenate. θ-2θ XRD scan of SRO thin film on MgO showing the highly-oriented (00*l*) morphology. (Inset) The *ex situ* RHEED pattern also confirms the high degree of epitaxy.

PLD SRO thin films are grown at 650 °C at 200 mTorr oxygen from a sintered target, 99.9% pure $SrRuO_3$ (figure 3.12). The full texture of the PLD SRO film was investigated further by diffracting from planes that are away from the normal axis. Pole figures of SRO on MgO with 2θ set at 32.2° show four peaks corresponding to the (00*l*) orientation (*El-Naggar 2006*).

Finally, PLD BTO was grown on PLD SRO on MgO substrates to show a single epitaxial film stack with an integrated oxide electrode layer. θ-2θ XRD data show that the heteroepitaxial film stack retains the (00*l*) orientation from the bulk MgO substrate and no other phases are present (figure 3.13). PLD BTO on SRO on MgO substrates are primarily investigated in chapter 6 as the active element in a tunable plasmon interferometer. The final active oxide material investigated in this thesis is vanadium (II) oxide.

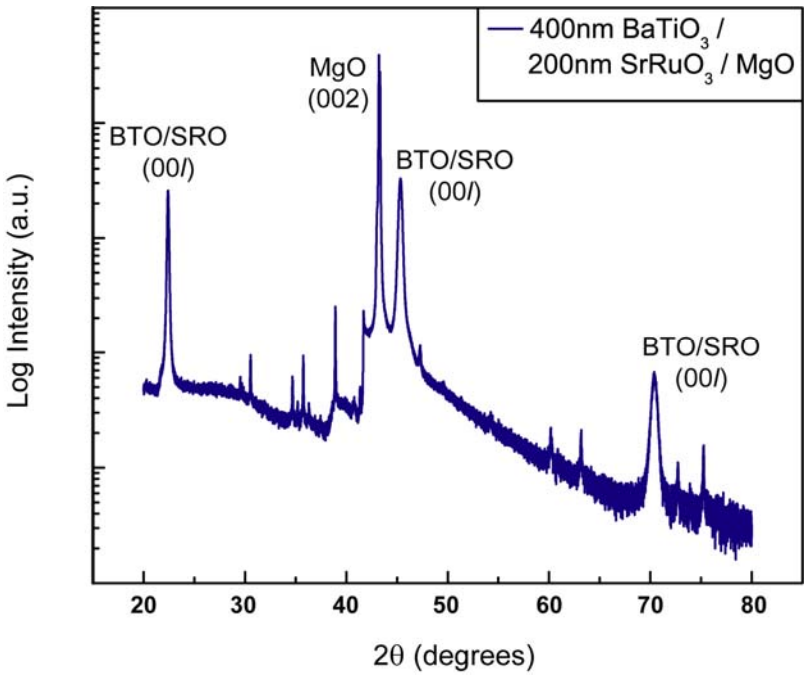

Figure 3.13. Pulsed laser deposition barium titanate on strontium ruthenate. θ-2θ XRD scan of BTO/SRO thin film on MgO showing the highly oriented (00*l*) morphology.

Vanadium (II) oxide (VO_2) thin films were developed using PLD. VO_2 thin films are grown on sapphire (c-plane Al_2O_3) between 550–600 °C using a pure vanadium target. VO_2 PLD is very sensitive to background oxygen pressure, 12–15 mTorr O_2 is optimum for single phase growth. Straying from either substrate temperature or oxygen pressure leads to V_2O_5 or V_6O_{13} phases. XRD is used to confirm the VO_2 phase on c-plane sapphire (figure 3.14). With single phase VO_2 thin films, we can begin to design optical devices that take advantage of the metal-insulator transition at approximately 70 °C. This transition is accompanied by a change in the crystal structure, optical properties and conductivity. This will be discussed in chapters 5 and 7.

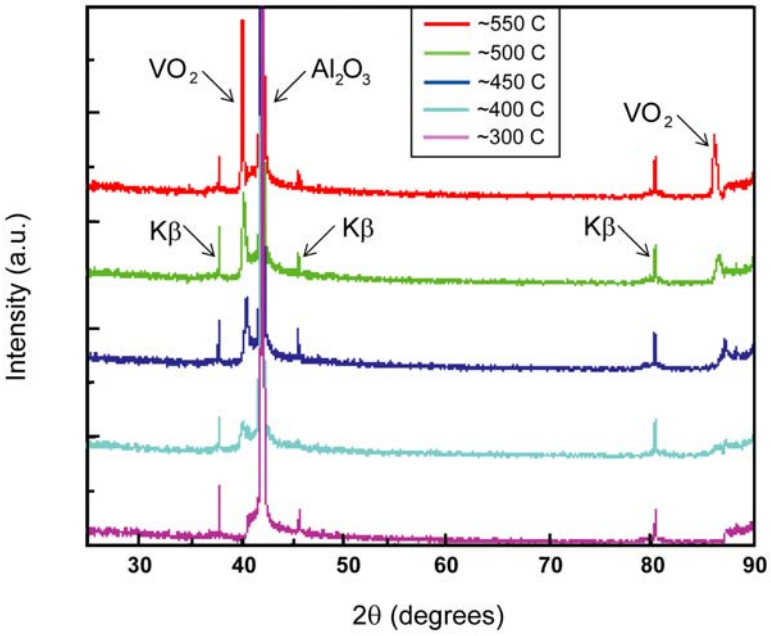

Figure 3.14. Vanadium (II) Oxide x-ray diffraction. Temperature dependence of VO_2 crystallinity. (002)/(020) single phase VO_2 becomes dominate above 500 °C. Cu-K_β signal from the XRD are denoted.

3.4 Conclusions

Active oxide thin film deposition techniques have been studied extensively by MBE and PLD. Deposition of BTO has been demonstrated using both techniques. PTO, STO, SRO, and VO_2 have been grown on various substrates using PLD. We have found PLD to be a superior technique for the rapid development of new materials for thin films applications.

Part II

Mechanical and Optical Characterization of Active Oxides

Chapter 4
Active Oxide Thin Films – Mechanical Studies

Mechanical activity in ferroelectric thin films comes from two sources: the piezoelectric effect and 90° domain switching. These two effects were studied in thin films deposited by MBE and PLD. The piezoelectric effect in BTO thin films was characterized by PFM. Orientation effects were investigated as films were deposited on Pt and lanthanum scandium cobalt oxide (LSCO) conductive substrates. Mechanical effects on ferroelectric domains were investigated using nanoindentation on bulk BTO samples[†].

4.1 Orientation Effects on Barium Titanate Polarization

The electrooptic and electromechanical properties of BTO thin films are correlated to crystallographic orientation, phase, domain structure and strain (*Park et al. 1999, Stavistki et al. 2002*). Recent studies of BTO thin films have attempted to utilize the large electrooptic and piezoelectric coefficients for such applications as miniaturized optical modulators for fiber optic based data transmission and a variety of mechanical sensors and actuators (*Petraru et al. 2003, Tang et al. 2003*). Characterization of the nanoscale material properties of ferroelectric thin films is needed for these applications. Recently, PFM has demonstrated the ability to image and characterize ferroelectric surfaces on the nanometer scale (*Auciello et al. 1998, Kalinin et al. 2002a, Kalinin et al. 2004, Zeng et al. 2004*). In the first part of this chapter, we report PFM characterization of BTO thin films used to study the nanoscale domain polarizations.

4.1.1 Barium Titanate Thin Films on Conductive Substrates

PFM has recently been used to image ferroelectric domains and characterize the piezoresponse of thin films (*Harnagea et al. 2002*). As discussed previously, PFM uses the deflection of an AFM cantilever with a conductive tip, under voltage modulation, in contact with the sample surface. The converse piezoelectric effect causes vibrations in the film that are measured as deflections in the cantilever. The magnitude of this deflection is

[†] Material used in this chapter is compiled from work published in references *Kim, Park, Dicken et al. 2005* & *Park, Dicken et al. 2007*.

proportional to the longitudinal piezoelectric coefficient, d_{33}. Understanding the orientation dependence of the piezoelectric constants is important for optimization of electromechanical film properties.

The effects of thin film texture on in-plane and out-of plane polarization in BTO grown on Pt/Ta/SiO2/Si and $La_{0.5}Sr_{0.5}CoO_3$ (LSCO)/Pt/Ta/SiO2/Si were investigated. BTO films were deposited via PLD to thicknesses in the range of 150—250 nm. The substrate temperature and oxygen ambient pressure during growth were 700 °C and 30 mTorr, respectively. The 100 nm LSCO buffer layers used were deposited at 600 °C onto Pt/Ta/SiO2/Si by PLD.

The 3-D polarization vector is reconstructed using RHEED and XRD measurements of crystal orientation. We found a preferred (101) orientation for BTO thin films grown on Pt electrodes compared to both (001) and (101) orientations on LSCO films. Figure 4.1 shows the XRD patterns of 250 nm BTO films grown on Pt/Ta/SiO2 and LSCO/Pt/Ta/SiO2/Si substrates. The BTO films on Pt/Ta/SiO2/Si show polycrystalline, perovskite, morphology, with highly (101) preferred orientation. BTO films on 100 nm LSCO buffered layers show mixed (001) and (101) orientations. XRD shows that the LSCO films are single phase, crystalline, with (100) orientation. The increase in (001) BTO orientation is due to the structural match between pseudocubic LSCO (a = 3.835 Å) and tetragonal BTO (a = 4.0 Å).

RHEED measurements were performed on BTO thin films on Pt and LSCO/Pt electrodes to confirm the surface structure. RHEED patterns show evidence of biaxial texture inheritance from the underlying Pt film in figure 4.2A. Figure 4.2B shows the ring patterns indicative of a polycrystalline BTO film. The elongated RHEED spots are indicative of the (101) and (001) textures compared to the continuous rings in the BTO/LSCO sample.

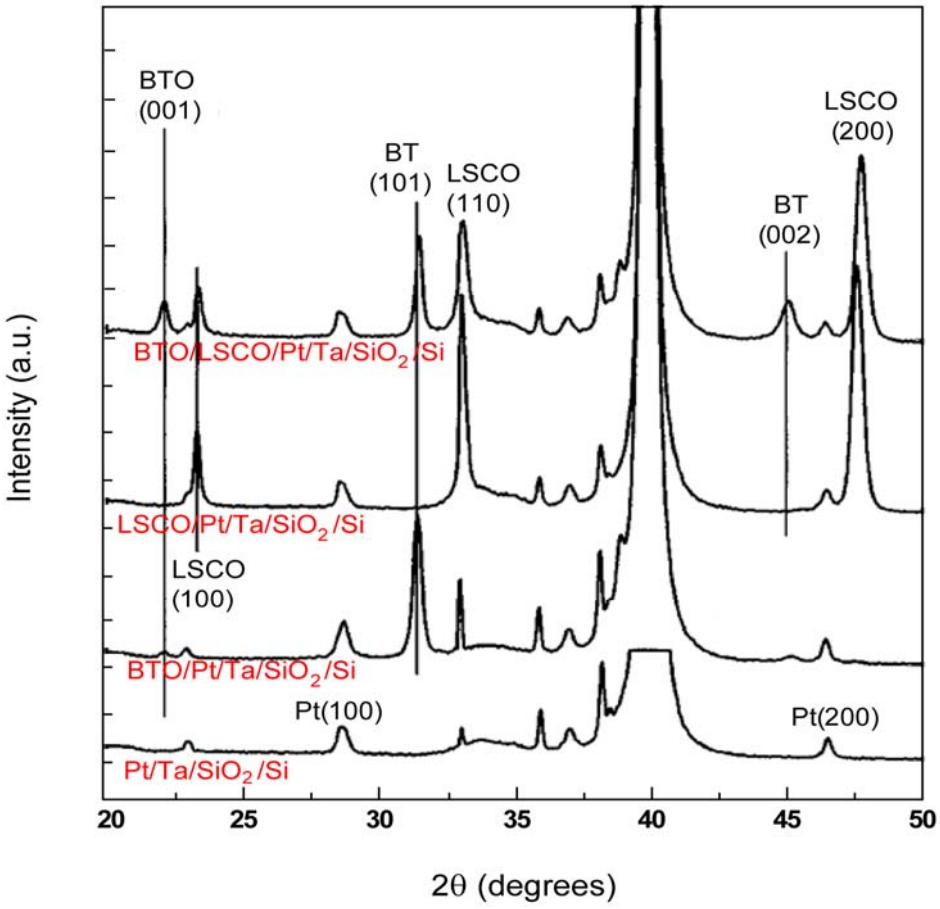

Figure 4.1. Barium titanate on conductive substrates–-x-ray diffraction comparison. (A) $Pt/Ta/SiO_2/Si$ substrate. (B) PLD $BTO/Pt/Ta/SiO_2/Si$ sample. (C) $LSCO/Pt/Ta/SiO_2/Si$ substrate. (D) PLD $BTO/LSCO/Pt/Ta/SiO_2/Si$ sample.

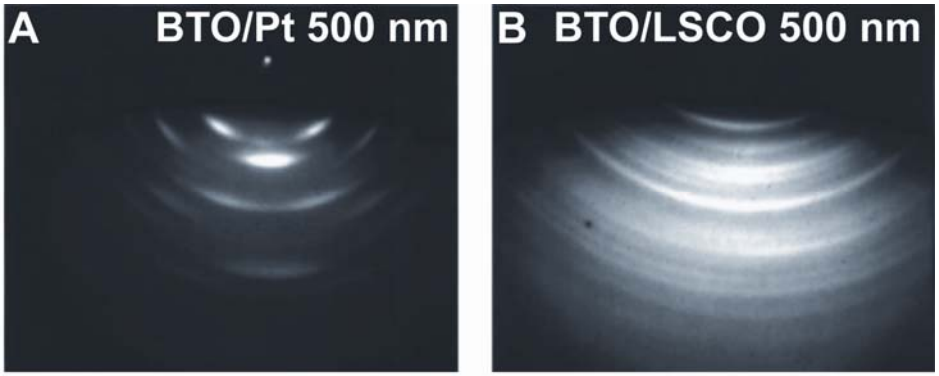

Figure 4.2. Barium titanate on conductive substrates—RHEED comparison. RHEED images of PLD BTO on (A) $Pt/Ta/SiO_2/Si$ and (B) $LSCO/Pt/SiO_2/Si$ substrates.

AFM images of the sample surface morphology are obtained simultaneously with PFM polarization images (figure 4.3). The BTO grain size was 125 nm for films on Pt and 167 nm for films on LSCO. The RMS roughness of a 2 X 2 μm^2 area was 8.4 and 7.7 nm for BTO/Pt and BTO/LSCO, respectively. The out-of-plane and in-plane PFM images in figure 4.3C-F show the grain size-dependent domain distributions of the BTO films. The PFM measurement applies a voltage along the (001) direction through the film using the LSCO/Pt or Pt film as a counterelectrode to the AFM tip. Non-(001) oriented components in the film are investigated by comparing the in-plane and out-of plane signals. We can see the increased in-plane polarization component in the BTO/Pt samples. It is believed that this is due to larger in-plane stresses imparted to the film upon cooling.

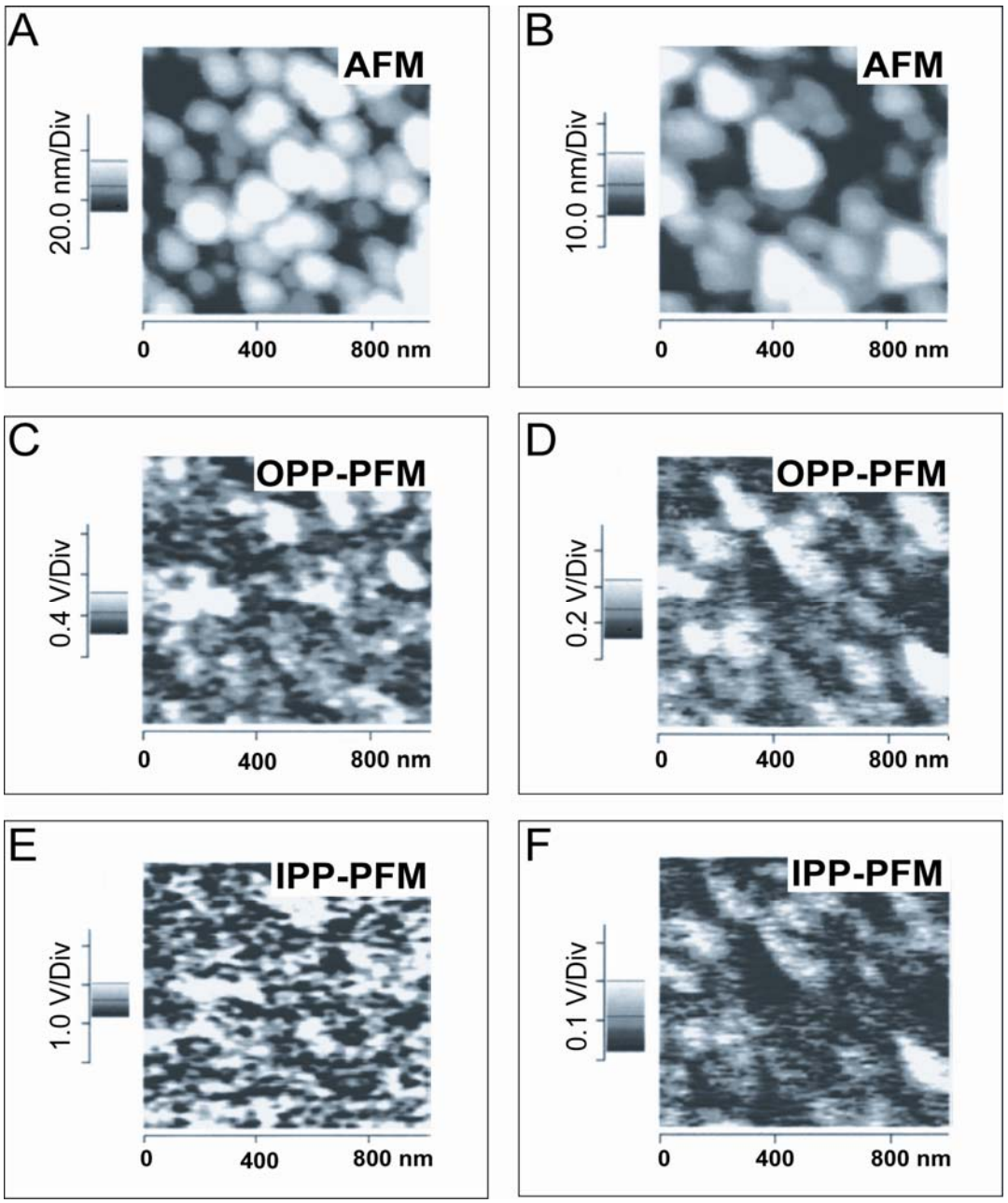

Figure 4.3. Barium titanate on conductive substrates–-AFM/PFM comparison. AFM/PFM images for PLD BTO on Pt (left column) and LSCO (right column) substrates. AFM of (A) BTO/Pt and (B) BTO/LSCO shows grains on the order of 100 and 200 nm respectively. This is expected as the BTO is better lattice matched to LSCO. Out-of-plane polarization PFM of (C) BTO/Pt and (D) BTO/LSCO shows stronger polarization response from BTO films on LSCO. In-plane polarization PFM of (E) BTO/Pt and BTO/LSCO also shows sharper polarization signal from the BTO/LSCO sample.

Finally, to measure the magnitude of the piezoelectric coefficient, $\mathbf{d_{33}}$, local piezoresponse hysteresis loops are measured on the BTO thin films. Figure 4.4 shows the local piezoresponse butterfly loops for BTO films on Pt and LSCO/Pt. Local P-E curves in each measurement show the typical butterfly loops indicative of electric field induced strain. The butterfly loops show the same increased in-plane polarization for BTO/Pt films as in the PFM scans. The slope of the piezoelectric strain curve is used to determine the effective d_{33} values. The preferred crystal orientations seen in XRD translated to increased in-plane polarization for BTO on Pt (d_{33} = 14.3 pm/V) and higher out-of plane polarization for BTO on LSCO (d_{33} = 54.0 pm/V). The values for effective d_{33} are smaller than the bulk value (d_{33} = 85 pm/V) due to substrate clamping, grain size, defects and orientation effects.

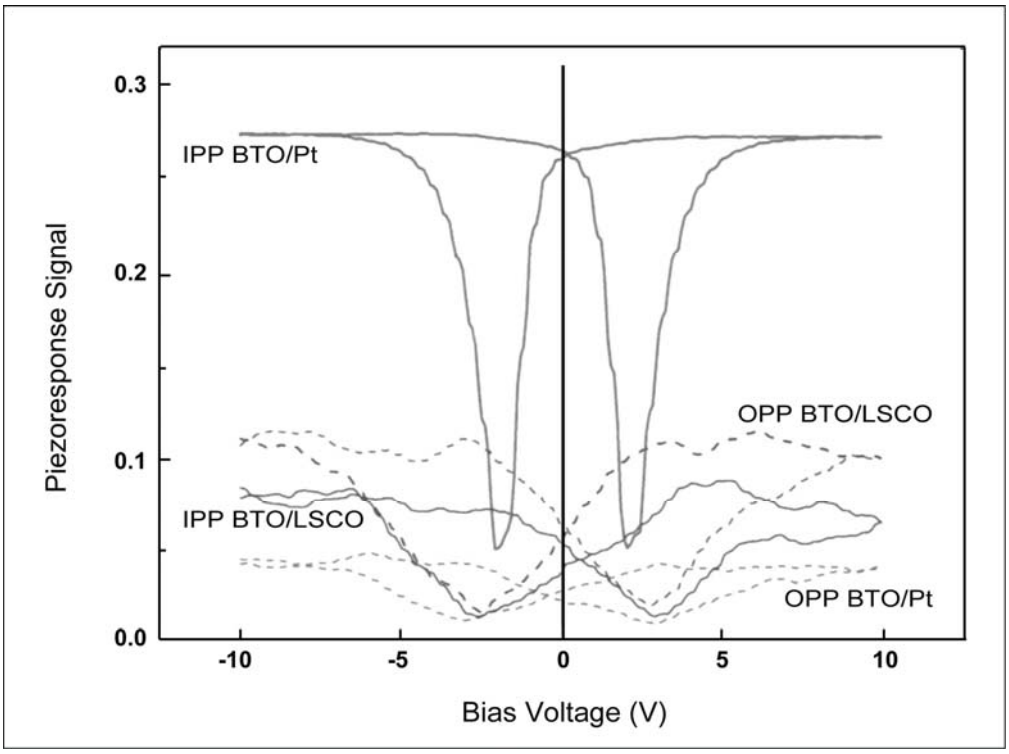

Figure 4.4. Barium titanate on conductive substrates–hysterisis. Local piezoresponse hysteresis loops for BTO films on Pt and LSCO substrates. Out-of-plane hysterisis loop for (A) BTO/Pt and (B) BTO/LSCO. In-plane hysterisis loops for (C) BTO/Pt and (D) BTO/LSCO.

4.1.2 Conclusion

The effects of crystal orientation on the piezoelectric properties of BTO thin films grown on Pt and LSCO/Pt electrodes have been investigated. Thin films deposited on Pt exhibit strong (101) orientation whereas films deposited on LSCO electrodes show mixed (001) and (101) orientations. The increase of the in-plane polarization signal in BTO thin films on Pt is related to the preferred (101) orientation of the polycrystalline films. The ferroelectric domains are thought to be clamped and stressed by the planar and biaxial stresses exerted by the substrate and lattice mismatch.

4.2 Mechanical Domain Switching

Nanoindentation, performed in conjunction with PFM, was used to study domain switching and to measure the mechanical properties of individual ferroelectric domains in tetragonal BTO. Nanoindentation induces local domain switching and allows the mechanical differences between a- and c-domains to be investigated. The elastic moduli of a- and c-domains were mapped to confirm their differences.

4.2.1 Nanoindentation

It is well known that the application of mechanical stress or electrical field can change the domain structure in ferroelectrics (*Fang et al. 2002, Holt et al. 2005, Li et al. 2005, Li et al. 1992, Park et al. 2004, Rogan et al. 2003*). As device size shrinks, ferroelectric components consist of only a few domains and the properties of individual domains play a critical role in design, fabrication and function of the entire device. The mechanical properties of individual a- and c-domains, such as Young's modulus, are not well characterized on the nanoscale. Characterization of ferroelectric domains at these small dimensions is challenging for existing mechanical testing techniques. AFM operated in piezoresponse mode, PFM, has been developed to image surface morphology as well as polarization domains. Recently, scanning nanoindentation has emerged as a technique for modulus mapping a surface (*Bhushan et al. 2003, Li et al. 2002, Li et al. 2003, Oliver et al. 1992*). Using PFM and scanning nanoindentation, the mechanical properties of individual a- and c-domains are reported for the first time.

This work focuses on (001) oriented, single crystal BTO. Individual domains are investigated using polarized optical microscopy and contact mode AFM. During AFM

surface imaging, domain information is collected *in situ* via piezoresponse signal with a lock-in amplifier. PFM imaging is preformed through n-doped silicon cantilevers, modulated with an AC voltage from 3 to 5 V at 1-2 kHz with a scan rate of 0.3 Hz. A nanoindenter monitored and recorded the load and displacement of a three-sided diamond pyramid indenter with a force resolution of 1 nN and a displacement resolution of 0.1 nm. A series of nanoindentations were made on individual a- and c-domains in BTO. A typical indentation experiment consisted of three steps: approaching the surface, loading to peak load (5 mN), and unloading. Elastic modulus and hardness were calculated from the load-displacement curves.

The surface morphology and domain structure of ferroelectric BTO is reported here. Figure 4.5A shows a schematic for the strip domain structure found in bulk tetragonal BTO. The lines represent typical piezoresponse signal intensity along alternating a- and c-domains during a PFM measurement and corresponding AFM scan (*Kalinin et al. 2002b*). The schematic represents domains with a downward polarization as "c+" domains because they will yield a positive deflection in the tip which is positively biased. In-plane domains show no signal during the out-of-plane PFM measurement. Figure 4.5B shows the polarized optical microscopy image of the BTO. The domain size is in the range of 2–10 microns. The c- and a-domains appear dark and light in the polarized image, respectively, due to the birefringence difference. Figure 4.5C shows the XRD and RHEED patterns indicative of BTO. The XRD shows (100)/(001) peak splitting due to the tetragonal structure.

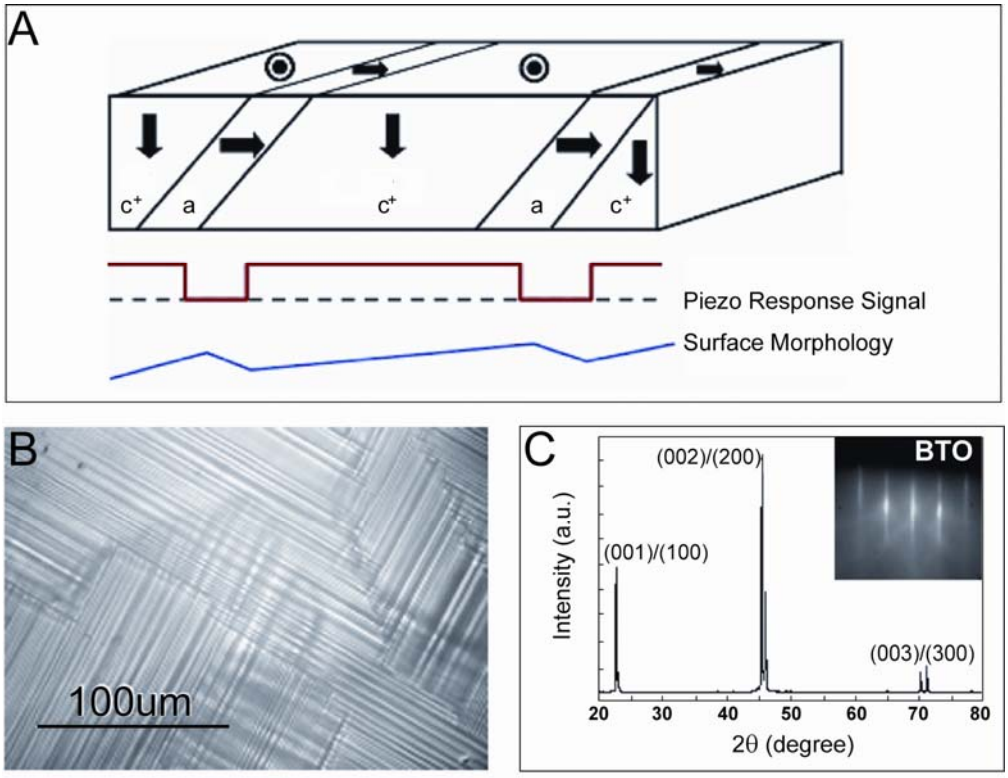

Figure 4.5. Bulk barium titanate domain analysis. Schematic and polarized optical microscopy image of ferroelectric domains in bulk BTO. (A) c- and a-domains and the associated PFM and AFM response expected. (B) Polarized optical microscopy image showing 90° stripe domains. (C) XRD and RHEED patterns showing single phase, bulk BTO.

The regions of interest for nanoindentation were found first using contact AFM (figure 4.6A). AFM shows the tetragonal corrugation due to a-/c- 90° domain walls. Domain sizes measured by AFM are in agreement with those seen in polarized optical microscopy. The angle formed at a- and c-boundaries is 0.5°–0.6° which confirms the tetragonal 90° domain walls. The piezoresponse image shows the downward pointing (c+) domains as bright areas and lateral in-plane domains as dark areas (figure 4.6B). The line profile in figure 4.6C shows the piezoresponse signal intensity along the a/c/a/c multidomains before nanoindentation. After confirming the domain characteristics using the AFM and PFM, nanoindentations were performed on individual a- and c- domains to study their mechanical properties and deformation behavior. After nanoindentation, AFM and PFM were performed in the same area to detect the indentation-induced domain switching. The piezoresponse signal (figure 4.6C) shows that c^+ domains switched by 180° to c-domains

and a-domains switched 90° to c-domains. Mechanical stresses due to nanoindentation therefore induced 180° and 90° domain switching.

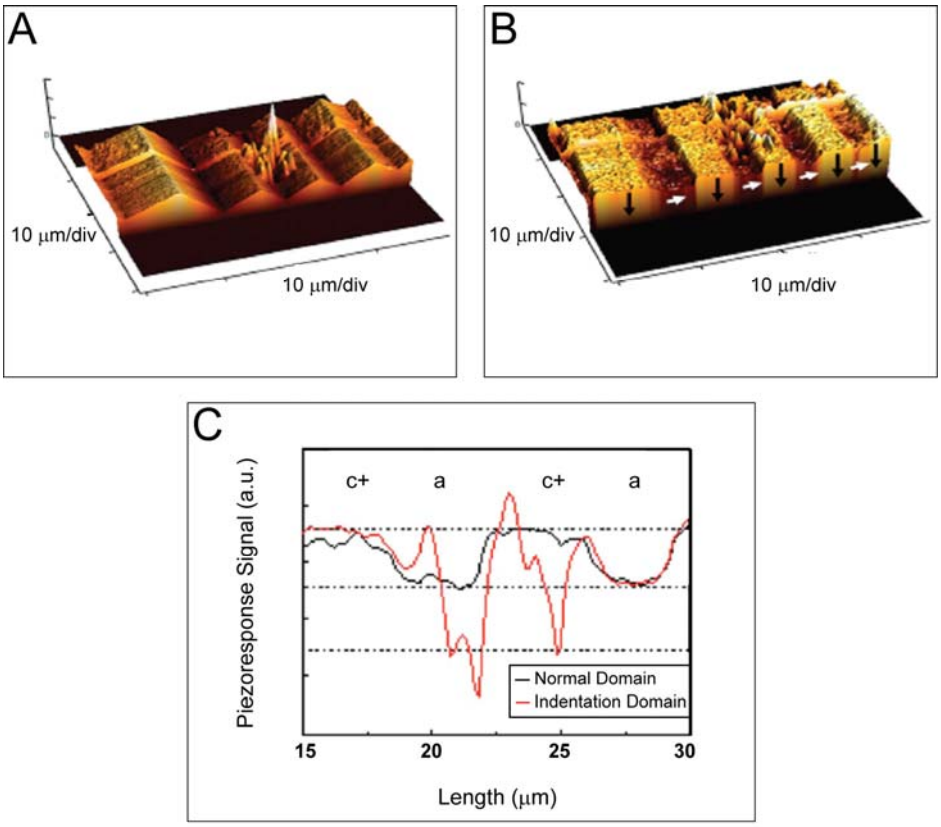

Figure 4.6. Bulk barium titanate AFM/PFM analysis. (A) AFM and (B) PFM scans of bulk BTO. (C) Piezoresponse line scan along surface before (black) and after (red) indentation.

Figure 4.7 shows the load-displacement curves of nanoindentations made on a- and c-domains together with the corresponding finite element simulation results. The a- and c-domains are thought to have widths on the order of 2–10 μm and form a mixed stacking multilayer 100–500 μm thick. The penetration depth of the nanoindenter is less than 150 nm in this study, which negates any effects from underlying domains (*Xu et al. 2004, Xu et al. 2006*). The load-displacement curves for a- and c-domains indicate that they have different mechanical properties. Under the same peak indentation load, displacement of the a-domain is less than the c-domain. Using a Poisson ration of 0.3, the elastic modulus of a-domains was calculated to be 154.16 +/- 1.92 GPa from these curves. The c-domains were found to have an elastic modulus of 139.59 +/- 2.55 GPa. The calculated hardness for a- and c-domains was comparable however, 13.94 +/- 0.26 GPa and 13.02 +/- 0.5 GPa, respectively.

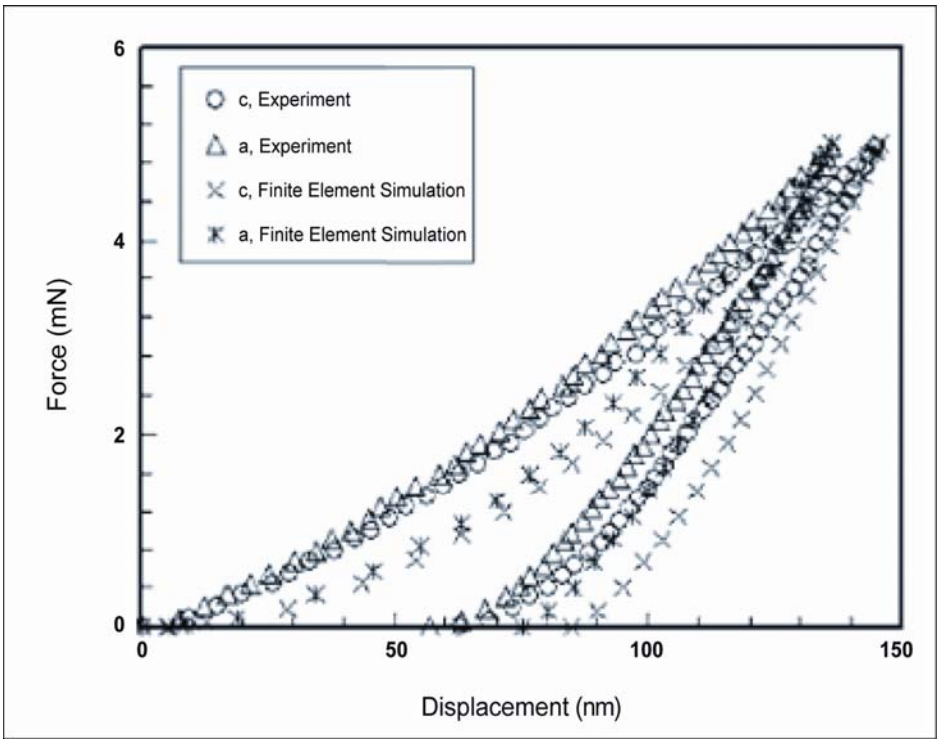

Figure 4.7. Bulk barium titanate nanoindentation. Force-displacement curves for nanoindentation on a- and c-domains in bulk BTO. Experimental (Ex) and finite element simulation (Fem) data are plotted.

The mechanical properties of individual a- and c-domains were measured by nanoindentation in conjunction with PFM. The a- and c-domains show comparable hardness but a significant difference in elastic modulus. It was found that nanoindentation can induce domain switching.

4.3 Conclusions

Mechanical activity in ferroelectric thin films was investigated thoroughly in the early stages of this work. We found that ferroelectric polarization domains could be imaged by PFM and their mechanical properties investigated by nanoindentation. The properties of a- and c-domains were investigated. The piezoelectric effect in BTO thin films was characterized by PFM. Orientation effects were investigated as films were deposited on Pt, and LSCO. Ferroelectric domain effects were investigated using nanoindentation on bulk BTO samples.

Chapter 5
Active Oxide Thin Films – Optical Studies

Engineering the optical properties of active oxide materials begins with deposition conditions. Complex oxide thin films are very sensitive to oxygen stoichiometry, and therefore, oxygen conditions during growth. In this chapter, we draw on work done to show the effect of oxygen conditions on the complex index of refraction of BTO thin films[†]. We present VASE as a characterization technique for the optical properties of active oxide thin films. A VASE model is developed to determine the index of refraction and absorption of thin films of BTO grown by MBE and PLD. Finally, two models are presented for VO_2 which describes the optical properties of the material in the semiconducting phase and the metallic phase.

5.1 Background

Integration of electrooptic materials with Si substrates allows for compact optical components capable of high frequency modulation, such as electrooptic modulators, to be developed using conventional CMOS processes. The ferroelectric perovskite BTO is an interesting candidate for thin film optical devices because of its large electrooptic coefficients and electrically switchable structural and optical properties. While growth of various oxide thin films has been demonstrated on Si, these films cannot support waveguiding modes due to low index contrast and the presence of cracks in thick films (*Lisoni et al. 2001, McKee et al. 1991*). Optical quality perovskite oxide thin films grown on sufficiently thick, low optical index template layers would allow for electrooptic thin film waveguides, modulators and statically tunable photonic devices to be designed and fabricated on Si and Si-compatible substrates. Previous attempts to grow thin BTO films on template layers has led to polycrystalline films on Si substrates (*Lisoni et al. 2001*) while oriented BTO films have been achieved via growth on MgO films deposited on Al_2O_3 (*Lipinsky et al. 2005*).

Ferroelectric thin films can be grown using PLD (*Beckers et al. 1998*), metal organic chemical vapor deposition (*Beckers et al. 1998, El-Naggar et al. 2005, Kwak et al. 1991*),

[†] Material used in this chapter is compiled from work done in *Dicken et al. 2007.*

sol-gel synthesis (*Wills et al. 1992*) and MBE (*Lemoine et al. 1994, McKee et al. 1991*). MBE can be used to grow complex oxide thin film structures with atomic layer accuracy (*Schlom et al. 2001*). High quality ferroelectric thin films are generally grown on lattice matched substrates such as MgO and STO. Integration of ferroelectric thin films with Si processing may enable the properties of ferroelectrics to be utilized in combination with CMOS in multi-material integration. IBAD of various template layers such as MgO and yttria-stabilized zirconia has been used to develop thin films of superconducting $YBa_2Cu_3O_7$ as well as oriented layers of $(Pb,Ba)TiO_3$ (*Brewer & Atwater 2002, Wang et al. 1997*).

We have developed processes for growth by IBAD of biaxially oriented MgO films that act as templates for growth of highly textured ferroelectric perovskite oxide films (*Brewer & Atwater 2002*). So far, however, well oriented, optical-quality BTO films integrated with amorphous substrates in conjunction with Si-based substrates have not been realized. In this chapter we investigate growth of highly textured BTO films on various substrates using different oxidation sources and establish models to fit the optical properties of BTO thin films in order to compare with single crystal BTO.

5.2 Optical Properties of Textured Barium Titanate Thin Films

We have investigated the growth of BTO thin films on bulk crystalline and amorphous substrates utilizing biaxially oriented template layers. IBAD was used to grow thin, biaxially textured, MgO template layers on amorphous and Si substrates. Growth of highly oriented BTO films on these template layers was achieved by MBE using a layer-by-layer growth process. BTO thin films were grown in molecular oxygen and in the presence of oxygen radicals produced by a RF plasma. We used x-ray and *in situ* RHEED to analyze the structural properties and show the predominately *c*-oriented grains in the films. VASE was used to analyze and compare the optical properties of the thin films grown with and without oxygen plasma. We have shown that optical quality BTO thin films, which show bulk crystal-like properties, can be grown on any substrate through the use of biaxially oriented MgO template layers.

5.2.1 Barium Titanate Thin Film Growth

We have grown BTO via MBE on bulk MgO substrates as well as biaxially-textured MgO film templates on SiO_2 on Si and Si_3N_4 on Si using both oxygen gas and an oxygen plasma as the oxidizing agent. IBAD of MgO can be used to form biaxially textured crystalline template layers (*Wang et al. 1997*). Thin perovskite films grown on IBAD MgO template layers have been shown to grow with the biaxial texture inherited from the template (*Brewer & Atwater 2002*).

Biaxially textured MgO thin films were achieved using an e-beam evaporator to heat MgO crystals to a deposition rate of 0.2 nm/s. A 1200eV Ar^+ ion beam, impinging on the substrate at 45^o incidence, is used to develop the biaxial-texture of the film. MgO is evaporated under Ar^+ ion bombardment at these conditions to a total thickness of approximately 15 nm as measured by a quartz crystal monitor. The crystal texture development is monitored using RHEED. The IBAD MgO film is then heated to 650 ^oC and an additional 35 nm of homoepitaxial MgO is evaporated on top of the biaxially oriented layer leading to larger MgO grain size and sharper in-plane and out-of-plane crystal orientation. Finally, the IBAD template layer is annealed at 700 ^oC for 1 hour in 6.5 X 10^{-6} mTorr oxygen.

BTO thin films were grown by MBE using a layer-by-layer growth technique. This technique is calibrated such that each shutter sequence exposes the substrate to one monolayer of BaO followed by one monolayer of TiO_2 to ultimately construct the BTO unit cell. Monolayer deposition was calibrated using RHEED intensity oscillations for both constituents. Separate experiments were done depositing BaO and TiO_2 on bulk MgO substrates to calibrate the deposition rates. RHEED intensity oscillation data was used to find optimum source temperatures and shutter times to expose the substrate to one monolayer of material. The Ba material source is a resistively heated cell that was held at 625 ^oC. The Ti source is a Ti-Ball sublimation pump operating at 700 Watts. The MgO substrate is brought to 650 ^oC using a SiC heater. Using these temperatures we found that one monolayer of both BaO and TiO_2 were deposited over 10 seconds. BTO growth was performed at 1 X 10^{-6} mTorr oxygen with and without a RF plasma source. When utilized, the plasma source generates an oxygen plasma using 300 Watts forward power and 0-1 Watts reflected power.

5.2.2 Characterization

In situ RHEED was used to monitor IBAD MgO and BTO thin film texture development (*Brewer & Atwater 2002*). RHEED images taken with a CCD camera are used to qualitatively monitor film growth. RHEED intensity oscillations are also monitored to confirm layer-by-layer growth. RHEED images of bulk MgO (figure 5.1A) compare well to those of IBAD MgO. Figure 5.1B exhibits a typical RHEED pattern for a biaxially textured IBAD MgO template layer after deposition on amorphous Si_3N_4 on Si. Streaks in the IBAD MgO RHEED pattern attest to the smoothness of the template layer, while the angular orientation of the RHEED spots show how the grains are oriented out of plane with some small distribution about the normal. In-plane RHEED rocking curves have been used to confirm the in-plane crystal orientation distribution is approximately 4° (*Wang et al. 1997*). Figures 5.1E,F show BTO films grown on IBAD MgO templates and bulk MgO in a 1 X 10^{-6} mTorr molecular oxygen ambient. The larger RHEED spots exhibited by the BTO/IBAD-MgO/Si_3N_4/Si sample are due to the inheritance of the biaxial-texture distribution from the template layer. The BTO/bulk MgO sample shows epitaxial orientation. AFM scans of these films confirm grain sizes on the order of 200 nm and RMS roughness of 2 Å for individual grains and 2 nm for a 60 μm by 60 μm scan. Figures 5.1C,D compare BTO films grown on similar IBAD and bulk MgO substrates using 1 X 10^{-6} mTorr oxygen in a 300 Watt RF plasma. Samples grown using an oxygen plasma exhibit more defined diffraction spots indicating these films are of better crystal quality.

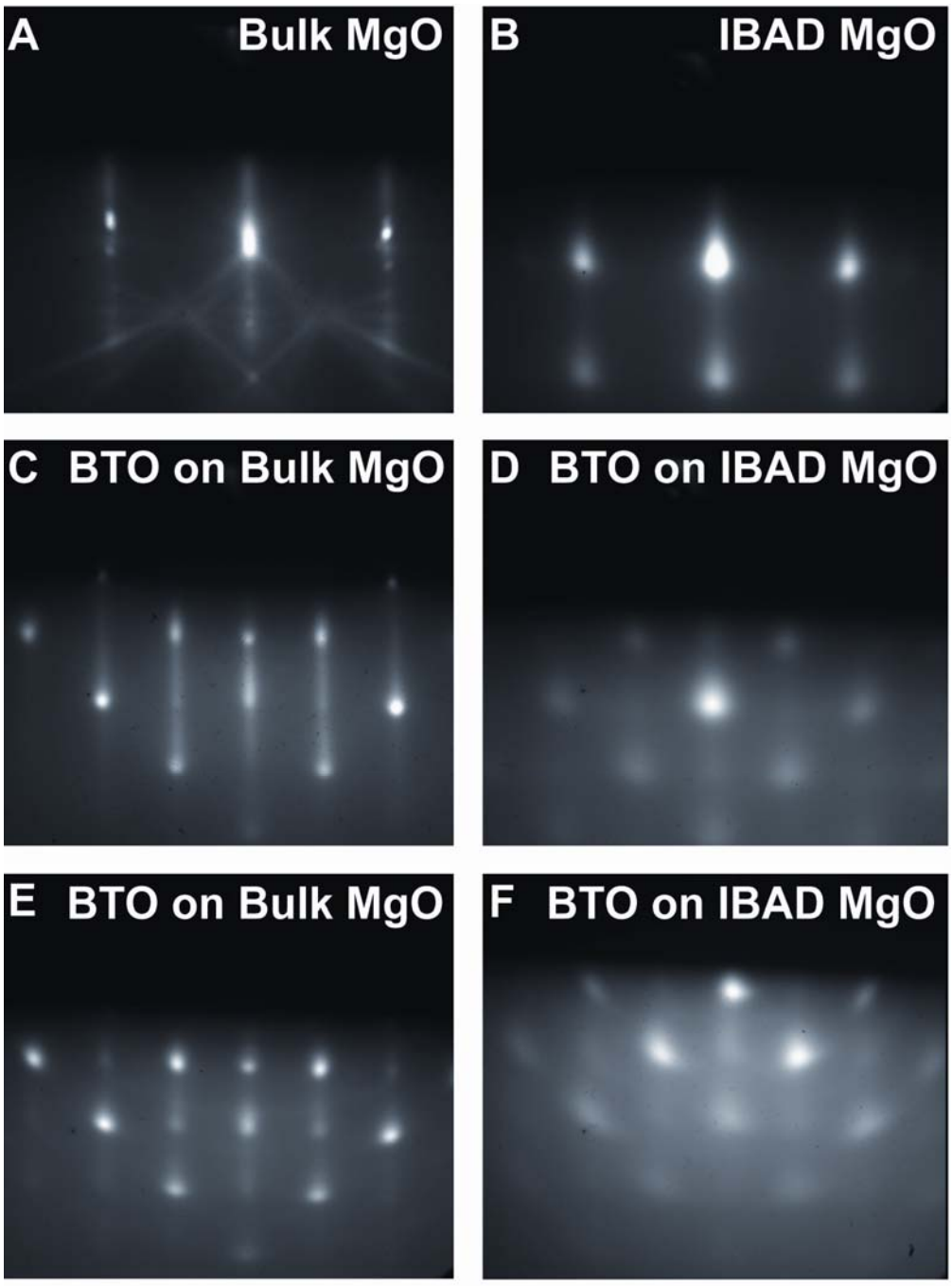

Figure 5.1. Barium titanate RHEED comparison: plasma growth vs molecular O_2. RHEED images along the (00l) zone axis of (A) bulk MgO, (B) IBAD MgO deposited on amorphous Si_3N_4, (C) BTO on bulk MgO using an O_2 plasma, (D) BTO on an IBAD MgO using an O_2 plasma, (E) BTO grown on bulk MgO using O_2, (F) BTO grown by MBE on an IBAD MgO template layer deposited on Si_3N_4 using O_2.

We used XRD to analyze the crystal orientation of the thin films. θ–2θ XRD scans of the films were used to determine relative crystallinity and texture of the sample. We found that samples grown by MBE at these conditions produced diffraction spectra with the c/a peaks shifted toward the c-axis value. Figure 5.2 shows θ–2θ X-ray diffraction measurements done on thin film BTO samples to investigate the crystal orientation. XRD scans of BTO/MgO samples reveal the predominately c-orientation of the thin films as expected from deposition on bulk MgO (*Beckers et al. 1998*).

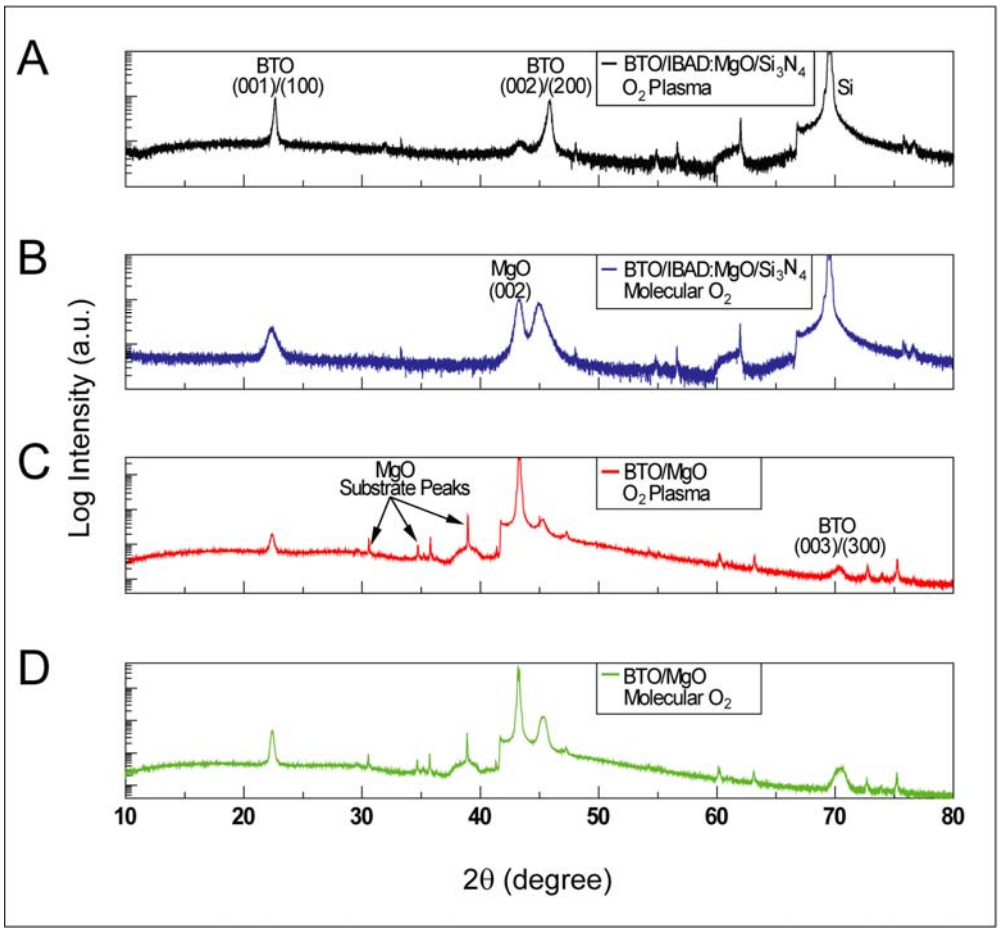

Figure 5.2. Barium titanate x-ray diffraction comparison: plasma growth vs molecular O_2. X-ray diffraction θ–2θ scans of (A) MBE BTO on IBAD MgO using O_2 plasma, (B) MBE BTO on IBAD MgO using molecular O_2. (C) MBE BTO on bulk MgO using O_2 plasma, (D) MBE BTO on bulk MgO using molecular O_2.

The broadness of the diffraction peaks for samples grown on IBAD MgO templates may indicate "a-" and "c-axis" oriented grains. All of the BTO thin films show predominately (00*l*) orientation as compared with single crystal BTO data.

The same growth process was performed on an n^+ doped, conductive, Si substrate. This sample was used for PFM. The detailed measurement conditions of PFM are shown in (*Kim et al. 2005*). Figure 5.3 shows AFM and PFM images of a BTO film grown on an IBAD MgO template deposited on an n^+ doped conductive Si substrate. PFM uses a biased conducting AFM tip to sense domain polarization and electromechanical displacement in ferroelectric films. Figure 5.3A shows an AFM image of the surface of the BTO sample. The BTO thin film morphology is characterized by large grains with extremely low RMS roughness, 0.2 nm, on the order of atomic step height. The surface corrugation angle, θ, of tetragonal BTO is typically 0.4°-0.6° below Curie temperature ($T_c \approx 125$ °C for bulk BTO) which can be obtained by

$$d\theta = 2\arctan\left(\frac{c}{a}\right) - 90° \quad , \tag{5.1}$$

where **a** and **c** are lattice parameters (c/a ratio = 1.016 for BTO). The AFM line scan and surface angle in figure 5.3A shows a typical surface corrugation angle, which means the film has a tetragonal structure due to a strain between c/a domains during the growth and cooling processes during which the films experience a ferroelectric phase transition from cubic to tetragonal. This is consistent with the XRD result shown in figure 5.2. We used OPP and IPP PFM measurements to image the ferroelectric polarization domains. Effective d_{33} value of BTO film can be estimated using this method.

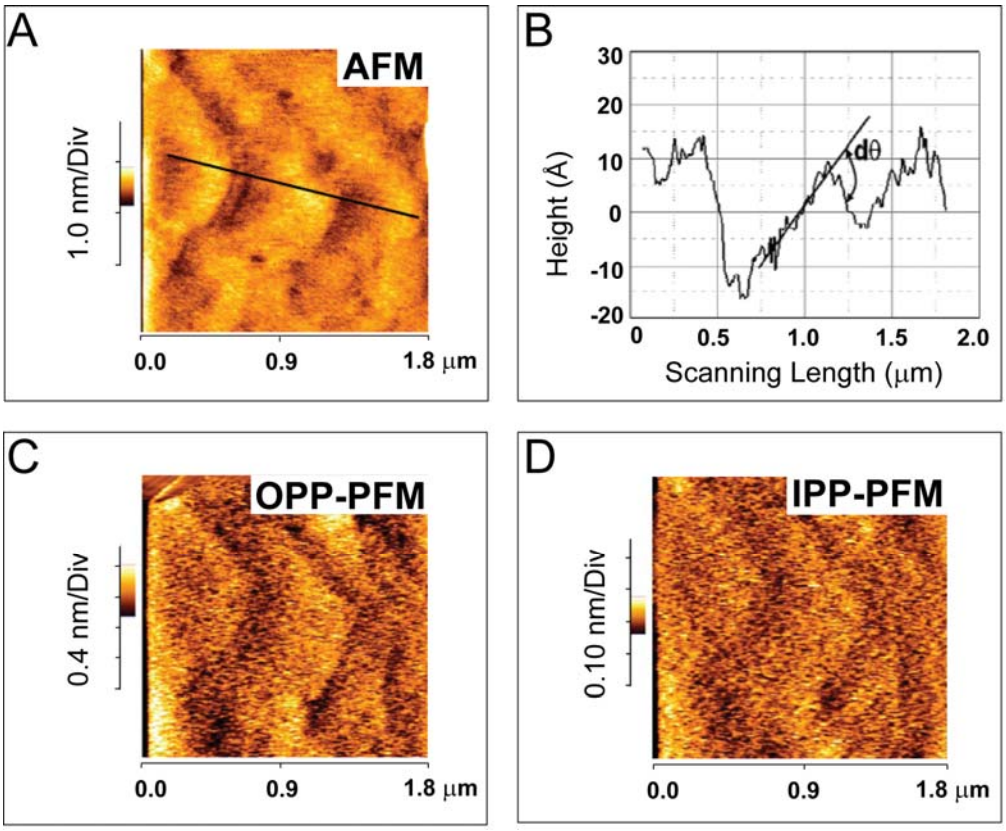

Figure 5.3. Barium titanate AFM/PFM: plasma growth. (A) AFM image of BTO grown by MBE on an IBAD MgO template layer deposited on an n+ doped Si substrate, (B) AFM line scanning along domains, (C) OPP-PFM image and (D) IPP-PFM image. Scanning size of all images is 1.8 μm x1.8 μm

Optical thin film characterization was performed using VASE in the wavelength range 300-2200 nm to obtain the complex dielectric function of our thin BTO films. Psi and Delta measurements were taken at 63°, 65°, and 67° and the data were fit using both the Tauc-Lorentz model and a relaxed Lorentzian model for the dielectric function. The fitting program minimizes the mean-square error by varying the function parameters. Model fits for Ψ and Δ were performed on the three different angle data sets simultaneously. The experimental data from VASE characterization is shown in figures 5.4 through 5.7. VASE gives Ψ and Δ values for the BTO films in UV-visible-infrared range. Multiple angles (63^o, 65^o, and 67^o) are used to scan above and below the Brewster angle, $\theta_b = \arctan(n_1/n_2)$, of the BTO thin films. This is the first example of the VASE data of BTO thin films in the range 300-2200 nm.

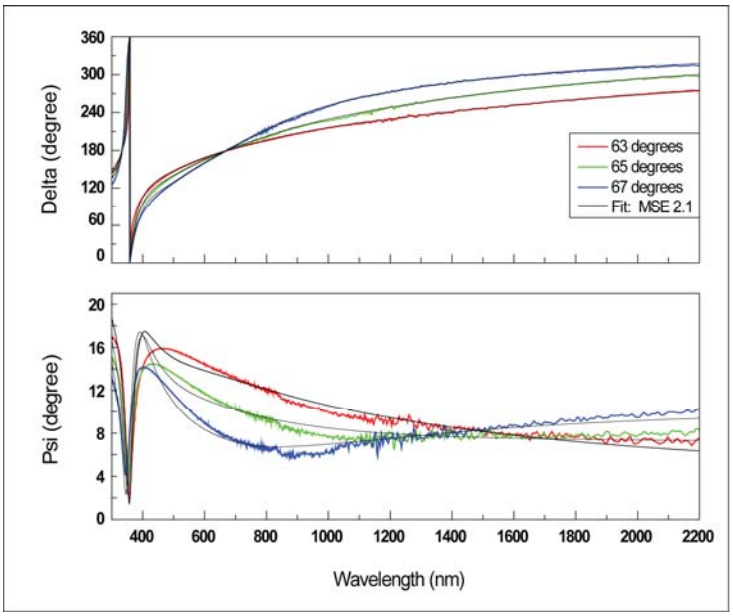

Figure 5.4. Barium titanate/MgO VASE: plasma growth. VASE data and fits using the Tauc-Lorentz model. The BTO thin film is 75 nm thick, grown on bulk MgO using a 300 Watt RF oxygen plasma.

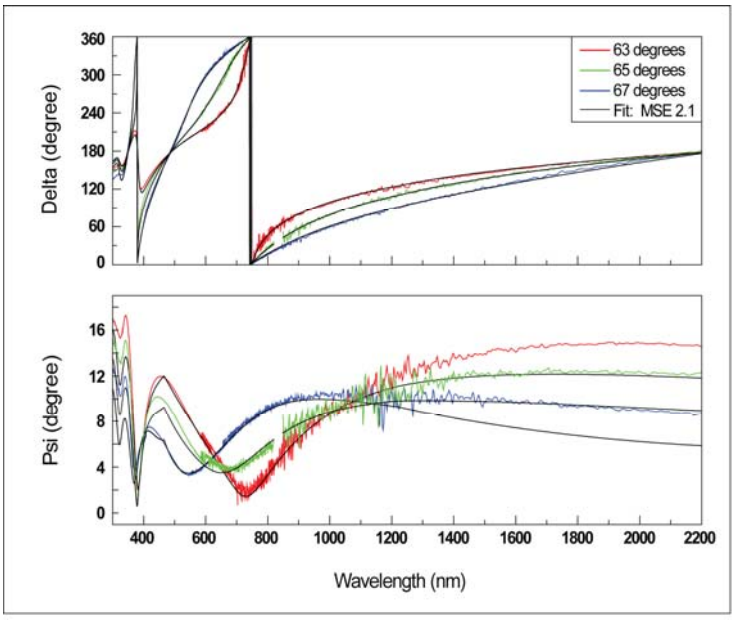

Figure 5.5. Barium titante/MgO VASE: molecular O_2 growth. VASE data and fits using the relaxed Lorentzian model. The BTO thin film is 175 nm thick, grown on bulk MgO using molecular oxygen.

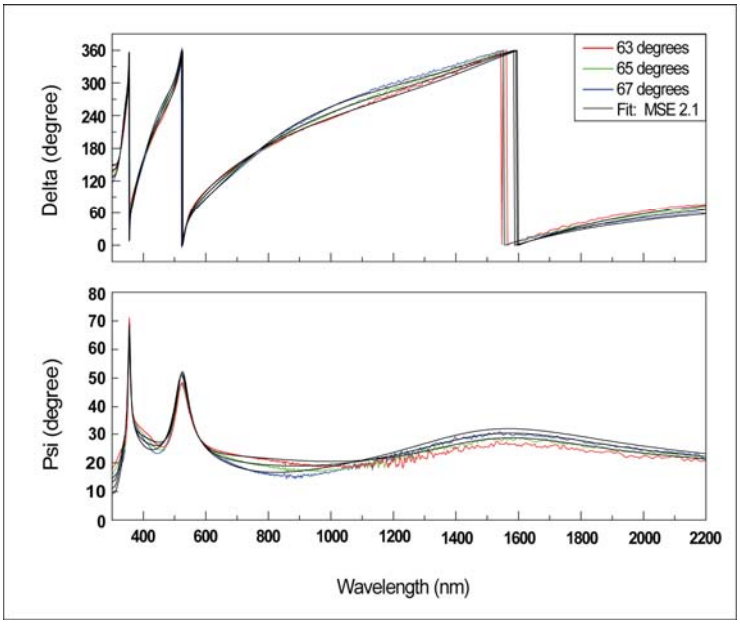

Figure 5.6. Barium titanate/IBAD MgO VASE: plasma growth. VASE data and fits using the Tauc-Lorentz model. The BTO thin film is 150 nm thick, grown on 30 nm IBAD MgO using a 300 Watt RF oxygen plasma.

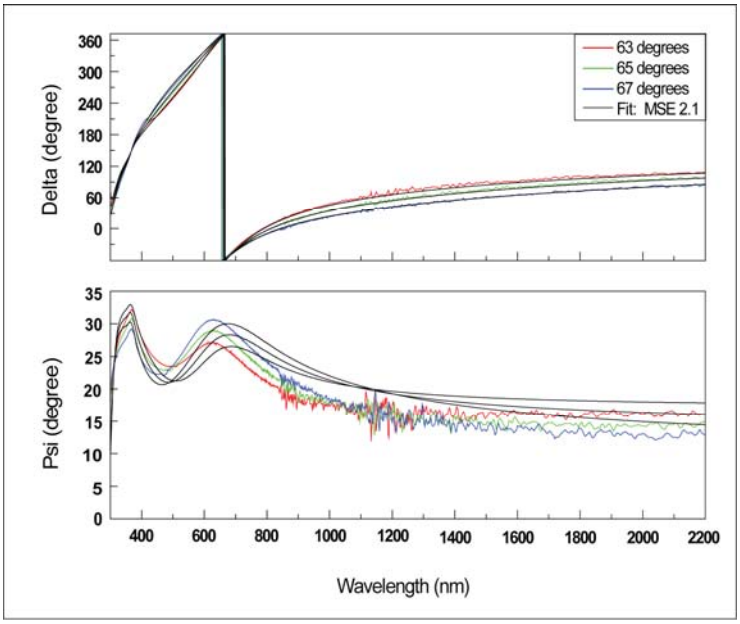

Figure 5.7. Barium titanate/IBAD MgO VASE: molecular O_2 growth. VASE data and fits using the relaxed Lorentzian model. The BTO thin film is 20 nm thick, grown on 30 nm IBAD MgO using molecular oxygen.

We analyze these experimental data (figures 5.4-5.7) using a relaxed Lorentzian or Tauc-Lorentz (equation (5.2)) type dispersion relationships to fit Ψ and Δ data.

$$\varepsilon_1(E) = \varepsilon_1(\infty) + \frac{2}{\pi} P \int_{E_g}^{\infty} \frac{\xi \varepsilon_2(\xi)}{\xi^2 - E^2} d\xi$$

$$\varepsilon_2(E) = \frac{A \cdot E_0 \cdot C \cdot (E - E_g)^2}{(E^2 - E_g)^2 + C^2 \cdot E^2} \cdot \frac{1}{E} \qquad E > E_g \tag{5.2}$$

$$\varepsilon_2(E) = 0 \qquad E \le E_g$$

The fit was done by minimizing the mean-square error (MSE) for all three data sets simultaneously (equation (5.3)).

$$MSE = \frac{1}{2J - K} \sum_{i=1}^{J} [(\tan(\Psi_i^{\text{mod}}) - \tan(\Psi_i^{\text{exp}}))^2 + (\cos(\Delta_i^{\text{exp}}) - \cos(\Delta_i^{\text{mod}}) - \cos(\Delta_i^{\text{exp}}))^2] \tag{5.3}$$

Samples grown using molecular oxygen exhibited optical absorption throughout the range of 300-2200 nm and were fit using a relaxed Lorentzian for the dielectric function. This function allowed for the index of refraction to be modeled in the entire range. Samples grown in oxygen plasma showed no visible absorption and were fit using a Tauc-Lorentz model. This model is Kramers-Kronig consistent and gives information about band gap and static dielectric constant. After these data were modeled, the index of refraction and absorption coefficients were simulated using the models. Comparisons of n(ω) and k(ω) for films grown on IBAD MgO and bulk MgO with and without oxygen plasma are shown in figure 5.5. It can be seen that films grown using molecular oxygen as the oxidation agent led to films with high absorption. We believe this is due to a large number of oxygen vacancies in these films.

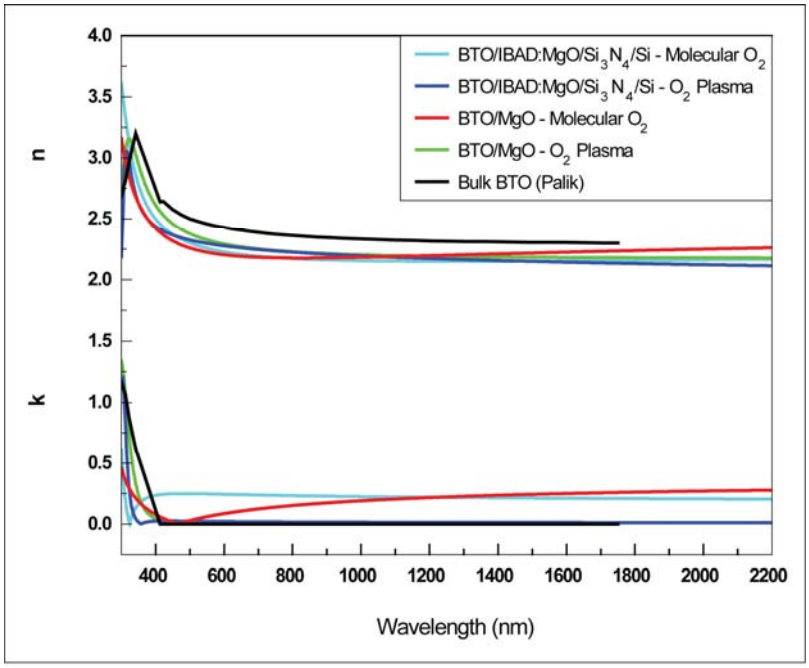

Figure 5.8. Barium titanate index of refraction comparison. Index of refraction (n) and absorption (k) derived from relaxed Lorentzian fits to ellipsometric data.

The wavelength dependence of the refractive index and absorption coefficient for BTO thin films was obtained by simulating the values of Psi and Delta from the best fit using Tauc-Lorentz and/or Lorentzian-models (MSE ≈ 2.0). The optical constants dispersion relations for BTO grown with and without oxygen plasma are represented in figure 5.8. Refractive index and absorption coefficients for single crystal BTO from handbook values are shown for comparison.

We find that thin BTO films grown with oxygen plasma have bulk-like indices of refraction. As expected, higher atomic oxygen partial pressure reduces oxygen vacancy sites to compensate the stoichiometric ratio during the layer-by-layer growth. Each Ba and Ti monolayer should be fully oxidized by using oxygen plasma; however, excess amounts of atomic oxygen can etch the growing surface at high plasma power. Films grown using oxygen plasma also exhibit higher resistivity compared to molecular oxygen-BTO thin films.

To compare the optical properties of MBE and PLD oxide thin films we performed VASE on PLD BTO (figure 5.9). The PLD BTO film thickness was 400 nm grown on bulk MgO. We see that PLD films have the same low absorption as films grown by MBE with a 300 Watt oxygen plasma.

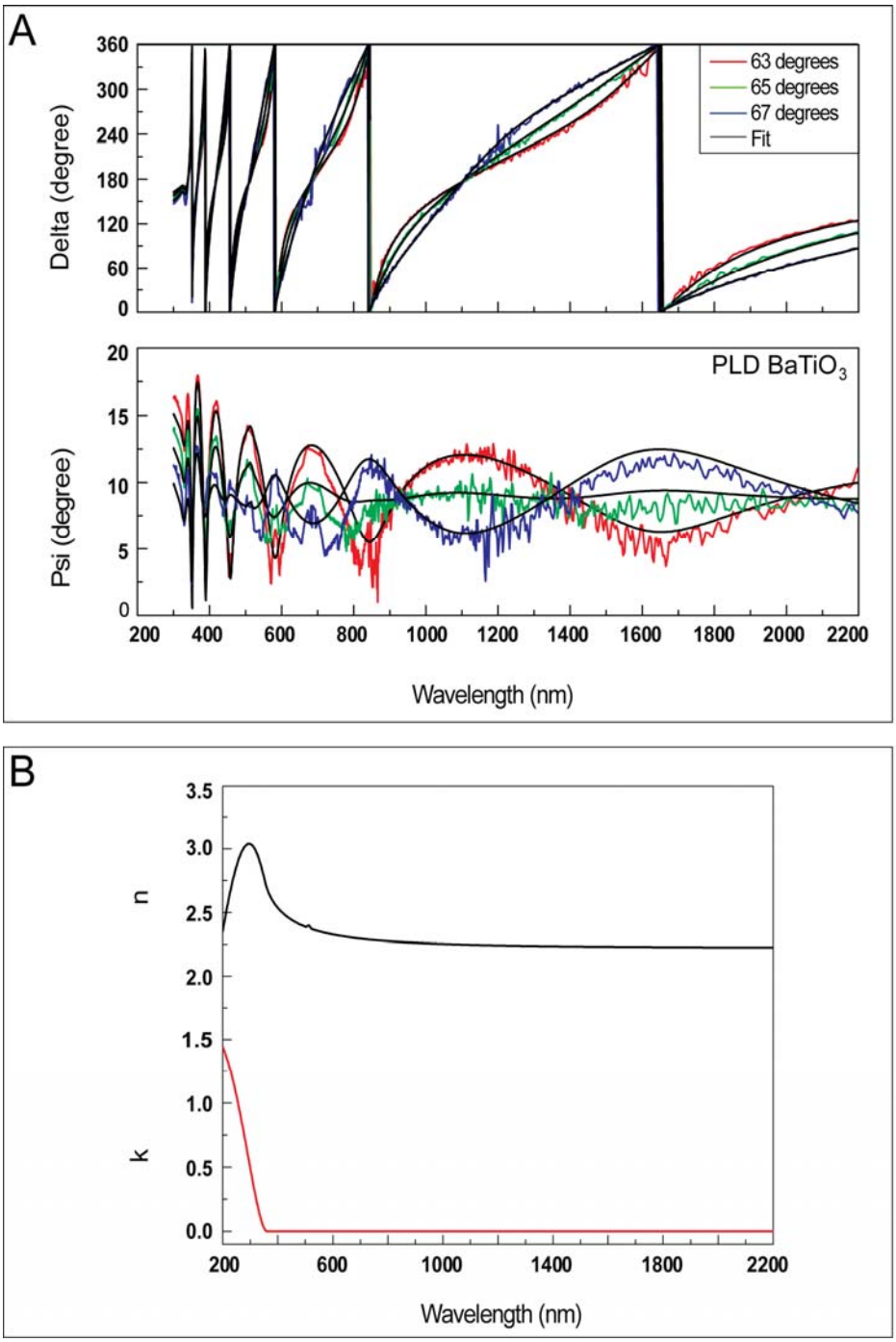

Figure 5.9. VASE of pulsed laser deposition barium titanate. The optical quality of PLD BTO is comparable to MBE films grown in an oxygen plasma. Data were fit using a Tauc-Lorentz function similar to MBE films (equation (5.1)).

5.2.3 Conclusion

In summary, highly textured and optically active BTO thin films were grown by layer-by-layer MBE on various crystal substrates by using IBAD MgO template which allows the growth of BTO films on amorphous and Si-based substrates. X-ray diffraction and *in situ* RHEED analyses show the highly textured *c*-orientation of the BTO films on both IBAD MgO/a-Si_3N_4/Si and bulk MgO substrates independent of oxidation methods. Optical properties of the BTO films show bulk-like dispersion relations, but films grown using molecular oxygen exhibit large optical absorption throughout the wavelength range 300—2200 nm. Utilizing an oxygen plasma ambient during growth helps to develop optically transparent and stoichiometric BTO film growth on any substrate. In addition, PLD BTO films are of comparable optical quality to MBE films.

5.3 Optical Properties of Vanadium Oxide Thin Films

Vanadium (II) oxide (VO_2) is a transparent semiconductor at room temperature. Above 70° C, VO_2 undergoes a metal-insulator transition (MIT) which is accompanied by a large change in the material optical properties. We use VASE to measure the optical properties of both phases of VO_2 and develop a separate optical model for each phase to extract the complex index of refraction. VASE data for VO_2 at room temperature, during heating with a conventional heat gun, and above its MIT temperature are shown in figure 5.10. The complex index of refraction for VO_2 was modeled at room temperature and above the metal transition temperature. At room temperature, VO_2 can be modeled as a Tauc-Lorentz layer, similar to BTO, above its MIT it is modeled as a Drude metal. The Ψ and Δ data were fit using these models and n and k (ε_1 and ε_2) as a function of wavelength were extracted (figure 5.11). The complex index of refraction for each VO_2 sample can be found using this procedure. These data are used to model the VO_2 layer in the metamaterial structures discussed in chapter 7.

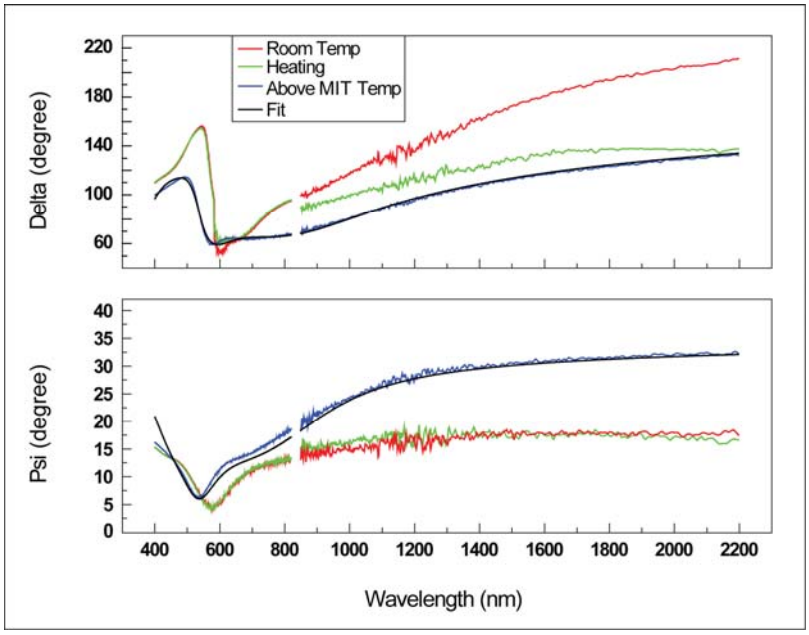

Figure 5.10. VO_2 VASE: heating experiment. VASE data and optical model fits of PLD VO_2 on c-plane Al_2O_3 above and below the metal-insulator transition. A conventional heat gun was used to induce the MIT during data collection.

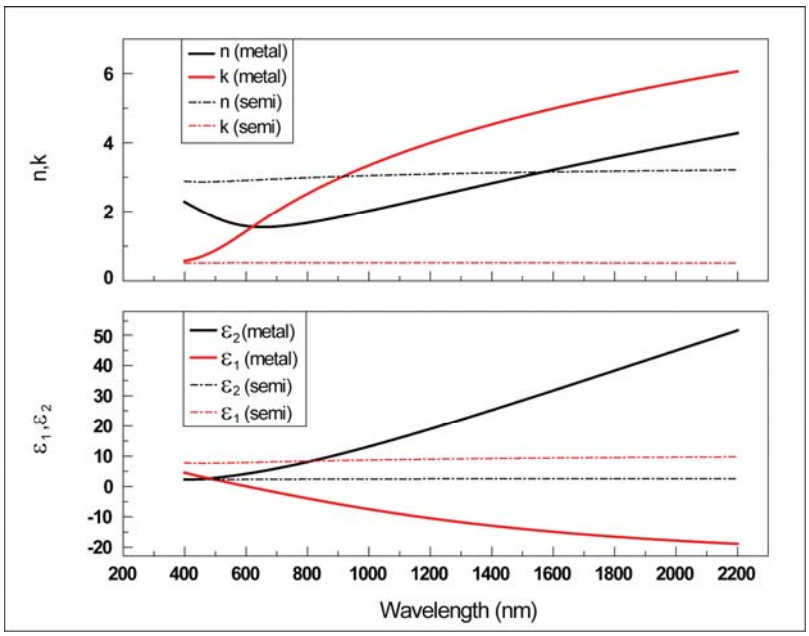

Figure 5.11. VO_2 complex index of refraction. Complex refractive index (dielectric constants) as a function of wavelength for PLD VO_2 on c-plane Al_2O_3. Data were modeled using Tauc-Lorentz (semiconductor phase) and Drude oscillator (metallic phase) models.

Part III

Active Metal-Oxide Nanophotonics

Chapter 6
Active Metal-Oxide Plasmonics

In this chapter we discuss the first example of an active optical device based on BTO thin films conceived of, simulated, fabricated, and tested in our lab[†]. We demonstrate control of the SPP wavevector in an active metal-dielectric plasmonic interferometer by utilizing electrooptic BTO as the dielectric layer. Arrays of sub-wavelength interferometers were fabricated from pairs of parallel slits milled in Ag on BTO thin films. Plasmon-mediated transmission of incident light through the sub-wavelength slits is modulated by an external voltage applied across the BTO thin film. Transmitted light modulation is ascribed to two effects, electrically induced domain switching and electrooptic modulation of the BTO index.

6.1 Introduction

The optical transmittance of arrays of sub-wavelength surface apertures in metal films, such as holes and slits, has generated enormous scientific interest and surface plasmons have been found to play a governing role (*Ebbesen et al. 1998, Garcia-Vidal et al. 2003, Gay et al. 2006, Lezec & Thio 2004, Thio et al. 2001*). Surface apertures have been studied extensively as a means for coupling electromagnetic waves into and out of SPP modes. Recently, passive plasmonic interferometers were constructed from pairs of slits as a means to enhance understanding of slit array transmittance (*Schouten et al. 2005*). Although at present these devices are only prototypical, ultra-compact modulators derived from subwavelength slit arrays could have active areas less than 10 μm^2, compared to 1000 μm^2 for conventional electrooptic modulators.

Surface plasmon polaritons are highly confined electromagnetic waves that propagate along a metal-dielectric interface by coupling to a polarization of the electron gas in the metal. Light can be coupled into and out of these modes by scattering from abrupt structural features such as grooves or slits (*Lalanne et al. 2005*). The ground work for passive plasmonic structures has been laid through intensive studies of SPP propagation in metal-dielectric structures (*Dionne et al. 2006*). It has been shown that these waves can interact

[†] Material used in this chapter is compiled from work published in reference *Dicken 2008*.

with light transmitted through slits to create an interference pattern in the overall transmission intensity and this interference pattern can be affected by changes to the imaginary part of the SPP wavevector (*Pacifici et al. 2007*). SPP modulation via the electrooptic effect has been studied previously in polymer films by coupling light into surface plasmon modes at a metal-polymer interface (*Chyou et al. 2005*). Here, we investigate dynamic modulation of the real part of the SPP wavevector by replacing the dielectric layer in the structure with an electrooptically active BTO thin solid film.

Barium titanate is a well known perovskite ferroelectric material that exhibits a large electrooptic coefficient, on the order of r = 100 pm/V, and large birefringence due to its atomic structure, $\Delta n = 0.05$ (*Beckers et al. 1998, Zgonik et al. 1994*). Thin films of BTO are deposited by numerous techniques and their optical properties have been widely investigated and employed in electrooptic waveguides and modulators (*Petraru et al. 2002, Tang et al. 2004a, Tang et al. 2004b*). BTO has a tetragonal crystal structure with an ordinary index, $n_o = 2.412$, corresponding to the shorter a-axis, which is larger than the extraordinary index, $n_e = 2.36$, along the longer c-axis. Ferroelectric domains form when the film is cooled below the Curie temperature of 120 ^oC and their final orientation is affected by film stresses, as well as lattice and thermal expansion mismatch. Ferroelectric domains in BTO can be characterized by their orientation in-plane (a-axis) or out-of-plane (c-axis). BTO thin films deposited on oxide thin film electrodes have been characterized by PFM and show both in-plane and out-of-plane domains (*Kim et al. 2005*). These domains can be manipulated by applying an electric field across the material, and in-plane domains can be forced to switch out-of-plane under an applied field greater than the coercive field. This domain switching event is accompanied by a large change in the index of the BTO thin film due to the birefringence in the material. Using BTO thin films, we modulate the real part of the index of refraction at the Ag/$BaTiO_3$ interface and thereby modulate the SPP wavevector.

6.2 Device Design

6.2.1 Plasmonic Interferometer Device Stack

A schematic of the plasmonic interferometer based on double-slit transmission and electrooptic modulation of the SPP wavevector is shown in figure 6.1.

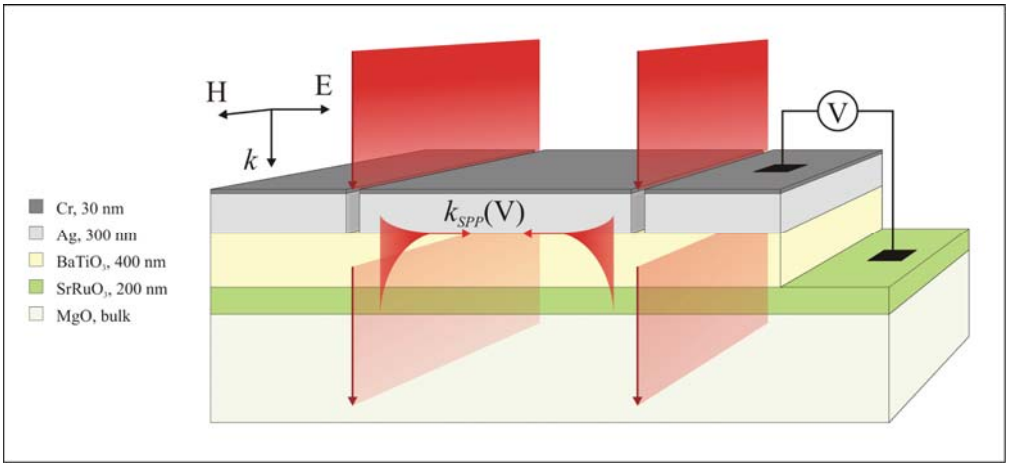

Figure 6.1. Double-slit metal-ferroelectric plasmonic modulator. Schematic of a plasmonic modulator based on interference of surface plasmon polaritons (SPP) launched from a set of parallel slits milled into a planar metal film. The counter-propagating SPPs travel with wavevector k_{SPP} along the Ag/BTO interface. The interference of these SPPs with the transmitted fields can be affected by an applied voltage across the BTO layer, by means of electrooptic modulation and electrically induced domain switching.

The optically active oxide thin film stack used for these SPP mediated double-slit interferometers was deposited without breaking vacuum in a PLD system (Neocera 180). SRO and BTO thin films were deposited on double-side polished MgO substrates (MTI Crystal). MgO substrates with dimensions 10 X 10 X 0.5 mm were attached to a molybdenum holder with silver paste for good thermal contact. Substrates were annealed at 900 ^{o}C for 1 hr in vacuum (P = 1 X 10^{-7} Torr) prior to growth. The SRO and BTO films were deposited at 700 ^{o}C with background oxygen partial pressures P_{O2} = 150 mTorr and P_{O2} = 10 mTorr respectively. The substrates were rotated 60°/sec and the target-substrate distance kept at 9 cm during growth. A KrF excimer laser (λ = 248 nm) focused onto sintered targets of 99.9% pure $SrRuO_3$ and 99.99% pure $BaTiO_3$ was used to ablate the material at a pulse rate of 10 Hz with a pulse power of 300 mJ. After deposition, the films

were cooled to room temperature at a rate of 5°/min at P_{O2} = 1 Torr. The film thicknesses grown under these conditions were 400 nm BTO and 200 nm SRO. The crystal structure of the samples was characterized by XRD and RHEED. θ-2θ XRD scans were performed in a Panalytical X'PERT diffractometer using Cu Kα radiation (λ = 1.5406 Å). θ-2θ XRD scans show the epitaxial, single-crystalline phase (100/001), of the BTO/SRO/MgO structure. RHEED was performed *ex situ* in a separate chamber equipped with a 25 keV electron gun. Ag (300 nm) and Cr (30 nm) films were vacuum deposited by evaporation onto the sample through a shadow mask to expose only a rectangular area on the sample. The structures consist of pairs of parallel slits etched into the metal layer by FIB milling (FEI Nova 600 Dual Beam Focused Ion Beam system, Ga^+ ions, 30 keV). The slits are 5 μm long by 100 nm wide with slit pitch starting at 500 nm and increasing by 20 nm for each device along a row. Each device is laterally separated by 5 μm (figure 6.2). Electrical contacts are made to the SRO film by mechanically etching the BTO film and contacting the SRO using conventional silver paste. The final device is mounted onto a glass slide and copper tape is used to contact the top Cr/Ag layer and bottom SRO layer. A total of 240 plasmonic interferometers were investigated using these methods.

6.2.2 Analytical Model

The device array is illuminated by a TM-polarized (H-field parallel to the long axis of the slit) light source causing a fraction of the energy to be coupled into SPP modes at the Ag/BTO interface and the remaining to be transmitted or reflected. The SPP mode extends evanescently into both the metal and ferroelectric films, and the SPP wavevector, $\mathbf{k_{SPP}}$, is determined by the optical properties of both layers. The two counter-propagating surface waves are scattered out from the interface into radiative modes at the opposite slit. The SPPs interfere with the transmitted light at each slit corresponding to their phase accumulation during propagation along the interface. Interference with the transmitted light can be modulated by changing the SPP phase via slit pitch or SPP wavevector. We designed experiments, complemented by full field electromagnetic simulations, based on planar arrays of these devices (figure 6.2) to investigate optical modulation in SPP mediated double-slit interferometers.

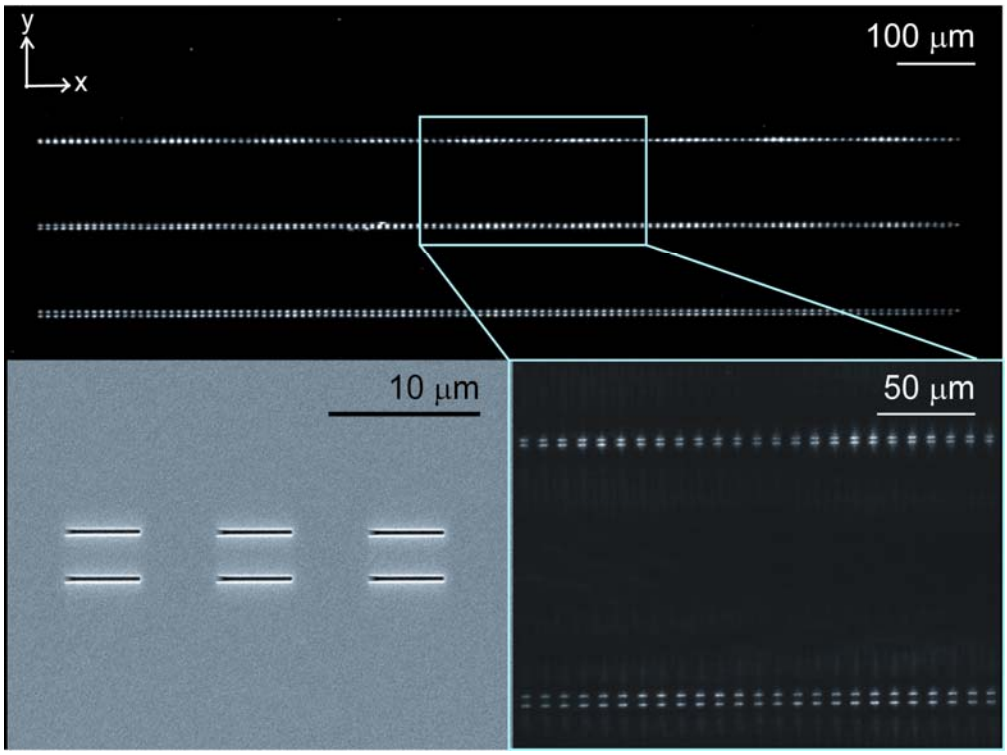

Figure 6.2. Double-slit SPP interferometer array. CCD image, collected with a 10X objective, of an array of double-slit devices patterned in Cr/Ag on BTO illuminated by TM-polarized (H-field parallel to the long axis of the slit) 688 nm laser diode light. The slit pitch starts at 0.50 μm and increases by 20 nm for each device along a row. The observed intensity oscillation as a function of slit pitch is due to SPP interference with light transmitted through each slit. Insets: Scanning electron micrograph of slit pairs milled by focused ion beam in a Cr on Ag layer. 50X image of devices with slit pitches varying from 1.50 to 1.98 μm showing one full period of transmitted intensity oscillation.

A simple analytical treatment of the total transmitted intensity resulting from interference between the incident field and the SPP field can be used to show that small changes in the index of refraction of the dielectric layer can lead to significant changes in the transmitted intensity profile. For this work, the double-slit device is governed by plasmon interference at the bottom interface of the Ag, due to the highly absorbing Cr layer at the top surface. Considering the transmission at each slit to be the sum of a transmitted field and a SPP field that has acquired some phase, $\phi = k_{SPP}x + \phi_o$, the resulting normalized transmitted intensity can be expressed as (*Pacifici et al. 2008*)

$$\frac{I_T}{I_o} = 1 + \left(\beta_o \beta_o^{'}\right)^2 e^{-\alpha x} + 2\beta\ \beta_o^{'} e^{-\frac{\alpha}{2}x} \cos\left[k_{SPP} x + \phi_o\right] \quad , \tag{6.1}$$

where β_o and β_o' are scattering efficiencies for SPP coupling at each slit, α is the absorption coefficient, k_{SPP} is the SPP wavevector and ϕ_o is the phase imparted by scattering from the slit. Data from experiments and full field electromagnetic simulations have been fit by this model to extract the relative index change of the active BTO layer from $n_{SPP}=\sqrt{\varepsilon_{Ag}\varepsilon_{Eff}/\left(\varepsilon_{Ag}+\varepsilon_{Eff}\right)}$ where ε_{Eff} is an effective dielectric constant describing the properties of all non-metallic layers (*Raether 1988*).

6.2.3 Finite Difference Time Domain Simulations

To explore the physics of this double-slit device, simulations were performed using full field finite-difference time-domain software (FDTD) (*OptiFDTD 2005*). A multi-oscillator Lorentz-Drude model is used for the Cr and Ag layers with parameters given by Rakic et al. (*Rakic et al. 1998*). The BTO and SRO complex refractive index data used were derived from VASE measurements (*Dicken et al. 2007*). Figure 6.3A shows the magnetic field profile (H_y) for one device with a slit pitch of 1.50 μm and an index of refraction, $n_{BTO,}$ of 2.20 for the BTO layer. The input plane wave (λ = 688 nm) from Z = 1 μm is transmitted through the 100 nm wide slits and a fraction is scattered into surface plasmon polariton modes propagating along the Ag/BTO interface to the left and right of each slit. Counter-propagating SPPs along the interferometer arm formed between the slits interfere constructively or destructively depending on slit pitch and SPP wavevector. Figure 6.3B shows the absolute magnetic field ($|H_y|^2$) from the same simulation. The resonant mode formed by the two counter-propagating SPPs inside the cavity can be identified in this figure. SPPs propagating away from each slit appear in the form of a continuously decaying intensity profile along the Ag/BTO interface. Figure 6.3B also shows fields being coupled into a waveguide mode formed by the 400 nm BTO film. At each slit, a fraction of the incoming energy scatters out of the SPP mode and interferes with the transmitted light to create an overall modulation in the transmitted power. The optical power flow through the device can be analyzed for these simulations by plotting the Poynting vector (S_z) (figure 6.3C).

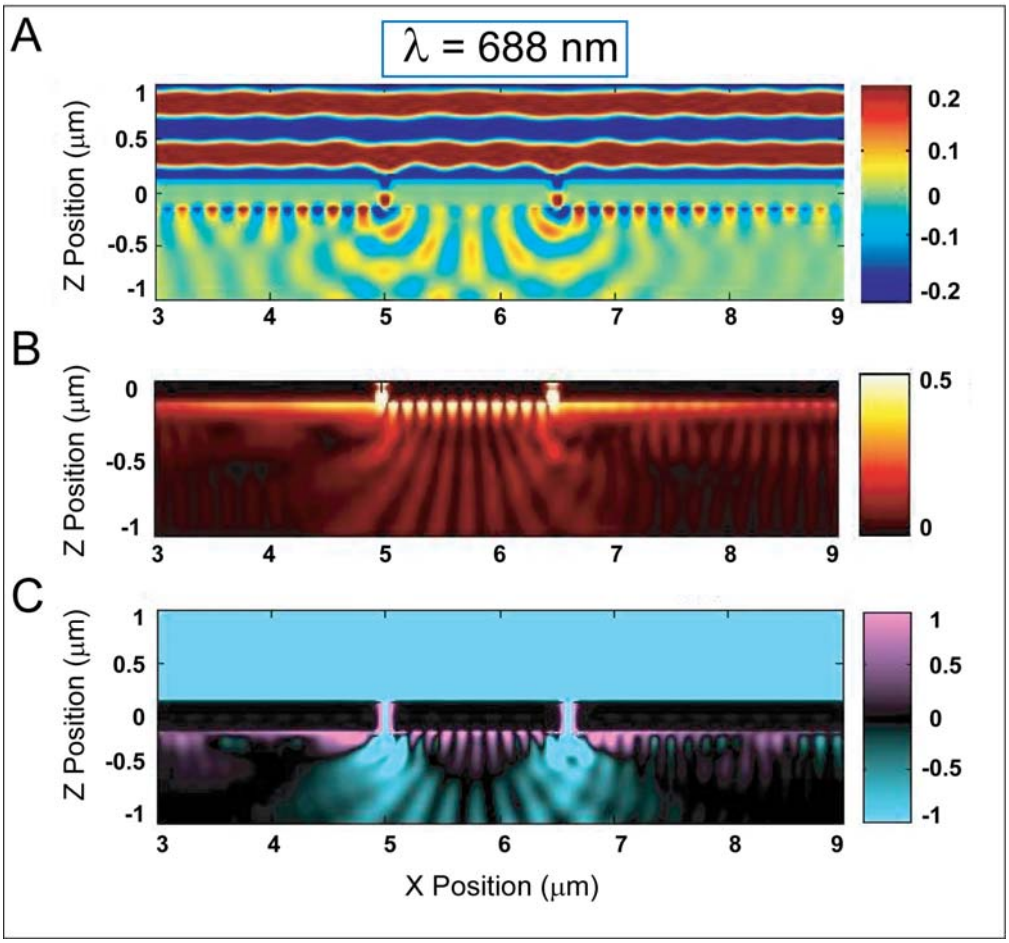

Figure 6.3. FDTD device simulations. Full-field finite difference time domain simulations of a double-slit SPP interferometer device with a slit pitch of 1.50 μm illuminated by λ = 688 nm plane-wave light. (A) Magnetic field (H_y) distribution for the device structure showing the destructive interference of the counter-propagating SPPs between the slits. (B) Absolute magnetic field ($|H_y|^2$) showing the standing wave mode formed by the counter-propagating SPPs as well as the slowly decaying SPPs propagating away from each slit. (C) Power flow (S_z) simulation used to quantify the relative power leaving the modeled devices at position Z = -1 along the X position.

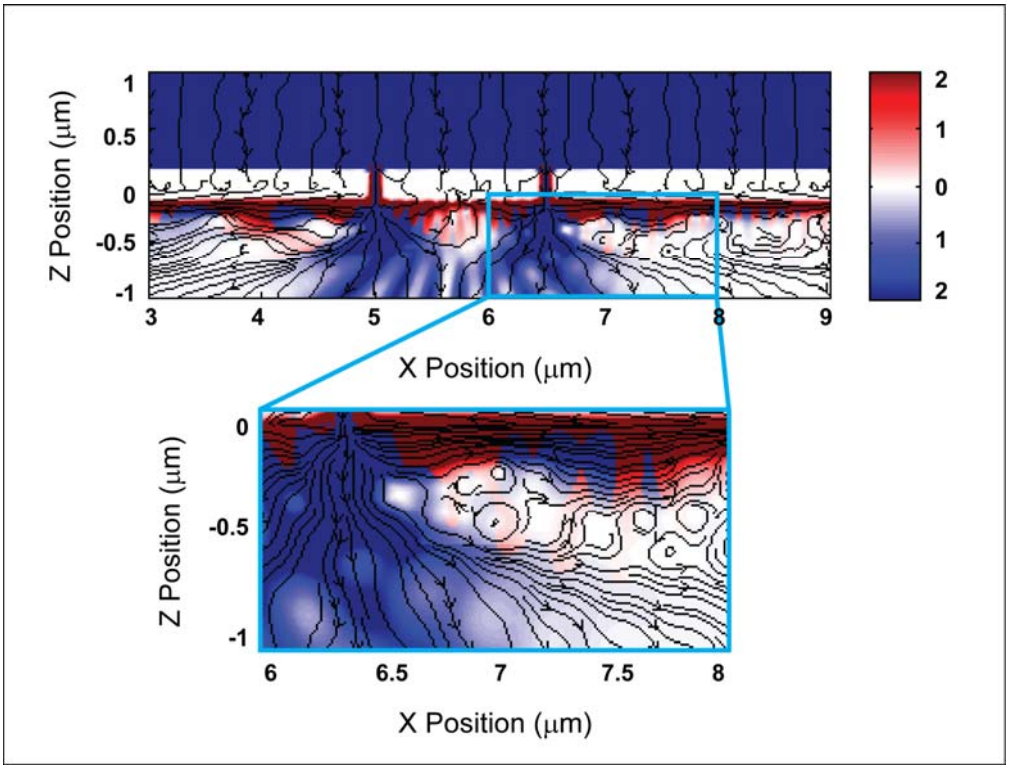

Figure 6.4. Poynting vector streamlines. Streamlines showing the direction of power flow out of the double-slit interferometer. (Inset) Exploded view near a single slit showing the forward and backward flow of power.

A monitor line placed along the bottom of the simulation (Z = -1 μm) can be used to monitor the net "transmission," that is, the power flow away from the slit pair in the –z direction. Plotting the integrated power flow out of the device for each slit pitch yields an interference pattern as predicted from theory (figure 6.5A). Simulations were done for these devices using input BTO indices of refraction of 2.20 and 2.21 to approximate the index change under applied bias. The range of indices simulated is indicative of a change in index due to some degree of a-domain to c-domain switching under bias. These FDTD data were fit using equation (6.1) to extract n_{SPP} and n_{Eff} following from $\varepsilon_{Eff} = n_{Eff}^2$. We find that comparing simulations with $n_{BTO} = 2.20$ and 2.21, the model fit yields $n_{SPP} = 2.626$ and 2.646 from which $n_{Eff} = 2.24$ and 2.25 respectively, corresponding to a change $\Delta n_{Eff} = 0.01$ (figure 6.5A). The difference in n_{Eff} from the input n_{BTO} is due to SPP interaction with the entire material stack beneath the BTO, which is naturally addressed in the FDTD simulation, but not in the analytical model. This does not affect the overall change in index, both the input

and simulated index change is $\Delta n = 0.01$. It is important to note that the intensity of the modulation is indicative of the change in n_{SPP} for a given slit pitch and material index, and can be used to put a lower limit on the index change for a given device. The percentage change in integrated power flow for each device, as n_{BTO} is changed from 2.20 to 2.21, is plotted in figure 6.4B. We can infer that the smallest change in n_{Eff} to yield 15% modulation for a device with pitch 2.26 μm with the optical material properties simulated here is $\Delta n_{Eff} = 0.01$.

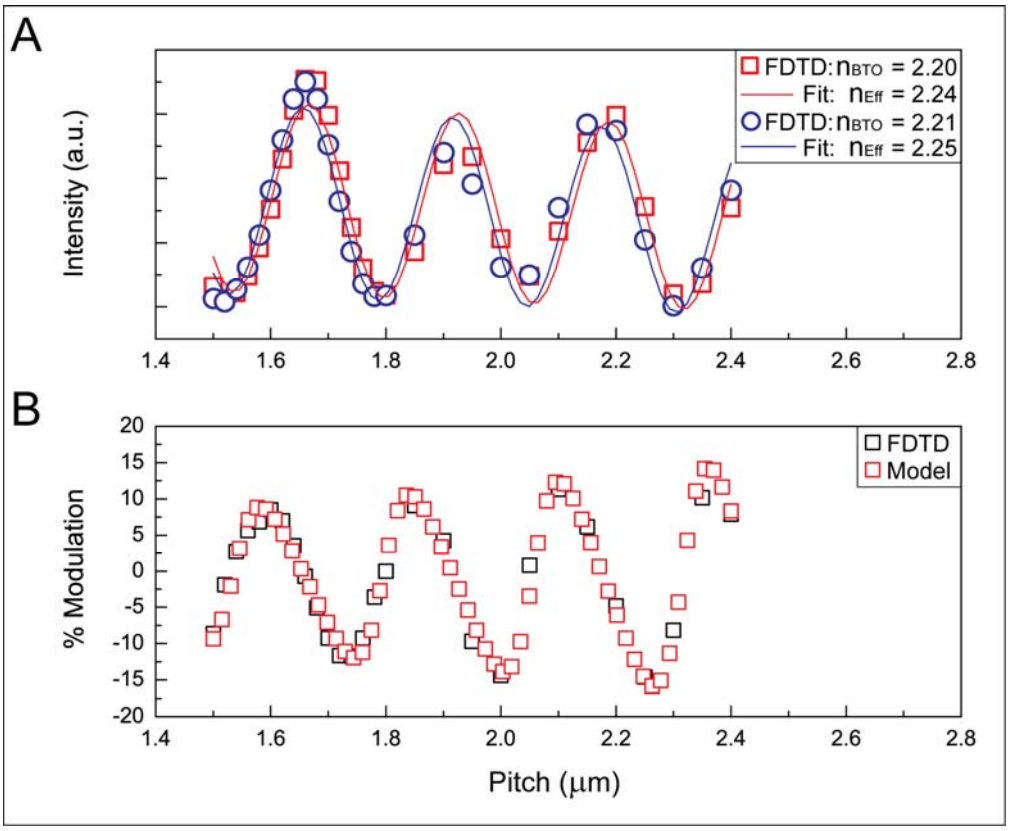

Figure 6.5. FDTD and analytical model validation. Integrated power flow from FDTD simulations of devices from 1.50 to 2.40 μm and experimental results for devices from 0.50 to 5.25 μm fit using equation (6.1). (A) FDTD data for BTO indices of $n_{BTO} = 2.20$ and 2.21. The model fit for these results yields SPP indices of $n_{SPP} = 2.626$ and 2.646 and the extracted $n_{Eff} = 2.24$ and 2.25. (B) Signal modulation from both FDTD data and model fit agree well.

6.3 Experiment

We fabricated an array of double-slit interferometer structures in silver on BTO (figure 6.2). The double-slit device array was illuminated from the topside, normal to the sample, with a TM-polarized (λ = 688 nm) diode laser source. The diode laser was aligned to the optical axis of a Zeiss Axiovert 135 inverted microscope using a quartz cube beamsplitter. The laser spot was expanded to uniformly cover the 2 X 2 mm device array and approximate a plane wave source from the Gaussian beam. A microscope objective (10X, N.A. 0.25) was used to collect transmitted light into a liquid nitrogen cooled Si CCD camera. A clear modulation in the transmitted intensity can be seen in the first and second rows, where the device pitch varies from 0.50 to 5.28 μm. At 50X (NA 0.45) magnification (figure 6.2, inset) a clear distinction between each slit can be seen, as well as one full period of intensity oscillations due to the interference of the out-coupled SPPs with the transmitted light.

The intensity profile along each row of devices under both zero and applied bias was monitored to understand the dynamic switching properties of the interferometer. The overall transmitted intensity from each device was integrated over the device area and compared along each row. Figure 6.6B shows transmission data from the first two rows of devices (pitch: 0.50-5.28 μm) with an expanded view of devices spanning the pitch range 2.52-2.80 μm. Devices in pitch range 2.52-2.80 μm were fit using the analytical model (equation (6.1)) and show an electrooptic change in the SPP index of Δn_{SPP} = 0.001 at 45 V applied bias (figure 6.6A). Modulation of the transmitted intensity profile for all devices in the range shows up to 15% change in the signal compared to 0 V. A change in index of this magnitude suggests some degree of a-domain to c-domain switching in the active BTO layer. The intensity modulation data also suggest that each device did not undergo the same change in n_{SPP}. To investigate this further, we plotted the theoretical change in both the interference pattern and the percent modulation approximating electrooptic switching (Δn_{eo} = 0.001) and domain switching ($\Delta n_{a\text{-}c}$ = 0.03) effects (figure 6.6C). We also observed that in some regions, the device transmittance departed from the prediction of the analytic model due to local changes in n_{Eff} arising from changes in either the Ag/BTO index or local film inhomogeneities.

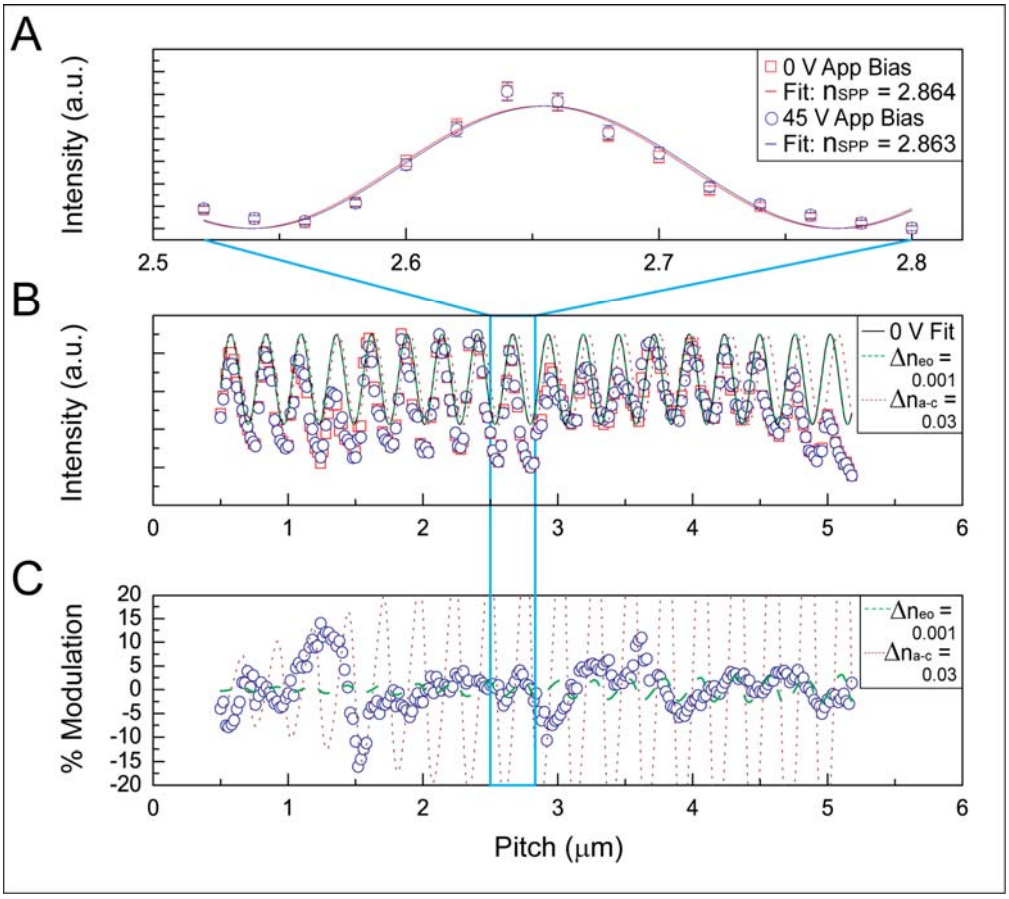

Figure 6.6. Experimental double-slit transmission modulation. (A) Analytical model fits for experimental device response with pitches 2.52 to 2.80 μm show an electrooptical change in the index of $\Delta n_{SPP} = 0.001$. (B) Experimental data and fits for devices at 0 and 45 V. The dashed lines are theoretical interference patterns corresponding to $\Delta n = 0.001$ and 0.03 for electrooptic and domain reorientation effects respectively. (C) Experimental data for devices under 45 V applied bias show modulation up to 15%, compared to 0 V. The dashed lines are the theoretical modulation for changes in index of $\Delta n = 0.001$ and 0.03. Devices in the range 1.75 to 2.75 μm show modulation on the order of the electrooptic effect while devices from 1.00 to 1.50 μm show much larger modulation due to domain reorientation.

Intensity data were compiled in 5 V increments from 0 to 45 V and the percent change in intensity compared to 0 V is plotted in figure 6.7. We see a reasonable comparison of the modulation data for devices with pitches in the range 0.50-1.00 μm with theoretical modulation due to electrical modulation of the SPP wavevector, via domain switching effects on the order of $\Delta n_{Eff} = 0.03$.

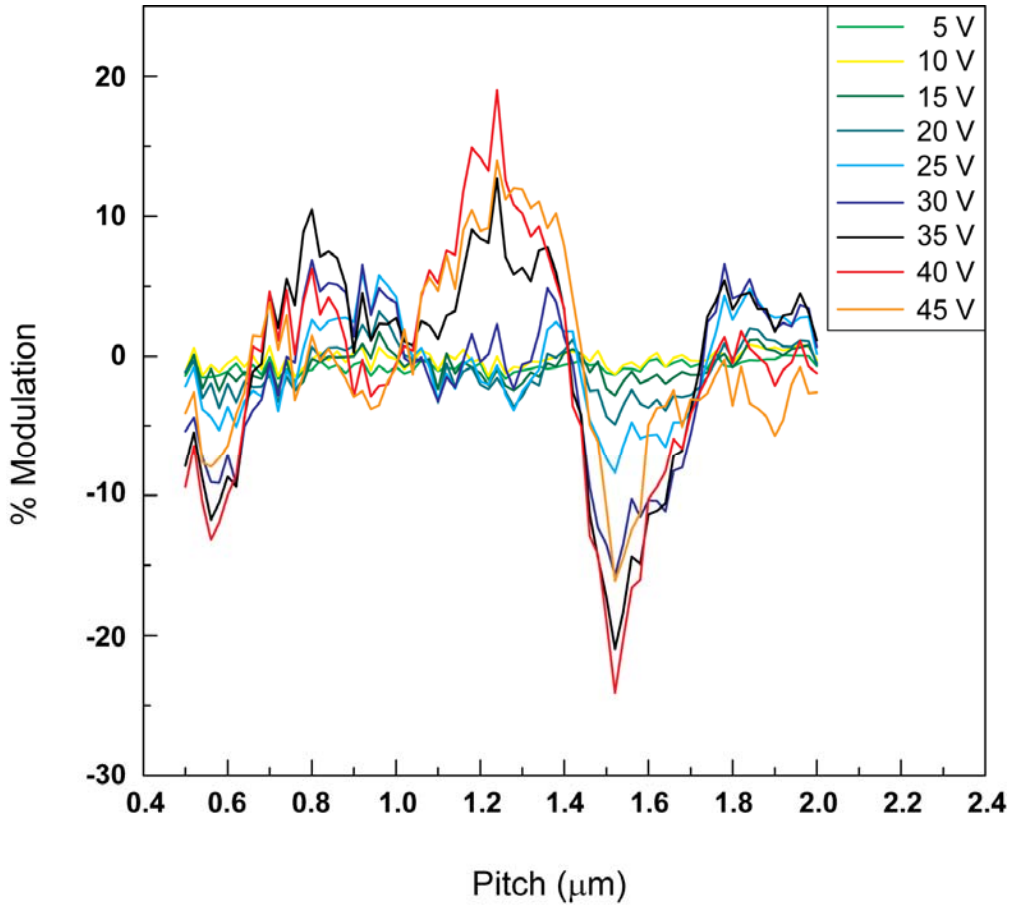

Figure 6.7. Experimental observation of SPP modulation. Data collected by inverted microscope and spectroscopic ellipsometer show evidence of optical index change inducing modulation in propagating SPPs. Experimentally measured signal modulation for devices in the range of 0.50-2.0 μm slit pitch, under polarized λ = 688 nm light. The intensity modulation shows areas where index change is on the order of electrooptic effect and a-domain to c-domain switching induced. The large signal increase between 30 and 35 V is attributed to a-c domain switching.

For slit pitches less than 1.00 μm, the maxima and minima of the intensity modulation correspond well with the inflection points of the 0 V interference pattern. This implies that the change in index from device to device was similar in this range. Devices between 1.00 and 1.80 μm slit pitch show the largest change in intensity modulation. By comparing the data in this range to the percentage modulation of the analytical model, we can put a lower limit of $\Delta n_{Eff} = 0.03$ on the index change in these devices. This larger effect is attributed to domain switching or piezoelectric activity in the BTO film, such that devices showing very large intensity modulation are undergoing 90° domain switching from c-axis in-plane to c-axis out-of-plane (*Kim et al. 2005*). This effect would yield a change in the index of

refraction on the order of the birefringence of the material, $\Delta n = 0.05$. The fraction of domains that switch between the slits of each device will dictate the change in effective index for the device.

To investigate this further, the bias across the devices was cycled from 0 to 45 to0 V. A plot of the response of three devices (1.60, 1.62, 1.64 μm slit pitch) to the voltage cycle is shown in figure 6.8. The intensities of these devices were normalized to their values at 0 V. The device response shows hysteresis demonstrative of ferroelectric domain switching.

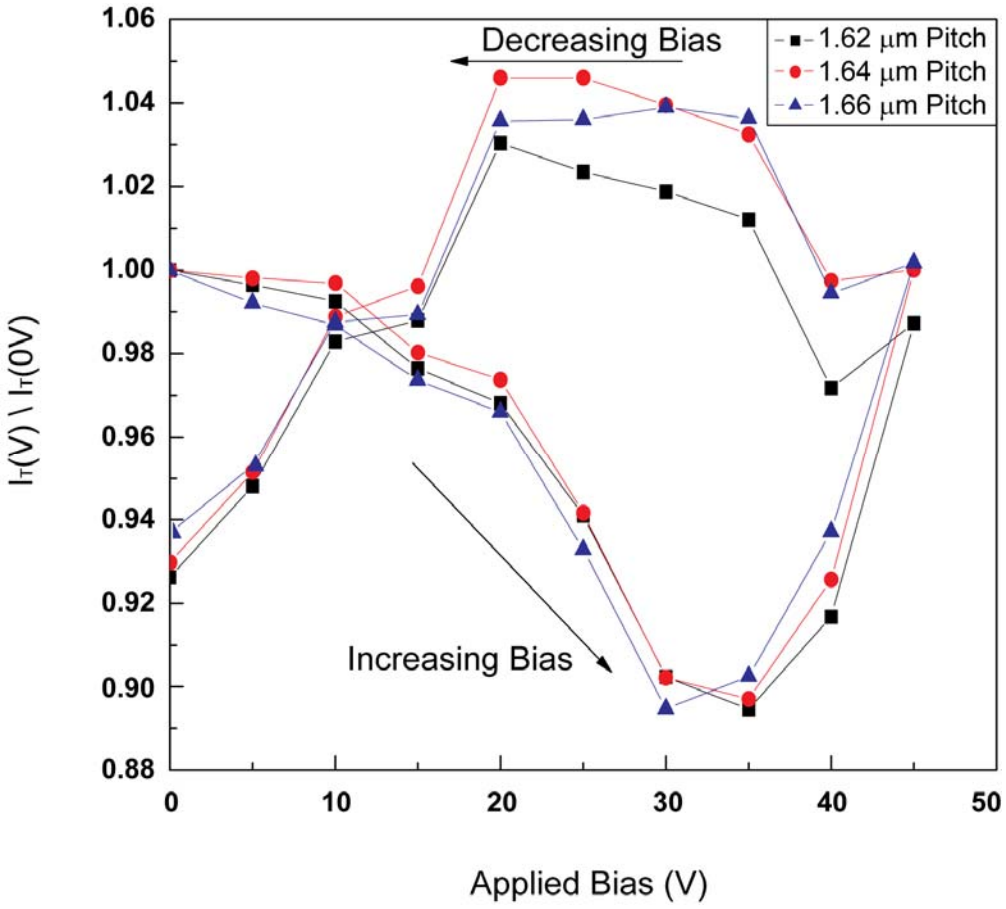

Figure 6.8. Modulation hysterisis in double-slit arrays. Devices in the pitch range with the largest modulation show expected hysteretic behavior due to domain relaxation.

As the bias is increased, devices in this range show a decrease in output intensity as the index changed up to 35 V, and the following increase in intensity suggests that the index change was sufficient to move the response through a minimum in the interference pattern. As the bias is decreased, the domains that have switched from c-axis in-plane to c-axis out-of-plane

relax slowly to their original state. At 15 V, decreasing bias, the index begins to follow the same path through the intensity minimum.

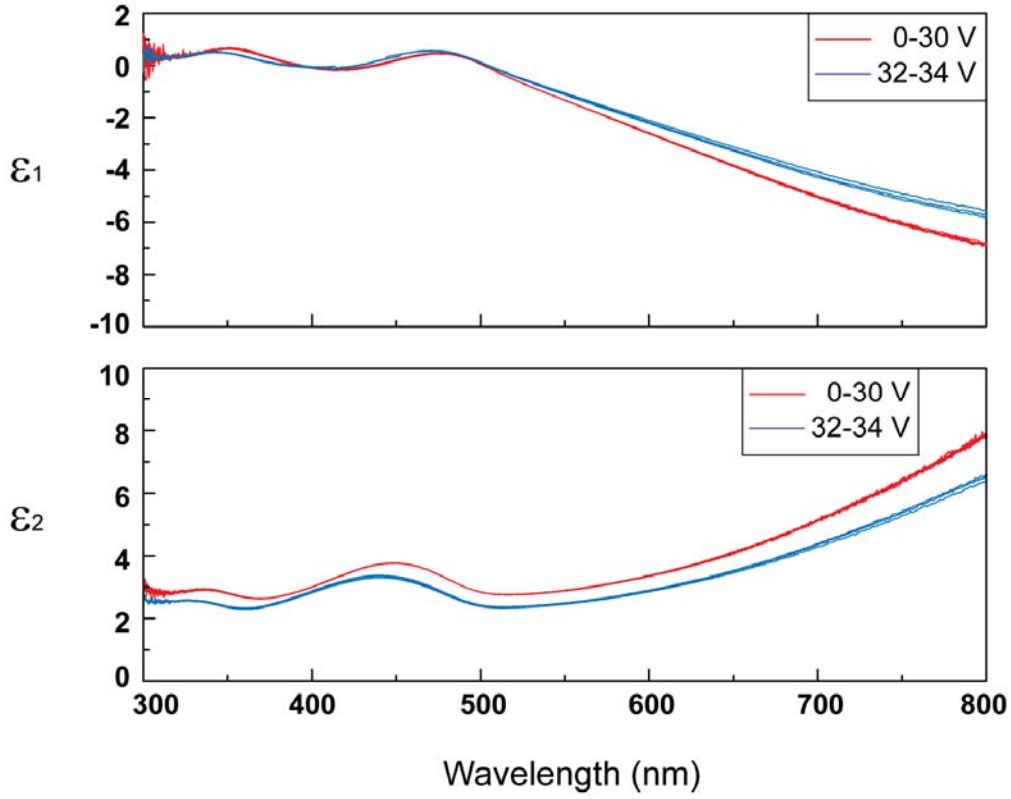

Figure 6.9. Optical validation of domain switching. Spectroscopic ellipsometry confirms large index change, on the order of $\Delta n = 0.03$, between 30 and 32 V applied bias.

Finally, we performed an independent confirmation of the large refractive index change due to domain switching. This effect was investigated using spectroscopic ellipsometry in a separate planar sample with a 20 nm, optically transparent, silver film evaporated on the same BTO / SRO / MgO film stack. Shown here (figure 6.9) are the ε_1 and ε_2 data, as measured by VASE, under applied voltage from 0 to 35 V. The change in ε_1 and ε_2 at 30 V corresponds to $\Delta n = 0.03$ at 688 nm which is on the order of the change due to domain switching seen in the plasmonic interferometers.

6.4 Conclusions

The phenomena of SPP-mediated interference using a pair of sub-wavelength slits in silver on BTO thin films has been investigated by a simple analytical model, full-field finite difference simulations and experiment. Electrical modulation of the SPP wavevector was achieved by utilizing the electrooptic effect as well as 90° domain switching in BTO. The degree of optical switching obtained in these devices is potentially useful for designing new plasmonic and metamaterial structures in which active oxide replaces a static dielectric material. As photonic networks become more prevalent in chip-based microelectronic systems, the need for active nanoscale devices is increasingly apparent. Active plasmonic devices, based on electrooptic modulation, are well suited to fill this nanophotonic niche.

Chapter 7
Active Metamaterials in the Near-Infrared

In this chapter we present the first active, frequency-tunable, metamaterial devices operating in the near-infrared spectrum from 1.5 to 5 μm. These devices are based on typical split-ring resonator (SRR) structures fabricated on the vanadium oxide (VO_2) thin films discussed previously in this thesis. Metamaterial arrays were designed, simulated, fabricated and tested in our lab.

7.1 Introduction

Electromagnetic resonances in subwavelength metallic structures fabricated on dielectrics can be used to engineer optical responses not found in natural materials (*Enkrich et al. 2005, Shalaev 2007, Smith et al. 2004*). These "metamaterials" have reemerged from their initial incarnation (*Veselago 1968*) and are currently subject to intense investigation for their applications in super lensing (*Pendry 2000*), optical cloaking (*Cai et al. 2007*) and negative index (*Shalaev et al. 2005*). Recently, active metamaterials have been demonstrated over a narrow range around 1 THz using photoexcitation in semiconductors (*Chen et al. 2006*) and the metal-insulator phase transition in VO_2 (*Driscoll et al. 2008*). Engineering metamaterials with tunable resonances near communications wavelengths would have a profound effect on on-chip optical devices. Here, we demonstrate frequency-tunable metamaterials based on Ag/ and Au/VO_2 hybrid structures in the near-IR range from 1.5 to 5 μm. Hybrid Ag/ and Au/VO_2 structures allow optical and geometrical engineering of metamaterial devices leading to resonant peak position tuning and frequency shifts up to half a line width.

Metamaterial designs span the electromagnetic spectrum from millimeter waves (*Smith et al. 2000*) to the near-IR (*Soukoulis et al. 2007*). Typical metamaterials consist of arrays of metal structures embedded in a dielectric with feature sizes much smaller than the desired operating wavelength. In the simplest sense, each unit cell of the array is considered to be an individual LC circuit with resonant frequency $\omega_o \sim \sqrt{1/(LC)}$ (*Linden et al. 2004*). SRRs are the basis for many metamaterial designs due to the ease with which they may be

fabricated and modeled. A SRR is a metal ring with inductance, L, with a single notch where charge build up gives rise to a capacitance, C. These two parameters are, in general, set by the choice of materials and resonator dimensions leading to fixed metamaterial resonances. Active metamaterial designs previously focused on changing the capacitance in the SRR gap to modulate the amplitude of the resonance (*Chen et al. 2006, Degiron et al. 2007*). Integrating materials with tunable electrical or optical properties allows further control over the resonant response in metamaterials. VO_2 exhibits novel material properties arising from a structural phase transition from monoclinic to rutile (*Narayan et al. 2006*). Here, we investigate active, self-aligned, hybrid SRR structures on VO_2 as a route toward tunable metamaterial response in the near-IR through control over the resonator geometry and optical properties.

7.2 Device Design

VO_2 undergoes a structural transition from an insulating monoclinic phase to a metallic rutile phase at ≈70 °C. During this insulator-metal transition the conductivity increases by as much as six orders of magnitude and the optical transmission in the near-IR decreases from ≈70% down to ≈5%. This phase transition occurs on the order of picoseconds and can be instigated by thermal, optical (*Lysenko et al. 2006*) and electrical (*Chae et al. 2005*) means. Our active metamaterial device concept consists of self-aligned Au/VO_2 SRR-type structures. By utilizing the insulator-metal phase transition in VO_2 we can control the overall device dimensions as well as the effective optical properties of the hybrid-SRR arrays in both phases. A schematic of the self-aligned hybrid-SRR unit cell is shown in figure 7.1. When the active material is in the insulator phase, the arrays act as metal SRR-type metamaterials on VO_2 substrates. In the VO_2 metallic phase the resonant response can be modeled as a hybrid-metal/VO_2 metamaterial with total thickness equal to the combined layers. It is expected that this change in thickness causes the effective capacitance of the SRR increase and the resonant frequency to decrease. This new hybrid-SRR is now situated on a sapphire substrate with a larger dielectric constant, ε_s, also lending to the resonant frequency shift, which scales as $1/\sqrt{\varepsilon_s}$ (*Padilla et al. 2006*).

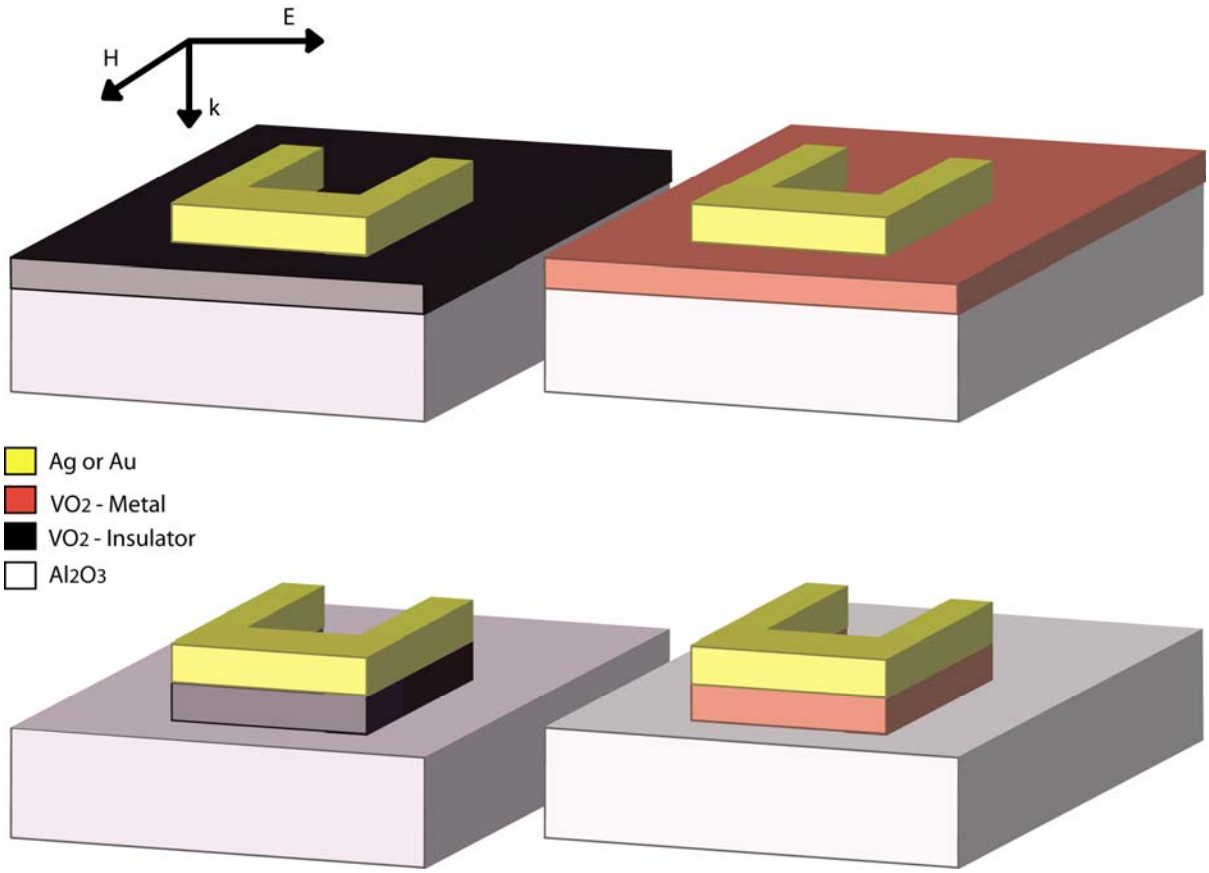

Figure 7.1. VO_2-based hybrid-SRR metamaterials. Schematic of Metal/VO_2 hybrid-SRR metamaterial unit cell. The metal layer is <100 nm to increase the EM interaction with the underlying VO_2. Upon switching, the hybrid-SRR increases in thickness, changing the overall capacitance and inductance.

VO_2 thin films are grown epitaxially by pulsed laser deposition on c-plane Al_2O_3 substrates at 500 °C. A vanadium metal target is used as the source material and deposition takes place in 12 mTorr oxygen. VO_2 films (≈100 nm) are deposited with a 300 mJ laser pulse at a rate of 10 Hz. The metamaterial arrays are fabricated using standard electron beam lithography (950K A4 PMMA resist). Arrays were investigated using both Au and Ag as the metal layer. Evaporation of a 3 nm titanium adhesion layer is used for Au SRR samples, Ag SRR samples are deposited directly. The remaining PMMA is removed during the metal lift-off step leaving only the patterned SRR array. Scanning electron microscopy images showing one metamaterial design, an SRR coupled to a nearby bar, studied in this thesis are shown in figure 7.2.

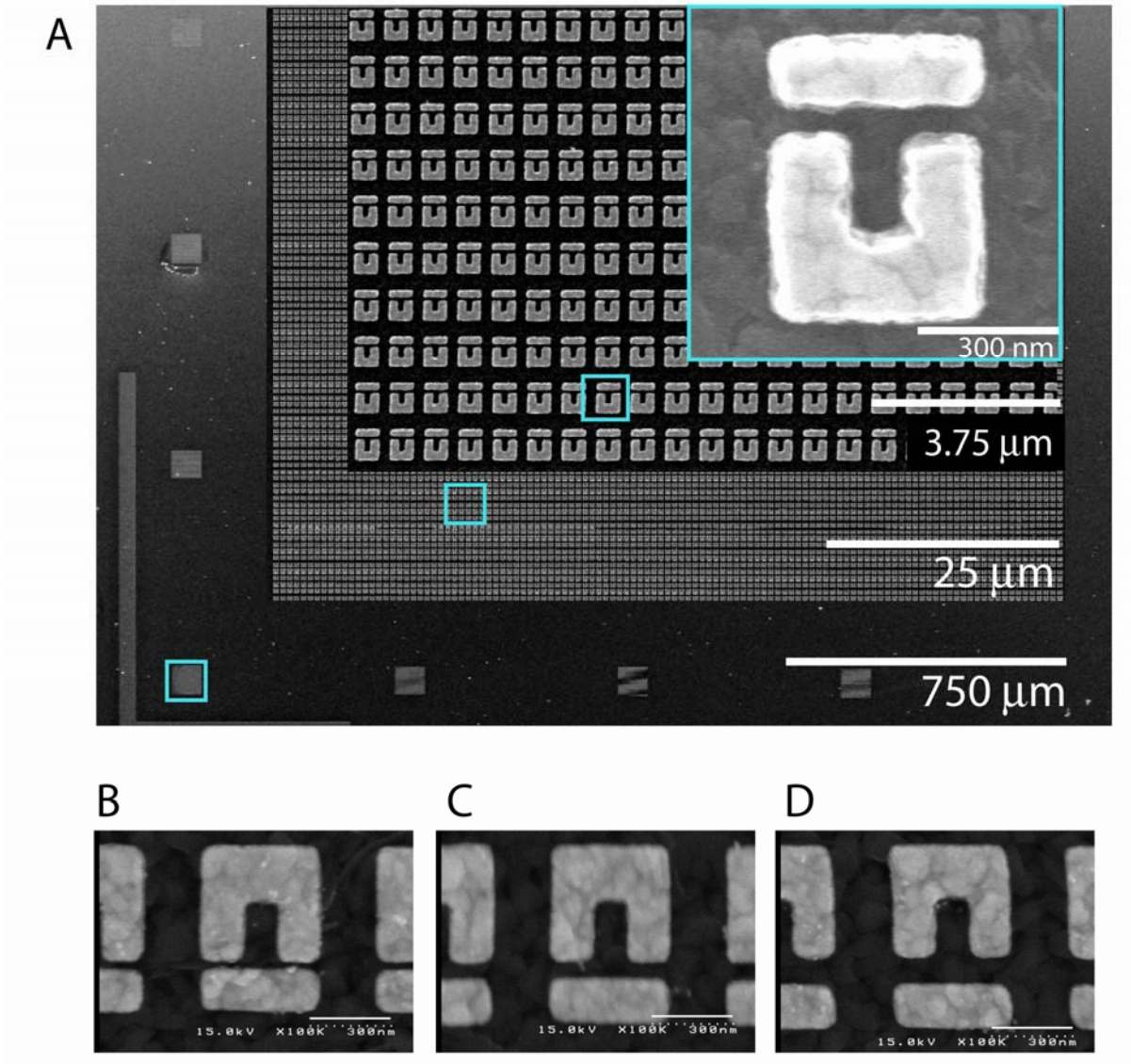

Figure 7.2. SEM images of coupled-SRR arrays. (A) A sample metamaterial array studied in this work based on coupling the typical SRR to a nearby metal element. SRR structures show good fidelity over the entire 70 X 70 µm array. Various SRR unit cell designs were studied, one such design is a typical SRR coupled to a straight bar. (B) 30 nm, (C) 60 nm, and (D) 90 nm gaps are shown. Coupled-SRR designs yield multiple resonances in the near-IR spectrum at these dimensions. Engineering the gap distances and SRR arm lengths is used to tune the resonant peaks across the near-IR spectrum.

7.3 Metamaterial Response in the Near-Infrared

7.3.1 Planar, VO_2-Based, Hybrid-SRR Metamaterials

Metamaterial arrays are illuminated at normal incidence through a FTIR microscope using a light source in the range of 1.5 to 8 μm. The incident E-field is polarized perpendicular to the SRR arms to efficiently couple to the capacitance inducing a circulating current in the structure. The measured reflection spectra are normalized to the reflectivity of an optically thick gold film. Figure 7.3 shows reflection spectra for 50 nm thick Ag SRR-based structures on 60 nm thick VO_2 thin films. These samples were heated using a commercial heating stage add-on comprised of a silver block with a millimeter-sized aperture milled in the center. Resonant peaks show no change as the temperature is increased from room temperature up to 60 °C. At 65 °C the resonant reflection peaks begin to red shift slightly and the reflectivity decreases as the VO_2 thin film changes phase. The phase change modifies the local fields in the SRR, acting like a tunable dielectric inside a capacitor. The resonance frequency of the SRR decreases (wavelength increases) as the VO_2 permittivity increases. This is expected from the simple RLC-circuit analysis discussed previously. This effect continues until 75 °C when the VO_2 phase change is complete and the SRR array is electrically shorted. Above the transition temperature, the sample reflectivity is dominated by the metallic VO_2 thin film. The resonances recover upon cooling below the phase transition temperature. Coupled-SRR metamaterials were similarly investigated. The resonant peak position in coupled-SRR can be tuned across the near-IR spectrum by changing the distance of the strongly coupled unit (figure 7.3A-E). After investigating the active resonant response of metal SRR arrays on planar VO_2 films, these samples were etched to create self-aligned, metal/VO_2-based, hybrid SRR metamaterials.

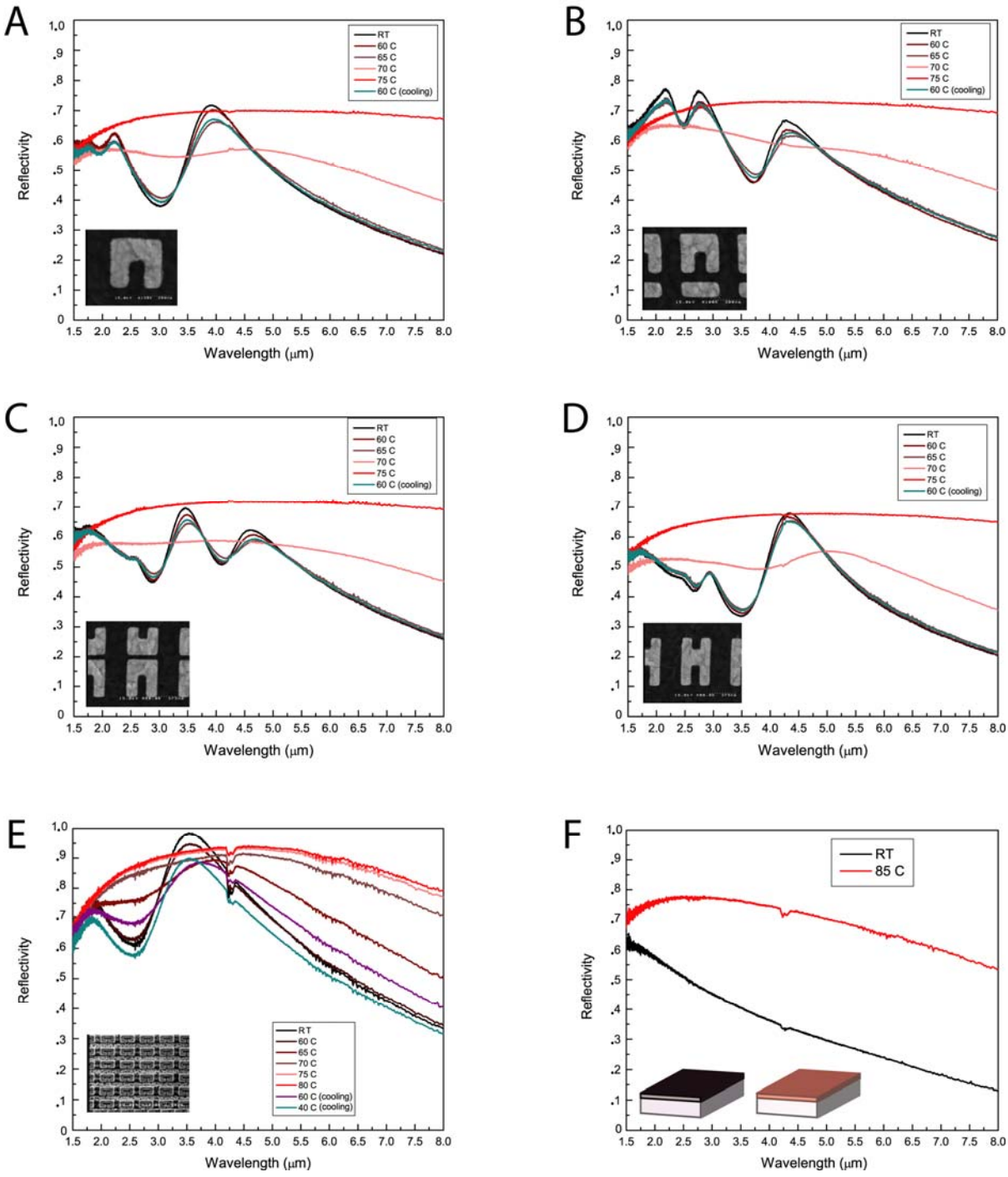

Figure 7.3. Planar, VO_2-based, SRR metamaterials. Near-infrared reflection spectra of 60 nm thick SRR-based Au metamaterial arrays (insets) on (A-D) 100 nm and (E) 50 nm thick VO_2 thin films. Spectra are taken as samples are heated above the insulator-metal transition temperature of VO_2 (≈70 °C). The phase transition onset is faster in the 100 nm VO_2 samples compared to the 50 nm VO_2 sample. In this range, resonant reflection peaks decrease as the SRR arrays become electrically shorted. The reflectivity of the VO_2 dominates above the phase transition temperature.

7.3.2 Self-Aligned, Metal/VO_2-Based, Hybrid-SRR Metamaterials

To fabricate self-aligned SRR metamaterials, two thin film etching techniques were investigated; ion-milling with Ar^+ ions and a CF_4/O_2 reactive ion etch (RIE). In both cases the metal SRR structure acts as the etch mask for the underlying VO_2 film. Ion-milled samples used a 10 nm Cr mask to protect the ≈100 nm Ag SRR pattern. 500 eV Ar^+ ions impinge on the sample for 90 seconds to etch the 50 nm VO_2 film. The CF_4 etch uses a 100 W oxygen plasma and 200 sccm CF_4 to etch the VO_2 film. This reactive ion etch is less destructive to the SRR pattern. Etching Au SRRs using a CF_4 RIE does not require an additional Cr layer to protect the array. Ag, however, oxidizes and becomes mottled and slightly etched under these conditions so a 5 nm Cr layer was still employed.

Figure 7.4 shows the optical response of self-aligned, 50 nm Au / 100 nm VO_2, hybrid-SRR metamaterials. In all cases, etching the array to create the self-aligned structures causes a blue shift of the resonant wavelength by ≈1.5 μm. The resonant peak full-width at half-maximum also decreases due to the decreased reflectivity from the sapphire substrate compared to the previous VO_2 film. Figure 7.4A shows the effects of changing SRR dimensions on the metamaterial resonance. Shrinking the arm lengths decreases the effective area and hence the capacitance, $C = \varepsilon A/d$, of the SRR thereby increasing the resonant frequency. Figure 7.4B shows the optical response of SRRs coupled to a nearby bar structure. The presence of the bar structure leads to a tunable magnetic resonance dependent on the SRR/bar distance. Smaller gaps lead to higher frequency resonances and a blue-shift of the reflection peak. The bar also has a fundamental electric resonance, at smaller wavelengths, that does not shift as the gap is varied. Coupled, facing, SRR structures are shown in figure 7.4C. These structures were varied by changing the arm lengths of one of the two SRRs. As the structure becomes more asymmetrical, two additional resonant peaks form in the reflectance spectra. A similar effect is seen for SRRs coupled back-to-back (figure 7.4D). Comparing figures 7.4D&E, we can identify the resonant peak splitting to be due to the coupling from the gap in the back-to-back coupled structures. Figure 7.4F show the optical response similarity of “facing” and “back-to-back” SRR coupling. Finally, the self-aligned structures were heated to investigate the change in reflection spectra above the VO_2 metal transition temperature.

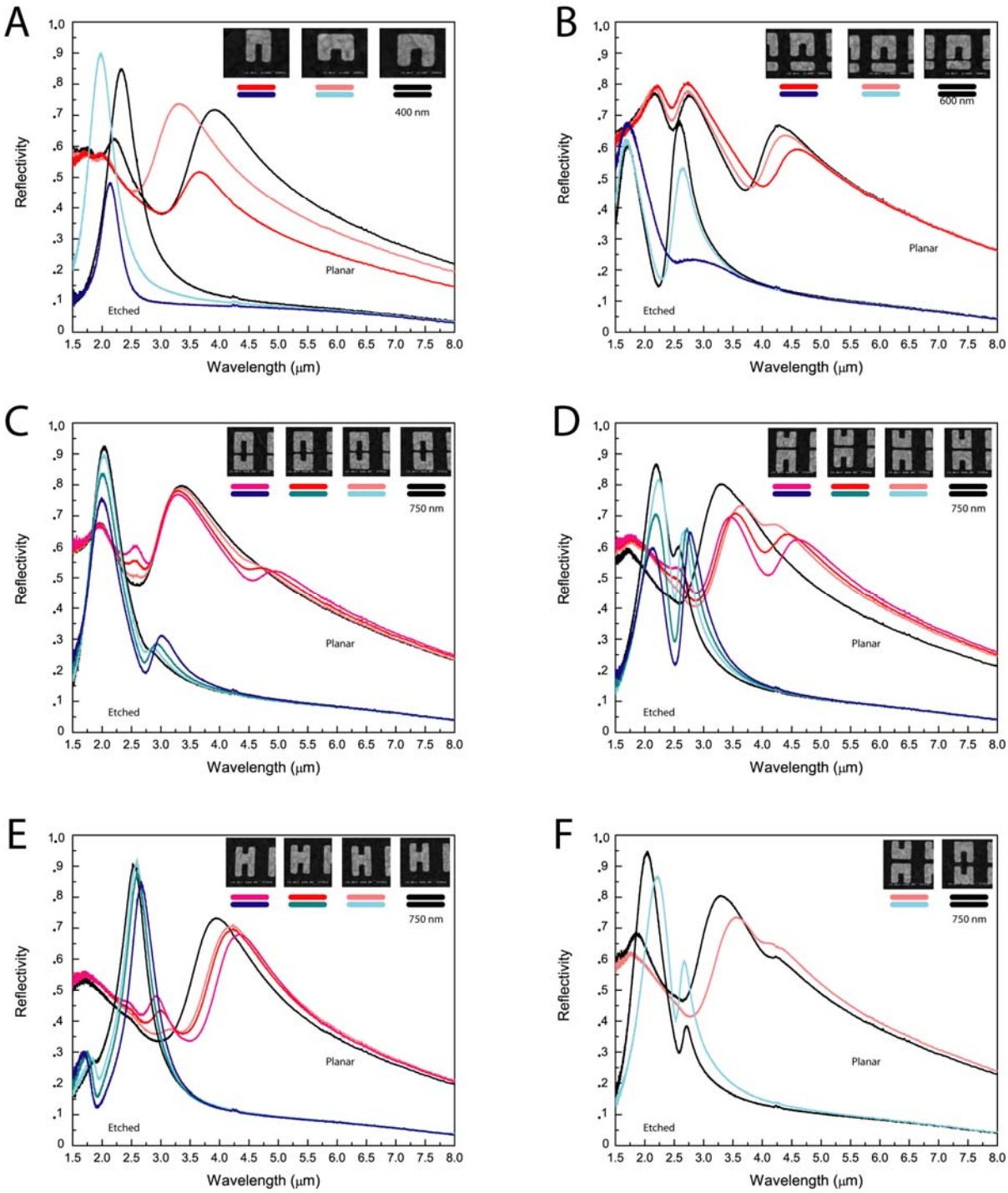

Figure 7.4. Self-aligned hybrid-SRR based metamaterials. 50 nm Au SRRs on 100 nm VO_2 thin films (red lines) are etched by RIE to form self-aligned SRR structures (blue lines). Reflection spectra of etched structures are blue-shifted by 1.3 to 1.6 μm and the line-widths narrow from ≈1.5 to 2.0 μm to 500 to 700 μm. (A-F) Effects of arm lengths and coupling distances are investigated in planar and etched structures.

7.3.3 Active, Frequency-Tunable, Hybrid-SRR Based Metamaterials

Resonant reflection response of self-aligned hybrid-SRR based metamaterials was investigated using the heating experiment described previously for planar hybrid-SRR arrays. Figure 7.5 shows the reflection spectra for the etched samples as the VO_2 changes phase. Compared to SRRs on planar VO_2, we see resonant reflection peak wavelength shifts of 60–110 nm upon VO_2 phase transition from insulator to metal. In all cases (figures 7.5A-F), the magnetic resonance peak shifts to lower frequency, longer wavelength. This can be explained, using the simple RLC model, due to the increased area of the metal/VO_2 hybrid-SRR. The VO_2 transition, from the insulator to the metal phase, causes the SRR thickness to increase from the metal array thickness to the combined metal/VO_2 thickness. This increase translates to an increased area of the capacitor plates in the SRR structures and a subsequent decrease in the resonator frequency. The increased absorption of the metal-phase VO_2, compared to Ag or Au, causes the resonant reflection peaks of the metamaterial to broaden slightly during switching. These metamaterials represent the first generation of tunable, VO_2-based designs. To further investigate VO_2 as a switching element in metamaterial arrays, we simulated these structures using finite-difference time-domain software.

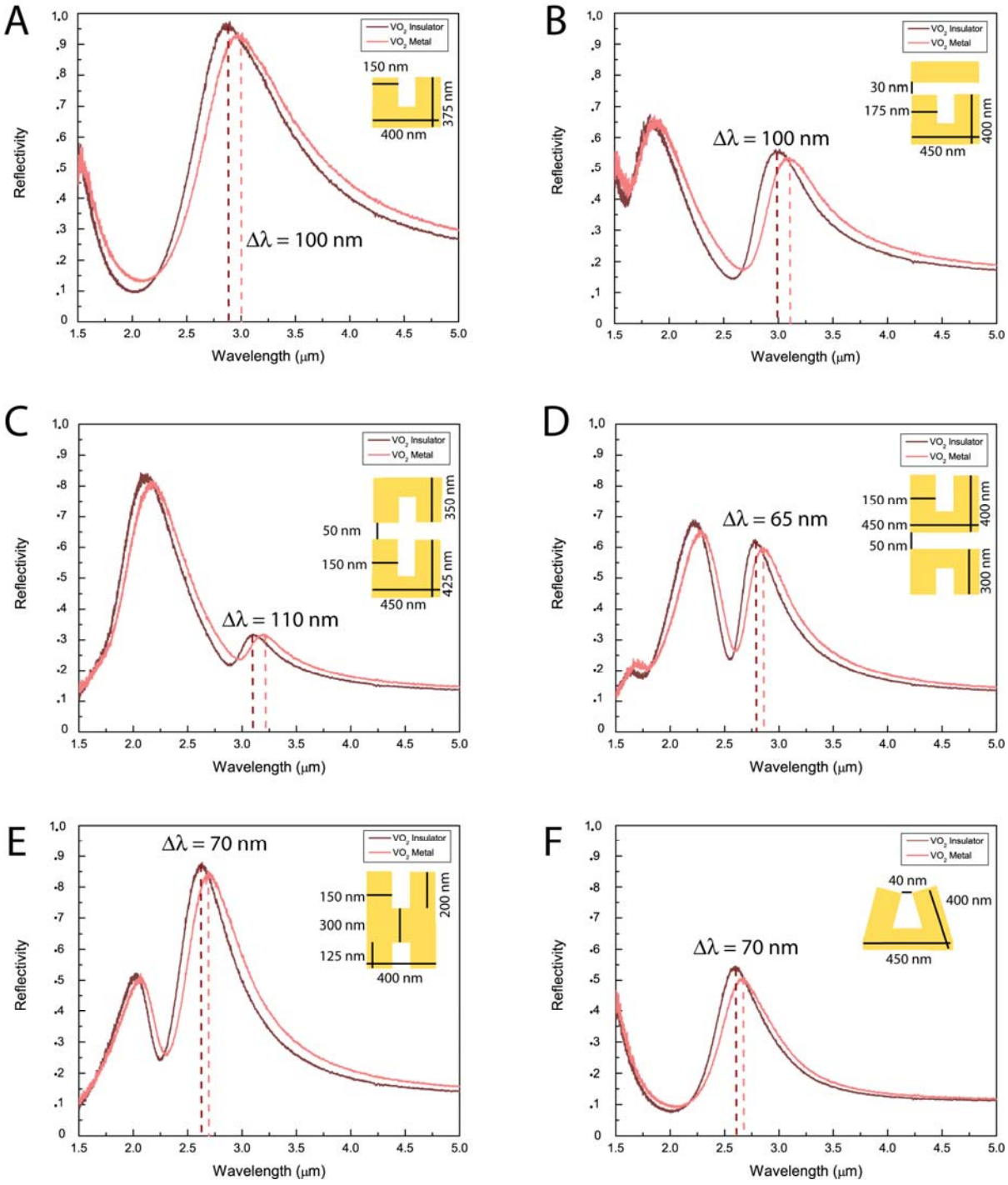

Figure 7.5. Active, frequency-tunable, hybrid-SRR based metamaterials. Resonant peak shifts from 65–110 nm are observed as the self-aligned Ag/VO_2 hybrid metamaterials are thermally switched above the VO_2 insulator-metal phase transition. These structures are ≈100 nm Ag with ≈30 nm Cr layers to protect the Ag during ion milling.

7.4 Simulated Optical Response in Metamaterials

Simulations of the self-aligned Au/VO_2 hybrid structures are shown in figure 7.6. To accurately simulate the metamaterial response, we measure the optical properties of the VO_2 thin films in both phases. Variable angle spectroscopy (VASE) is used to measure the complex dielectric constants of the VO_2 thin film in the insulating and metallic phases before patterning. Tauc-Lorentz and Drude oscillator models are used to fit the measured Ψ and Δ data from VASE and extract n and k in the respective phases (chapter 5). The optical data for both phases are used as inputs to simulate the metamaterial response by finite-difference methods using Lumerical, commercial software. Figure 7.6A shows the simulated response of a typical SRR metamaterial with dimensions reported earlier. The simulated response on planar VO_2 films matches experimental results well, using VASE data for the optical parameters. Figures 7.6B-D show simulations for other SRR structures investigated in this work. Resonant reflection response simulations compare well for arrays on insulating VO_2, however, metal-phase VO_2 shows slightly more absorption than seen in experiments. This can be due to the model used to fit the VO_2 optical data in the metal phase. Optical data for VO_2 in both phases was collected in the range of 300–2200 nm. To simulate the response in the near-infrared range, from 1.5 to 5 μm, the model fits were extrapolated to this range. Regardless of this fact, simulations of active resonant response in hybrid-SRR based metamaterial arrays are validated by experiments. Having shown that these simulations reflect experimental device response, we investigate a number of metamaterial arrays that have the possibility of larger optical response.

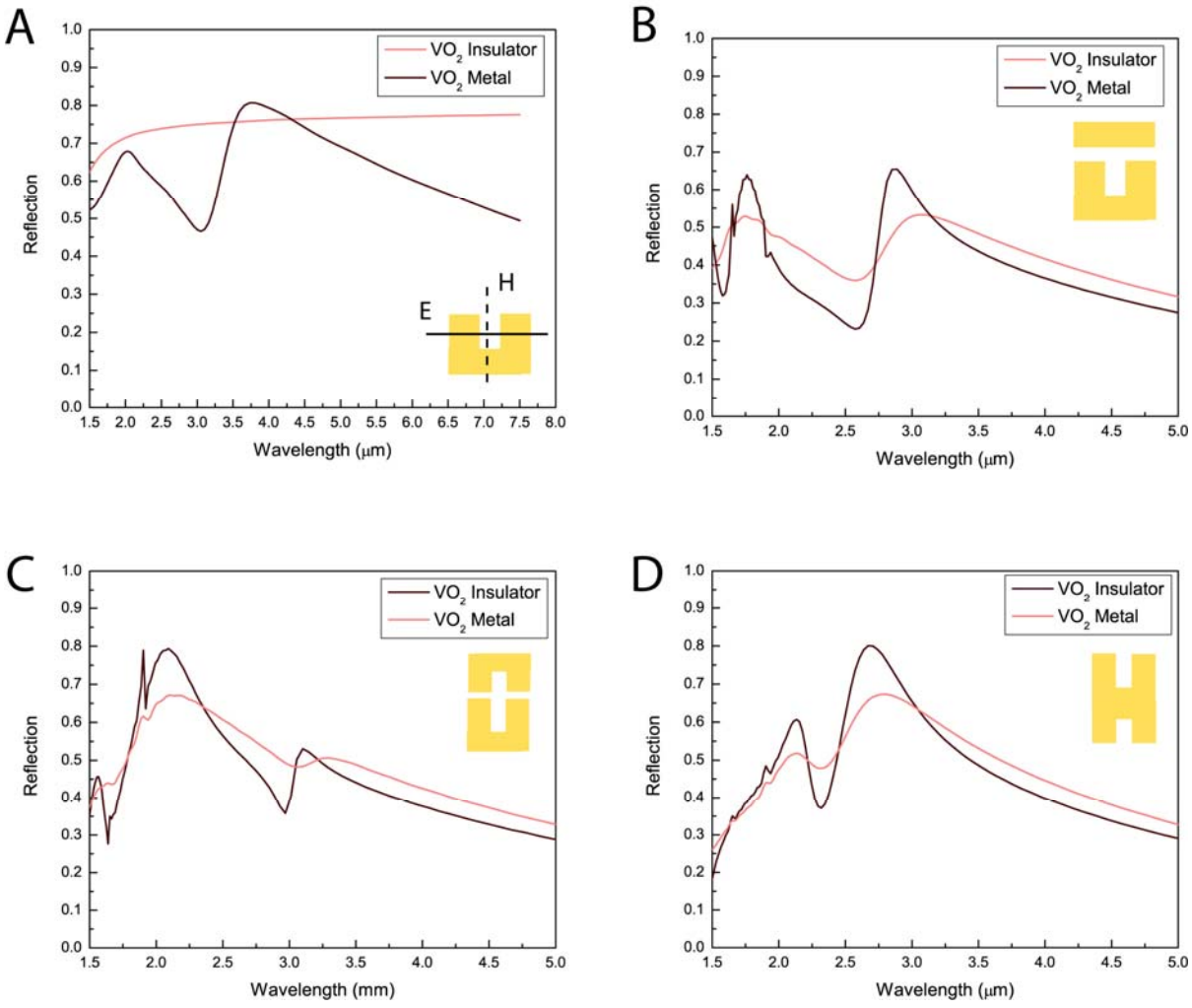

Figure 7.6. FDTD simulations of VO_2-based hybrid-SRR metamaterials. FDTD simulations of metamaterial optical response. (A) Au SRRs on planar VO_2 thin films. (B-D) Self-aligned, Au/VO2 hybrid SRR structures, polarized as in (A).

Figure 7.7 shows two possible designs for hybrid-SRR metamaterials using VO_2 as the active switching element. Figure 7.7A uses VO_2 to increase the arm length of the SRR in the metal phase. As discussed earlier, this change in SRR geometry results in a red shift of the resonant reflection peak. Changing the arm length by 150 nm in this way shifts the peak resonance from 3.0 to 3.5 μm and the reflectivity at 3.0 μm decreases by 60%. Metamaterial arrays can also be designed to short out the SRR in the VO_2 metal phase (figure 7.7B). No resonant peak is expected for this "closed-ring" resonator, therefore, the only effect is a reflectivity decrease of 56% at the SRR resonance wavelength.

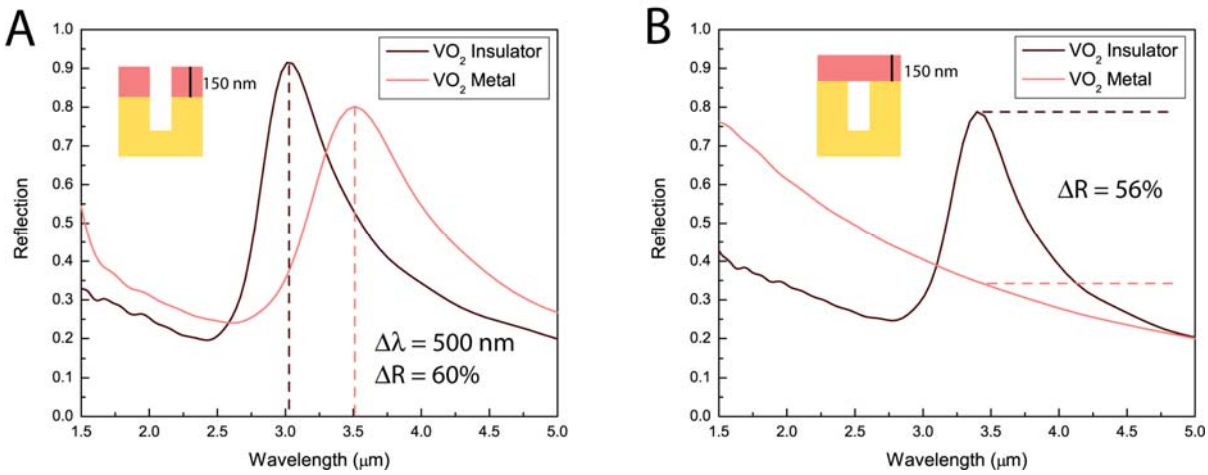

Figure 7.7. Simulations of VO_2-based hybrid-SRR metamaterial concepts. Design simulations for tunable metamaterials using switchable VO_2 elements. (A) Increasing the SRR arm lengths changes the resonant frequency drastically. (B) Electrically shorting the SRR elements causes the resonance to disappear when the VO_2 is in its metal phase. Each of these designs requires a two-mask electron beam lithography process.

7.5 Conclusions

In this chapter we presented the first active, frequency-tunable, metamaterial devices with resonances in the near-IR spectrum between 1.5 and 5 μm. These devices are based on hybrid-SRR structures fabricated on VO_2 thin films. The success of VO_2 as a switching element for the first iterations of these active metamaterials has spurred continued investigation. In addition to more advanced designs, optically and electrically induced metal phase transitions need to be studied.

Chapter 8
Optical Properties of Combinatorial Metal Films

In this chapter we demonstrate the ability to fabricate metal alloy thin films with tunable optical properties based on the alloy composition. A combinatorial approach is used to deposit various bimetallic systems based on silver, gold and copper via magnetron sputtering. Optical properties of Ag-Au, Ag-Cu and Au-Cu metal alloy films are investigated with variable angle spectroscopic ellipsometry. Simulations of metal structures are presented to illustrate the effect of tunable composition. The ability to selectively tune the optical properties of a metallic layer has significant implications for research in plasmonics, metamaterials and negative-index structures.

8.1 Introduction

Devices based on electromagnetic response in metals are currently attracting much attention. Metal optics at the nanoscale has led to enhanced transmission in subwavelength apertures (*Ebbesen et al. 1998*), plasmon waveguiding (*Brongersma et al. 2000*), cloaking (*Cai et al. 2007*), negative-index materials (*Lezec et al. 2007*) and metamaterials (*Chen et al. 2006*). This wide range of applications relies on coupling of electromagnetic energy to the collective oscillations of free electrons, or plasmons, at the interface between a dielectric and a metal. In order to minimize the loss of energy from plasmons due to absorption, the choice of conductive media is limited to a short list of nearly-free-electron metals such as silver, gold, and copper; which have relatively small optical frequency electronic damping. The study of metal-dielectric plasmonic devices has focused on designing the geometry or varying the dielectric material composition to achieve dispersion engineering. Metal alloy films offer a new optical engineering parameter to consider. Changing the optical properties of the metal layer can lead to graded optical index plasmonic structures, greater tunability in metal-insulator-metal waveguides, tunable resonances in optical metamaterials and greater access to the negative index regime of plasmon dispersion in metal-insulator systems. It is with this in mind that we set out to explore combinatorial synthesis of multimetal thin films.

8.2 Combinatorial Thin Films

Metal alloy material systems were fabricated by co-deposition using an AJA magnetron sputtering system capable of operating six targets using RF or DC plasma sputtering. Bi-metallic films were deposited at room temperature on 6" (111) Si wafers by exposure to two metal sputtering sources located below the substrate in pockets 180° opposite each other. Deposition rates were calibrated using a quartz crystal monitor to ensure equal flux of each metal at the sample midpoint. Each deposition was calibrated such that 150 nm of each metal was deposited at the midpoint of the silicon substrate. A DC plasma source is used to sputter each metal target at 1.5 Å/sec, and sputtered metal atoms are confined to a path to the substrate using a magnetic field, so-called magnetron sputtering. Deposition takes place with a background Ar gas pressure of 3 mTorr to maintain the plasma. Following deposition, the samples were optically characterized using electron dispersive spectroscopy (EDS), transmission electron microscopy (TEM), and variable angle spectroscopic ellipsometry (VASE).

Sample composition was investigated using EDS (figure 8.1). The deposited metal alloy samples were divided into multiple sections and the atomic percentage of each metal was determined. The electron beam energy was optimized at 9 keV to decrease the signal from the silicon substrate. We see from figure 8.1 that the Ag-Au film composition varies linearly across the entire six-inch sample. The inset shows the color gradient across the as-deposited Ag-Au sample. The sample was divided into 14 sections for optical characterization; the center sample was investigated by TEM.

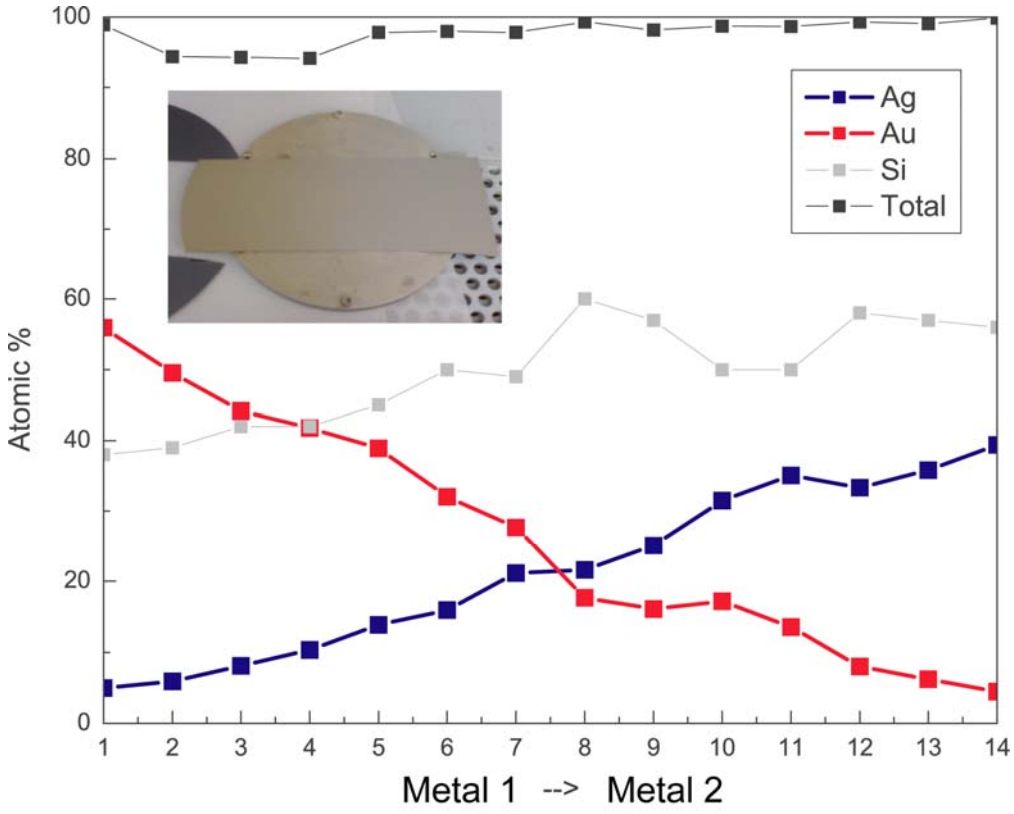

Figure 8.1. Electron dispersive spectroscopy: metal alloys. EDS characterization of the Ag-Au metal alloy system deposited on silicon. Silicon makes up a large fraction of the signal due to the sampling volume of the electron beam compared to the thickness of the film. (Inset) Optical photograph showing the color gradient along the silicon substrate as the alloy film varies from gold to silver.

Transmission electron microscopy was used to investigate the degree of alloying in the sputtered samples. Figure 8.2 shows (A) plan-view and (B) bright-field TEM images of a Ag-Au alloy sample of approximately 50:50 composition. Nanocrystals with dimensions <5 nm are seen in plan view within the matrix of the alloyed metal film.

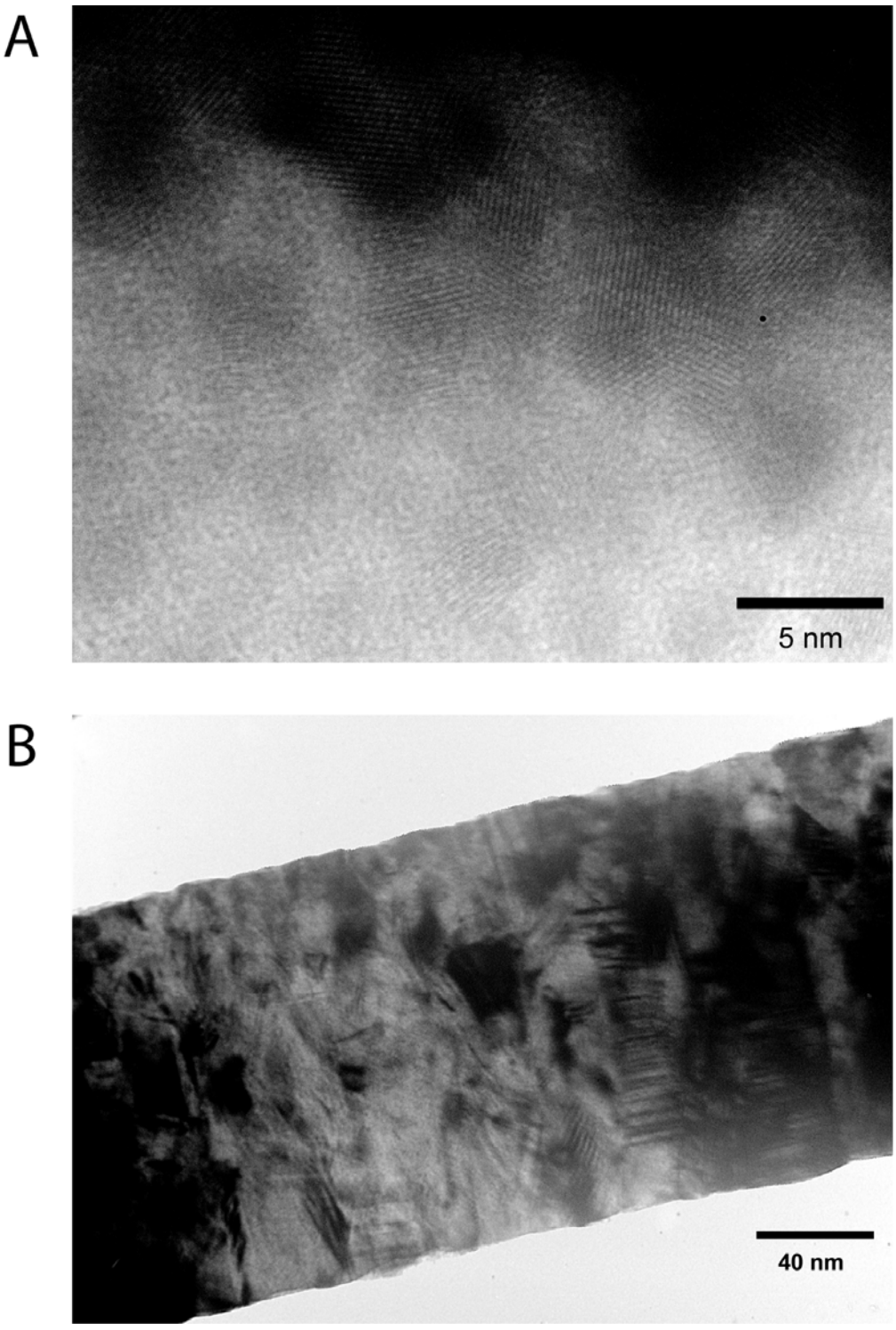

Figure 8.2. Transmission electron microscopy: Ag-Au. Transmission electron microscopy images of a 50:50 Ag-Au metal alloy sample. (A) The plan-view micrograph shows the presence of some nanocrystals of Ag and Au with dimensions <5 nm in a largely alloyed matrix. (B) Bright-field microscopy shows that the film is lacking voids.

8.3 Metal alloy Optical Characterization

VASE is a powerful technique for determining the optical properties of thin solid films as discussed previously in this thesis. Linearly polarized light is scattered at a particular angle from the surface of a sample with an arbitrary number of specific material interfaces and detected through a rotating polarizer. Reflections from each interface in a material stack are governed by the Fresnel equations. In the case of optically thick metal films, the transformation from measured Ψ and Δ values to n and k, or ε_1 and ε_2 is trivial as there is only one interface to consider. Figure 8.3 shows the measured Ψ and Δ values from (A) Ag-Au, (B) Ag-Cu, and (C) Au-Cu metal alloy material systems. We see that all three metal alloy systems show similar Ψ and Δ values in the near IR spectrum, far from the plasmon resonances. In the visible range, from 300 to 800 nm, the alloys show a uniform shift from one pure element to the other.

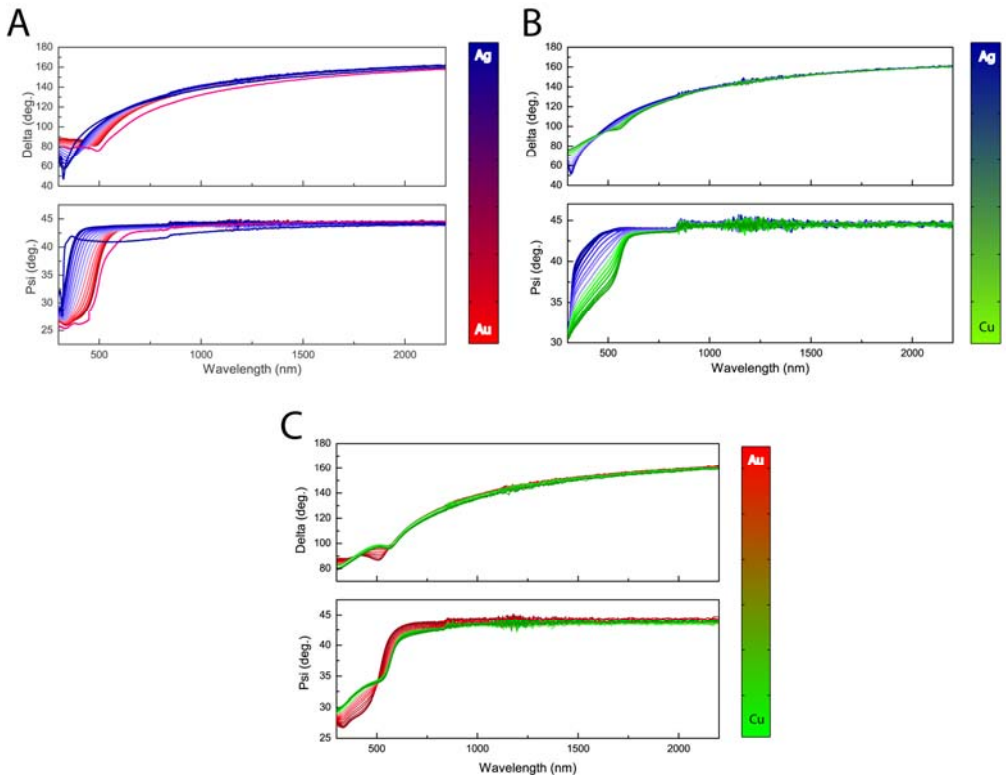

Figure 8.3. VASE: metal alloys. Variable angle spectroscopic ellipsometry Ψ and Δ for (A) Ag-Au, (B) Ag-Cu, and (C) Au-Cu alloy systems. Spectroscopic data were taken from 300 to 2200 nm along each sample.

The metal alloy dielectric functions were studied systematically at regular intervals across the sample. Figure 8.4A-C shows the complex dielectric constants derived from measured Ψ and Δ data at 70 degrees for 300 nm metal alloy films on silicon substrates. The data show a smooth transition of the optical constants for each sample from pure constituent metal 1 to metal 2. Figure 8.4B also plots ε_1 and ε_2 for pure Au to show that, for some wavelengths, the Ag-Cu system accesses ε_1 values not possible in the Ag-Au system. The ellipsometer spot size is approximately 1 mm wide by 3 mm long and the long axis was aligned perpendicular to the composition gradient. Pure samples of each constituent were deposited and characterized separately. We found VASE data for pure silver, gold, and copper samples are superior to data supplied in Palik *et al*.due to the higher resolution (1 data point per nm) and better sample quality. In addition, optical data taken with VASE is continuous across the wavelength ranges 300-850 nm.

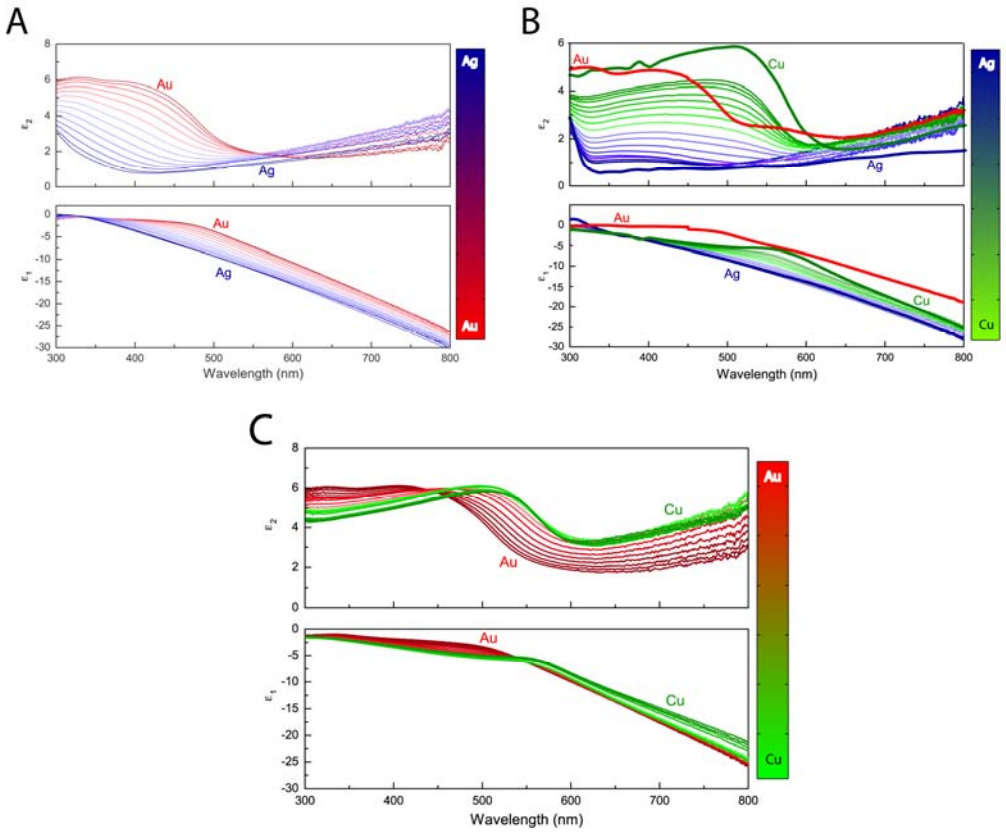

Figure 8.4. Metal alloy optical constants. ε_1 and ε_2 derived from variable angle spectroscopic ellipsometry Ψ and Δ data in the range 300–800 nm for (A) Ag-Au, (B) Ag-Cu, and (C) Au-Cu alloy systems. The optical constants for all three alloys vary smoothly from metal 1 to metal 2. Pure Ag, Au, and Cu samples were fabricated and characterized separately to ensure purity.

8.4 Metal Alloy Simulations

The optical constants found here were used to simulate the dispersion relation for a surface plasmon polariton at a metal alloy/air interface (figure 8.5). Here the SPP wavevector is calculated from $k_{SPP} = \frac{\omega}{c}\sqrt{\frac{\varepsilon_1\varepsilon_2}{\varepsilon_1+\varepsilon_2}}$. We see that using metal alloys with silver allows a wide range of wavevectors to be investigated in the region of anomalous dispersion.

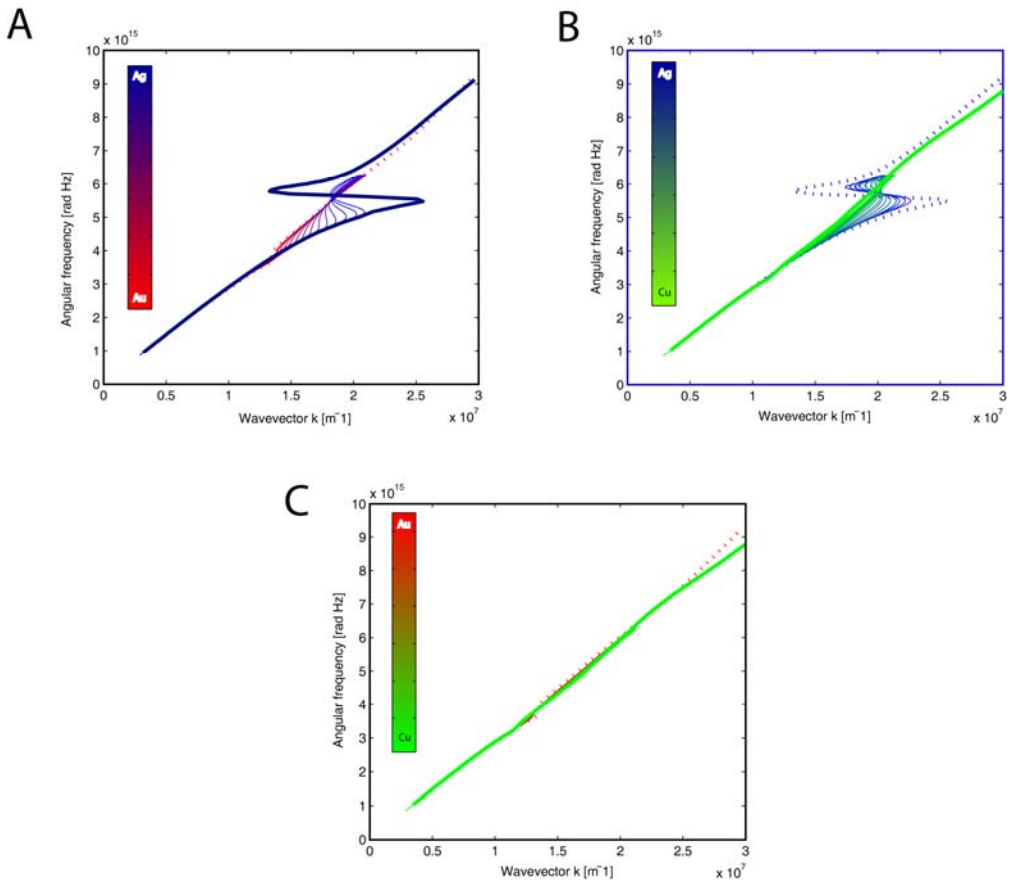

Figure 8.5. Simulated metal alloy SPP dispersion relations. Planar SPP dispersion diagrams for (A) Ag-Au, (B) Ag-Cu, and (C) Au-Cu metal alloy systems simulated using measured ε_1 and ε_2. Simulations are done for metal alloy films in air. The strong dispersion of Ag is dominant in both Ag-Au and Ag-Cu alloys. In Ag-Au alloys, Au shifts the dispersion relation down in both frequency and wavevector whereas the Cu in Ag-Cu only changes the wavevector. The Au-Cu system shows little nonlinear dispersion on this scale.

Simulations of metal nanoparticles with the compositions investigated here were also performed. The extinction cross section, C_{ext}, for 10 nm metal nanoparticles in vacuum was calculated at each composition using equation (8.1) (*Bohren & Huffman 1983*).

$$C_{ext} = \frac{\omega}{c}\sqrt{\frac{\sqrt{\mathrm{Re}(\varepsilon_1)^2 + \mathrm{Im}(\varepsilon_1)^2} + \mathrm{Re}(\varepsilon_1)}{2}}\,\mathrm{Im}\left(\frac{4\pi r^3(\varepsilon_2 - \varepsilon_1)}{(\varepsilon_2 + 2\varepsilon_2)}\right) \tag{8.1}$$

In figure 8.6 the extinction cross section for each metal alloy is investigated. For the case of Ag-Au, the resonant peak shifts in frequency and decreases in magnitude as the Au concentration increases. The Ag plasmon resonance peak intensity slowly decreases as the

Cu concentration increases. This is useful for tuning the nanoparticle resonance for applications as enhanced absorbers for solar cells, plasmon waveguides and nanoantennae. Ag-Cu nanoparticles show a broadening and decreasing of the extinction cross section.

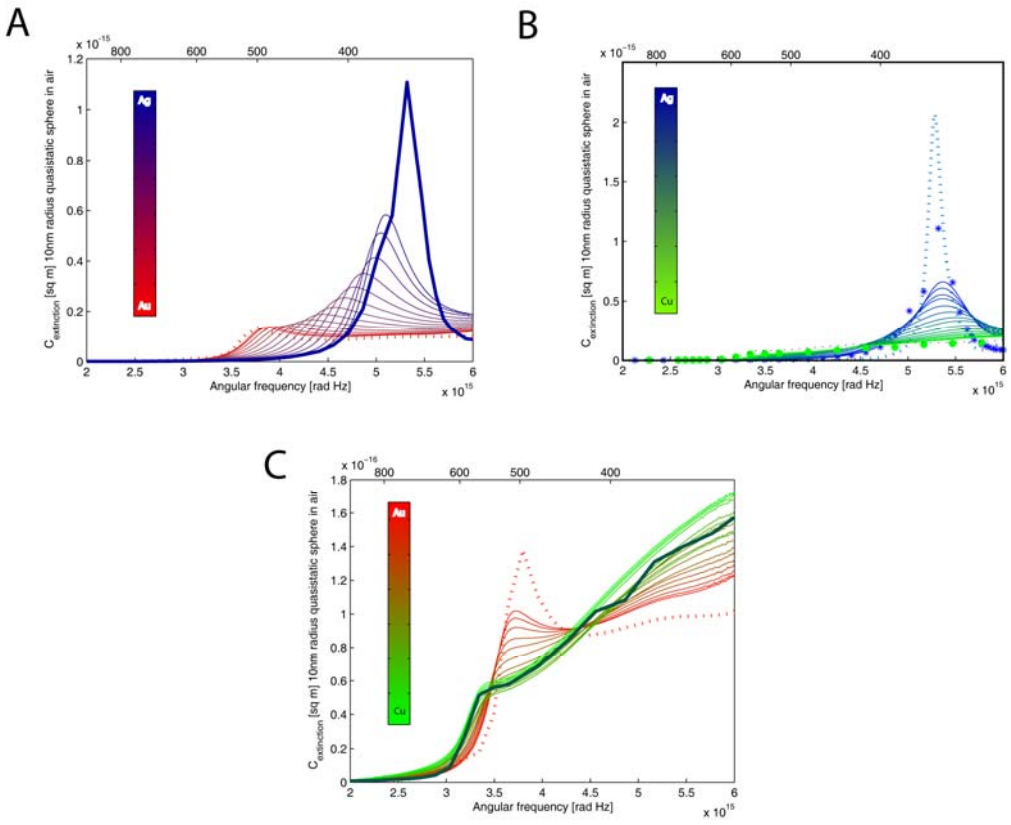

Figure 8.6. Extinction in metal alloy nanoparticles. Extinction cross sections for 10 nm metal alloy particles in vacuum (A) Ag-Au, (B) Ag-Cu, and (C) Au-Cu. Resonances in the Ag-Au nanoparticle vary smoothly from pure Ag to pure Au. Data from Palik *et al.* for pure Ag are used in (A). Measured data for pure Ag and Cu plotted in (B) show a much higher extinction cross section for the pure Ag than expected from Palik *et al*.

8.5 Conclusions

Metal alloy systems have been realized using combinatorial techniques based on magnetron sputtering. The optical properties of bi-metal films of Ag-Au, Ag-Cu, and Au-Cu have been investigated using VASE and the complex dielectric constants were found to vary systematically from pure metal 1 to pure metal 2. The largest variation of ε_1 and ε_2 for these metals is in the visible range from 300 to 850 nm. To investigate the effects of these variations, simulations of surface plasmon dispersion and nanoparticle extinction cross

section were performed. These simulations remain to be experimentally verified. In order to fabricate samples with a single alloy composition over a large area, a MBE chamber was built and deposition parameters explored for Ag, Au, and Cu evaporation.

References

Auciello, O., A. Gruverman, H. Tokumoto, S.A. Prakash, S. Aggarwal, and R. Ramesh. (1998) Nanoscale scanning force imaging of polarization phenomena in ferroelectric thin films, *Mater. Res. Bull. 23*.

Aydin, K. (2008) Characterization and applications of negative-index metamaterials, Ph.D. thesis, Bilkent University.

Barnes, W.L., A. Dereux, and T.W. Ebbesen. (2003) Surface plasmon subwavelength optics, *Nature 424*, 824-830.

Beckers, L., J. Schubert, W. Zander, J. Ziesmann, A. Eckau, P. Leinenbach, and C. Buchal. (1998) Structural and optical characterization of epitaxial waveguiding $BaTiO_3$ thin films on MgO, *J. App. Phys. 83*, 3305-3310.

Bhattacharya, K., and G. Ravichandran. (2003) Ferroelectric perovskites for electromechanical actuation, *Acta Mater. 51*, 5941-5960.

Bhattacharya, K., and R.D. James. (2005) The material is the machine, *Science 307*, 53-54.

Bhushan, B., and X.D. Li. (2003) Nanomechanical characterization of solid surfaces and thin films, *Int. Mater. Rev. 48*, 125-164.

Bohren, C.F., and D.R. Huffman (1983) *Absorption and scattering of light by small particles*, Wiley, New York.

Bradley, R.M., J.M.E. Harper, and D.A. Smith. (1986) Theory of thin-film orientation by ion bombardment during deposition, *J. Appl. Phys. 60*, 4160-4164.

Brewer, R.T., and H.A. Atwater. (2002) Rapid biaxial texture development during nucleation of MgO thin films during ion beam-assisted deposition, *Appl. Phys. Lett. 80*, 3388-3390.

Brongersma, M.L., and P.G. Kik (2000) *Surface plasmon nanophotonics*, Springer, Dordrecht.

Burcsu, E., G. Ravichandran, and K. Bhattacharya. (2000) Large strain electrostrictive actuation in barium titanate, *Appl. Phys. Lett. 77*, 1698-1700.

Cai, W., U.K. Chettiar, A.V. Kildishev, and V.M. Shalaev. (2007) Optical Cloaking with Metamaterials, *Nat. Phot. 1*, 224-227.

Chae, B.G., H.T. Kim, D.H. Youn, and K.Y. Kang. (2005) Abrupt metal-insulator transition observed in VO_2 thin films induced by a switching voltage pulse, *Physica B 369*, 76-80.

Chen, H.-T., W.J. Padilla, J.M. Zide, A.C. Gossard, A.J. Taylor, and R.D. Averitt. (2006) Active terahertz metamaterial devices, *Nature 444*, 597-600.

Chen, H.-T., J.F. O'Hara, A.K. Azad, A.J. Taylor, R.D. Averitt, D.B. Shrekenhamer, and W.J. Padilla. (2008) Experimental demonstration of frequency-agile terahertz metameterials, *Nat. Photonics 2*, 295-298.

Choi, K.J., M. Biegalski, Y.L. Li, A. Sharan, J. Schubert, R. Uecker, P. Reiche, Y.B. Chen, X.Q. Pan, V. Gopalan, L.-Q. Chen, D.G. Schlom, and C.B. Eom. (2004) Enhancement of ferroelectricity in strained $BaTiO_3$ thin films, *Science 306*, 1005-1009.

Chyou, J.J., C.S. Chu, Z.H. Shih, and C.Y. Lin. (2005) Fabrication and metrology of an electro-optic polymer light modulator based on waveguide-coupled surface plasmon resonance, *Opt. Eng. 44*, 034001.

Damjanovic, D. (1998) Ferroelectric, dielectric and piezoelectric properties of ferroelectric thin films and ceramics, *Reports on Progress in Physics 61*, 1267-1324.

Degiron, A., J.J. Mock, and D.R. Smith. (2007) Modulating and tuning the response of metamaterials at the unit cell level, *Optics Express 15*, 1115-1127.

Dicken, M.J., K. Diest, Y.B. Park, and H.A. Atwater. (2007) Growth and optical property characterization of textured barium titanate thin films for photonic applications, *J. Cryst. Growth 300*, 330-335.

Dionne, J.A., L.A. Sweatlock, H.A. Atwater, and A. Polman. (2005) Planar metal plasmon waveguides: frequency-dependent dispersion, propagation, localization, and loss beyond the free electron model, *Phys. Rev. B 72*, 075405.

Dionne, J.A., H.J. Lezec, and H.A. Atwater. (2006) Highly confined photon transport in subwavelength metallic slot waveguides, *Nano Lett. 6*, 1928-1932.

Donev, E.U., J.Y. Suh, F. Villegas, R. Lopez, R.F. Haglund Jr., and L.C. Feldman. (2006) Optical properties of subwavelength hole arrays in vanadium dioxide thin films, *Phys. Rev. B 73*, 201401.

Dong, L., and D.J. Srolovitz. (1998) Texture development mechanisms in ion beam assisted deposition, *J. Appl. Phys. 84*, 5261-5269.

Driscoll, T., S. Palit, M.M. Qazilbash, M. Brehm, F. Keilmann, B.G. Chae, S.J. Yun, H.T. Kim, S.Y. Cho, N.M. Jokerst, D.R. Smith, and D.N. Basov. (2008) Dynamic tunig of an

infrared hybrid-metamaterial resonance using vanadium dioxide, *App. Phys. Lett. 93*, 024101.

Duiker, H.M., P.D. Beale, J.F. Scott, C.A.P. Dearaujo, B.M. Melnick, J.D. Cuchiaro, and L.D. McMillan. (1990) Fatigue and switching in ferroelectric memories - theory and experiment, *J. Appl. Phys. 68*, 5783-5791.

Ebbesen, T.W., H.J. Lezec, H.F. Ghaemi, T. Thio, and H.J. Wolff. (1998) Extraordinary optical transmission through sub-wavelength hole arrays, *Nature 391*, 667-669.

El-Naggar, M., D.A. Boyd, and D.G. Goodwin. (2005) Characterization of highly-oriented ferroelectric $Pb_xBa_{1-x}TiO_3$, *J. Mater. Res. 20*, 2969-2976.

El-Naggar, M. (2006) Textured ferroelectric thin films: synthesis, characterization, and influence of compositional grading on the dielectric behavior, Ph. D. thesis, California Institute of Technology.

Enkrich, C., M. Wegener, S. Linden, S. Burger, L. Zschiedrich, F. Schmidt, J.F. Zhou, T. Koschny, and C.M. Soukoulis. (2005) Magnetic Metamaterials at Telecommunication and Visible Frequencies, *Phys. Rev. Lett. 95*, 203901.

Fang, F., and W. Yang. (2002) Indentation-induced cracking and 90° domain switching pattern in barium titanate ferroelectric single crystals under different poling, *Mater. Lett. 57*, 198-202.

Fatuzzo, E., and W. Merz (1967) *Ferroelectricity*, North-Holland, Amsterdam.

Garcia-Vidal, F.J., H.J. Lezec, T.W. Ebbesen, and L. Martin-Moreno. (2003) Multiple paths to enhance optical transmission through a single subwavelength slit, *Phys. Rev. Lett. 90*, 213901.

Gay, G., O. Alloschery, B.V.E. Lesegno, C. O'Dwyer, J. Weiner, and H.J. Lezec. (2006) The optical response of nanostructured surfaces and the composite diffracted evanescent wave model, *Nat. Phys. 2*, 262-267.

Harnagea, C. (2001) Local piezoelectric response and domain structures in ferroelectric thin films investigated by voltage-modulated force microscopy, Ph.D. thesis, Martin-Luther-Universitt Hally Wittenberg.

Harnagea, C., A. Pignolet, M. Alexe, and D. Hesse. (2002) Piezoresponse scanning force microscopy: what quantitative information can we really get out of piezoresponse measurements on ferroelectric thin films, *Integrated Ferroelectrics 44*, 113-124.

Holt, M., K. Hassani, and M. Sutton. (2005) Microstructure of ferroelectric domains in $BaTiO_3$ observed via x-ray microdiffraction, *Phys. Rev. Lett. 95*, 085504.

ITRS. (2007) International technology roadmap for semiconductors.

Jin, P., and S. Tanemura. (1995) Relationship between transition temperature and x in $V_{1-x}W_xO_2$ films deposited by dual-target magnetron sputtering, *Jpn. J. Appl. Phys. 34*, 2459-2460.

Kalinin, S.V., and D.A. Bonnell. (2002a) Imaging mechanism of piezoresponse force microscopy of ferroelectric surfaces, *Phys. Rev. B 65*, 125408.

Kalinin, S.V., C.Y. Johnson, and D.A. Bonnell. (2002b) Domain polarity and temperature induced potential inversion on the $BaTiO_3$(100) surface, *J. Appl. Phys. 91*, 3816-3823.

Kalinin, S.V., A. Gruverman, and D.A. Bonnell. (2004) Quantitative analysis of nanoscale switching in $SrBi_2Ta_2O_9$ thin films by piezoresponse force microscopy, *Appl. Phys. Lett. 85*, 795-797.

Kim, I.D., Y. Avrahami, H.L. Tuller, Y.B. Park, M.J. Dicken, and H.A. Atwater. (2005) Study of orientation effect on nanoscale polarization in $BaTiO_3$ thin films using piezoresponse force microscopy, *Appl. Phys. Lett. 86*, 192907.

Kretschmann, E., and H. Raether. (1968) Radiative decay of non-radiative surface plasmons excited by light, *Zeitschrift fur Naturforschung 23A*.

Krulevitch, P., A.P. Lee, P.B. Ramsey, J.C. Trevino, J. Hamilton, and M.A. Northrup. (1996) Thin film shape memory alloy microactuators, *J. MEMS 5*, 270-282.

Kwak, B.S., K. Zhang, E.P. Boyd, A. Erbil, and B.J. Wilkens. (1991) Metalorganic chemical vapor deposition of $BaTiO_3$ thin films, *J. Appl. Phys. 69*, 767-772.

Lalanne, P., J.P. Hugonin, and J.C. Roier. (2005) Theory of surface plasmon generation at nanoslit apertures, *Phys. Rev. Lett. 95*, 263902.

Lappalainen, J., S. Heinilehto, S. Saukko, V. Lantto, and H. Jantunen. (2008) Microstructure dependent switching properties of VO_2 thin films, *Sensor. Actuat. A 142*, 250-255.

Lemoine, C., B. Gilbert, B. Michaux, J.P. Pirard, and A.J. Lecloux. (1994) Synthesis of barium titanate by the sol-gel process, *J. Non-Cryst. Solids 175*, 1-13.

Lezec, H.J., A. Degiron, E. Devaux, R.A. Linke, L. Martin-Moreno, F.J. Garcia-Vidal, and T.W. Ebbesen. (2002) Beaming light from a subwavelength aperture, *Science 297*, 820-822.

Lezec, H.J., and T. Thio. (2004) Diffracted evaescent wave model for enhanced and suppressed optical transmission through sub-wavelength hole arrays, *Opt. Exp. 12*, 3629-3651.

Lezec, H.J., J.A. Dionne, and H.A. Atwater. (2007) Negative Refraction at Visible Frequencies, *Science 316*, 3.

Li, J.Y., R.C. Rogan, E. Ustundag, and K. Bhattacharya. (2005) Domain switching in polycrystalline ferroelectric ceramics, *Nat. Mater. 4*, 776-781.

Li, X.D., and B. Bhushan. (2002) A review of nanoindentation continuous stiffness measurement technique and its applications, *Mater. Charact. 48*, 11-36.

Li, X.D., H.S. Gao, C.J. Murphy, and K.K. Caswell. (2003) Nanoindentation of silver nanowires, *Nano Lett. 3*, 1495-1498.

Li, Z., C.M. Foster, X.H. Dai, S.K. Chan, and D.J. Lam. (1992) Piezoelectrically-induced switching of 90° domains in tetragonal $BaTiO_3$ and $PbTiO_3$ investigated by micro-Raman spectroscopy, *J. Appl. Phys. 71*, 4481-4486.

Linden, S., C. Enkrich, M. Wegener, J. Zhou, T. Koschny, and C.M. Soukoulis. (2004) Magnetic response of metamaterials at 100 terahertz *Science 306*, 1351-1353.

Lipinsky, T., J. Schubert, and C. Buchal. (2005) Crack-free $BaTiO_3$ films on Si with SiO_2, MgO, or Al_2O_3 buffer layers, *J. Opt. Soc. Am. B 22*, 913-916.

Lisoni, J.G., M. Siegert, C.H. Lei, W. Biegel, J. Schubert, W. Zander, and C. Buchal. (2001) The growth of MgO buffer layers on sapphire for the epitaxy of $BaTiO_3$ optical thin films, *Thin Solid Films 389*, 219-226.

Lysenko, S., A.J. Rua, V. Vikhnin, J. Jimenez, F. Fernandez, and H. Liu. (2006) Light-induced ultrafast phase transitions in VO_2 thin film, *App. Surf. Sci. 252*, 5512-5515.

Maier, S.A., P.G. Kik, H.A. Atwater, S. Meltzer, E. Harel, B.E. Koel, and A.A.G. Requicha. (2003) Local detection of electromagnetic energy transport below the diffraction limit in metal nanoparticle plasmon waveguides, *Nat. Mater. 2*, 229-232.

McKee, R.A., F.J. Walker, J.R. Conner, E.D. Specht, and D.E. Zelmon. (1991) Molecular beam epitaxy growth of epitaxial barium silicide, barium oxide, and barium titanate on silicon, *Appl. Phys. Lett. 59*, 782-784.

Narayan, J., and V.M. Bhosle. (2006) Phase transition and critical issues in structure-property correlations of vanadium oxide, *J. Appl. Phys. 100*, 103524.

Nye, J. (1957) *Physical properties of crystals*, Oxford University Press, Oxford.

Oliver, W.C., and G.M. Pharr. (1992) An improved technique for determining hardness and elastic modulus using load and displacement sensing indentation experiments, *J. Mater. Res. 7*, 1564-1583.

OptiFDTD. (2005) Finite-Difference Time-Domain Simulation Design Software Optiwave Systems Inc.

Pacifici, D., H.J. Lezec, and H.A. Atwater. (2007) All-optical modulation by plasmonic excitation of CdSe quantum dots, *Nat. Photonics 1*, 402-406.

Pacifici, D., H.J. Lezec, J. Weiner, and H.A. Atwater. (2008) Quantitative determination of optical transmission through sub-wavelength slit arrays in Ag films, *Phys. Rev. B 77*, 115411.

Padilla, W.J., D.N. Basov, and D.R. Smith. (2006) Negative refractive index metamaterials, *Materials Today 9*, 28-35.

Park, S.E., S. Wada, L.E. Cross, and T.R. Shrout. (1999) Crystallographically engineered $BaTiO_3$ single crystals for high-performance piezoelectrics, *J. Appl. Phys. 86*, 2746-2750.

Park, Y.B., J.L. Ruglovsky, and H.A. Atwater. (2004) Microstructure and properties of single crystal $BaTiO_3$ thin films synthesized by ion implantation-induced layer transfer, *Appl. Phys. Lett. 85*, 455-457.

Pendry, J.B., A.J. Holden, D.J. Robbins, and W.J. Stewart. (1999) Magnetism from conductors and enhanced nonlinear phenomena, *IEEE Trans. Microw. Theory 47*, 2075-2084.

Pendry, J.B. (2000) Negative Refraction Makes a Perfect Lens, *Phys. Rev. Lett. 85*, 3966-3969.

Petraru, A., J. Schubert, M. Schmid, and C. Buchal. (2002) Ferroelectric $BaTiO_3$ thin-film optical waveguide modulators, *Appl. Phys. Lett. 81*, 1375-1377.

Petraru, A., J. Schubert, M. Schmid, O. Trithaveesak, and C. Buchal. (2003) Integrated optical Mach-Zehnder modulator based on polycrystalline $BaTiO_3$, *Opt. Lett. 15*, 2527-2529.

Raether, H. (1988) *Surface plasmons on smooth and rough surfaces and on gratings*, Springer, Berlin.

Rakic, A.D., A.B. Djurisic, J.M. Elazar, and M.L. Majewski. (1998) Optical properties of metallic films for vertical-cavity optoelectronic devices, *Appl. Opt. 37*, 5271-5283.

Ramesh, R., W.K. Chan, B. Wilkens, B. Gilchrist, T. Sands, J.M. Tarascon, V.G. Keramidas, D.K. Fork, J. Lee, and A. Safari. (1992) Fatigue and retention in ferroelectric Y-Ba-Cu-O/Pb-Zr-Ti-O/Y-Ba-Cu-O heterostructures, *Appl. Phys. Lett. 61*, 1537-1539.

Ressler, K.G., N. Sonnenberg, and M.J. Cima. (1997) Mechanism of biaxial alignment of oxide thin films during ion-beam assisted deposition, *J. Am. Ceram. Soc. 80*, 2637-2648.

Rogan, R.C., N. Tamura, G.A. Swift, and E. Ustundag. (2003) Direct measurement of triaxial strain fields around ferroelectric domains using x-ray microdiffraction, *Nat. Mater. 2*, 379-381.

Ruglovsky, J.L. (2007) Correlating microscopic ferroelectric properties and macroscopic thin film device performance, Ph.D. thesis, California Institute of Technology.

Saleh, B.E.A., and M.C. Teich (1991) *Fundamentals of photonics*, Wiley, New York.

Schlom, D.G., J.H. Haeni, J. Lettieri, C.D. Theis, W. Tian, J.C. Jiang, and X.Q. Pan. (2001) Oxide nano-engineering using MBE, *Mat. Sci. Eng. B 87*, 282-291.

Schouten, H.F., N. Kuzmin, G. Dubois, T.D. Visser, G. Gbur, P.F.A. Alkemade, H. Blok, G.W. 'tHooft, D. Lenstra, and E.R. Eliel. (2005) Plasmon-assisted two-slit transmission: Young's experiment revisited, *Phys. Rev. Lett. 94*, 053901.

Scott, J.F., C.A. Araujo, B.M. Melnick, L.D. McMillan, and R. Zuleeg. (1991) Quantitative measurement of space-charge effects in lead zirconate-titanate memories, *J. Appl. Phys. 70*, 382-388.

Scott, J.F. (2000) *Ferroelectric memories*, Springer, Berlin.

Shalaev, V.M., W. Cai, U.K. Chettiar, H.-K. Yuan, A.K. Sarychev, V.P. Drachev, and A.V. Kildishev. (2005) Negative index of refraction in optical metamaterials, *Opt. Lett. 30*, 3356-3358.

Shalaev, V.M. (2007) Optical negative-index metamaterials, *Nat. Phot. 1*, 41-47.

Smith, D.A., J.B. Pendry, and M.C.K. Wiltshire. (2004) Metamaterials and Negative Refractive Index, *Science 305*, 788-792.

Smith, D.R., W.J. Padilla, D.C. Vier, S.C. Nemat-Nasser, and S. Schultz. (2000) Composite medium with simultaneously negative permeability and permittivity, *Phys. Rev. Lett. 84*, 4184-4187.

Soukoulis, C.M., S. Linden, and M. Wegener. (2007) Negative Refractive Index at Optical Wavelengths, *Science 315*, 47-49.

Stavistki, N., V. Lyahovitskaya, J. Nair, I. Zon, R. Popovitz-Biro, E. Wachtel, Y. Feldman, and I. Lubomirsky. (2002) Substrate-free crystallization of distorted hexagonal barium titanate thin films, *Appl. Phys. Lett. 81*, 4177-4179.

Suh, J.Y., R. Lopez, L.C. Feldman, and R.F. Haglund Jr. (2004) Semiconductor to metal phase transition in the nucleation and growth of VO_2 nanoparticles and thin films, *J. Appl. Phys. 96*, 1209-1213.

Sweatlock, L.A., S.A. Maier, H.A. Atwater, J.J. Penninkhof, and A. Polman. (2005) Highly confined electromagnetic fields in arrays of strongly coupled Ag nanoparticles, *Phys. Rev. B 71*, 235408.

Tang, P., D.J. Towner, A.L. Meier, and B.W. Wessels. (2003) Polarisation-insensitive Si_3N_4 strip-loaded $BaTiO_3$ thin-film waveguide with low propagation losses, *Electron. Lett. 39*, 1651-1652.

Tang, P., D.J. Towner, T. Hamano, A.L. Meier, and B.W. Wessels. (2004a) Electrooptic modulation up to 40 GHz in a barium titanate thin film waveguide modulator, *Opt. Exp. 12*, 5962-5967.

Tang, P., D.J. Towner, A.L. Meier, and B.W. Wessels. (2004b) Low-voltage, polarization-insensitive, electro-optic modulator based on a polydomain barium titanate thin film, *Appl. Phys. Lett. 85*, 4615-4617.

Theis, C.D., and D.G. Schlom. (1996) Cheap and stable titanium source for use in oxide molecular beam epitaxy systems, *J. Vac. Sci. Technol. A 14*, 2677-2679.

Thio, T., K.M. Pellerin, R.A. Linke, H.J. Lezec, and T.W. Ebbesen. (2001) Enhanced light transmission through a single subwavelength aperture, *Opt. Lett. 26*, 1972-1974.

Veselago, V.G. (1968) The electrodynamics of substances with simultaneously negative values of permittivity and permeability, *Sov. Phys. Usp. 10*, 504-509.

Wang, C.P., K.B. Do, M.R. Beasley, T.H. Geballe, and R.H. Hammond. (1997) Deposition of in-plane textured MgO on amorphous Si_3N_4 substrates by ion-beam-assisted deposition and comparisons with ion-beam-assisted deposited yttria-stabilized-zirconia, *Appl. Phys. Lett. 71*, 2955-2957.

Wei, Q.H., K.H. Su, S. Durant, and X. Zhang. (2004) Plasmon resonance of finite one-dimensional Au nanoparticle chains, *Nano Lett. 4*, 1067-1071.

Wills, L.A., B.W. Wessels, D.S. Richeson, and T.J. Marks. (1992) Epitaxial growth of $BaTiO_3$ thin films by organometallic chemical vapor deposition, *Appl. Phys. Lett. 60*, 41-43.

Xu, Z.H., and D. Rowcliffe. (2004) Finite element analysis of substrate effects on indentation behaviour of thin films, *Thin Solid Films 447*, 399-405.

Xu, Z.H., and X.D. Li. (2006) Sample size effect on nanoindentation of micro-/nanostructures, *Acta Mater. 54*, 1699-1703.

Yu, L.S., J.M.E. Harper, Cuomo, J. J., and D.A. Smith. (1985) Alignment of thin films by glancing angle ion bombardment during deposition, *Appl. Phys. Lett. 47*, 932-933.

Zeng, H.R., H.F. Yu, R.Q. Chu, G.R. Li, H.S. Luo, and Q.R. Yin. (2004) Domain orientation imaging of PMN–PT single crystals by vertical and lateral piezoresponse force microscopy, *J. Cryst. Growth 267*, 194-198.

Zgonik, M., P. Bernasconi, M. Duelli, R. Schlesser, and P. Gunter. (1994) Dielectric, elastic, piezoelectric, electro-optic, and elasto-optic tensors of $BaTiO_3$ crystals, *Phys. Rev. B 50*, 5941-5949.